PHOTOLUMINESCENCE IN SMART NANOCOMPOSITES AND FERROELECTRIC ULTRATHIN FILMS

ZHAO YIFEI

PhD

The Hong Kong Polytechnic University

2026

The Hong Kong Polytechnic University
Department of Applied Physics

Photoluminescence in Smart Nanocomposites and Ferroelectric Ultrathin Films

ZHAO Yifei

A thesis submitted in partial fulfillment of the requirements for the degree of Doctor of Philosophy

August 2025

CERTIFICATE OF ORIGINALITY

I hereby declare that this thesis is my own work and that, to the best of my knowledge and belief, it reproduces no material previously published or written, nor material that has been accepted for the award of any other degree or diploma, except where due acknowledgement has been made in the text.

_____(Signed)

ZHAO Yifei (Name of student)

Abstract

The exponential growth in information across diverse media drives an urgent need for multifunctional materials and devices beyond conventional electrical paradigms. Optical signal processing offers a promising route with contactless operations, parallel processing capabilities, high information bandwidth, and potential visualization of output signals. While "*smart phosphors*" with stimuli-responsive photoluminescence (PL) properties have seen widespread utilizations in optical information encryption and data storage, the dynamic aspect of PL variations and its implementation in optical information processing have not been fully harnessed. To bridge this gap, this thesis explores the construction of smart nanocomposites with PL-based neuromorphic behaviors using mixed-halide perovskite (MHPe) and macroporous Y_2O_3:Eu (MYE) smart nanocomposite. An all-optical physical reservoir computing is further developed based on MHPe@MYE smart phosphor, evidencing the potential of PL functions in classification of complex image datasets. After confirming the capability of PL functions in optical information processing, the down-scaling integration of PL into existing main-stream thin-film platforms is then explored. Ferroelectric (FE) HfO_2 has garnered significant research attention due to the exceptional nanoscale ferroelectricity and complementary-metal-oxide-semiconductor (CMOS) compatibility. Therefore, the thesis demonstrates the scaling-down incorporation of PL functions into ultrathin HfO_2 films through Er^{3+} doping with simultaneously improved FE endurance, potentially pathing the way towards multimodal neuromorphic devices at ultrathin levels.

In the first part of the thesis, MHPe@MYE smart nanocomposites with porous structure are constructed by hard-templated sol-gel syntheses. It demonstrates

progressively evolving PL properties variations upon light stimuli in the ultraviolet (UV) and blue region. The memristor-like PL variations with all-optical "Write" and "Read" processes are originated from the light-induced and dark-recoverable halogen migrations within MHPe@MYE. Density function theory (DFT) theoretical simulation reveals that a compositional adaptive halogen migration at the interface between MHPe and MYE plays a crucial role in these neuromorphic PL variations. Spectral investigations demonstrate rich neuromorphic properties that closely mimic biological synaptic behaviors, including paired-pulse facilitation (PPF), stimuli-dependent synaptic behaviors, and long-term memory (LTM).

In the second section, the PL-based neuromorphic computing capabilities of MHPe@MYE are further evaluated by leveraging the non-linear and volatile PL variation features. Utilizing optical stimuli and PL-readouts as a physical reservoir, the system achieves discrimination of 4-bit binary sequences. Furthermore, it exhibits considerable potential for image recognition tasks, attaining an accuracy of 94.4% in classifying the Modified National Institute of Standards and Technology (MNIST) handwritten digits and UV fingerprints from Sokoto Coventry Fingerprint (SOCOFing) dataset. Such a PL-based physical reservoir concept is found broadly applicable to conventional "*smart phosphor*" systems such as persistent luminescence (PersL) phosphors, demonstrating the vast potential of PL functions in the emerging information science applications.

The third part of the thesis focuses on the introduction of PL functions into FE HfO_2 to establish an ultrathin-film-level dual-mode platform. It is found the Er^{3+} dopant can not only introduce both UC and DC PL into HfO_2, but also simultaneously stabilize the metastable ferroelectricity in HfO_2. DFT theoretical investigation evidences the

two-way doping effect of Er^{3+} to induce in-gap localized Er 4*f*-*f* transitions while anchoring charged oxygen vacancies (V_O) to prevent domain wall pinning and electrical breakdown during cyclic FE switching. The experimental growth of 7 a.t.% Er^{3+}-doped HfO_2 (HErO) by pulsed-laser deposition (PLD) results in high-quality epitaxial thin film. Robust ferroelectricity can be obtained across a wide thickness range of 3 - 30 nm with modest remnant polarization of ~21 μC/cm^2. Notable endurance is observed to survive more than 10^{11} switching cycles at 1M Hz without breakdown or obvious degradation. Concomitant with Er-stabilized ferroelectricity, the distinct Er^{3+} energy levels in HErO enable PL spanning both near-infrared (NIR, ~1550 nm, via DC) and visible regimes (520-650 nm, via UC) under 980 nm excitation. Such intrinsic PL integration of FE HfO_2 may render extended information freedom and process versatility for future dual-mode neuromorphic computing.

List of Publications

Peer-reviewed Journals

1. **Y. Zhao**, M. Li, M-C. Wong, X. Han, F. Guo, Y. Liu, X. Lao, Z. Dang, S-Y. Pang, Z. Wu, S. Ye*, J. Hao*, Smart phosphor with neuromorphic behaviors enabling full-photoluminescent Write and Read for all-optical physical reservoir computing. ***Nat. Commun.*** *2025, 16, 7516.*

2. Q. Bai, X. Lao, S-Y. Pang, **Y. Zhao**, Y. Liu, X-Y. Tian, J. Hao*, Plaque-Targeted Delivery of Fluoride-Free MXene Nanozyme for Alleviating Atherosclerosis via Sonocatalytic Therapy. ***Adv. Mater.*** *2025, 2420189*.

3. Z. Dang, F. Guo, **Y. Zhao**, K. Jin, W. Jie, J. Hao*, Ferroelectric Modulation of ReS_2-Based Multifunctional Optoelectronic Neuromorphic Devices for Wavelength-Selective Artificial Visual System. ***Adv. Funct. Mater.*** *2024, 34, 2400105*.

4. X. Lao, Q. Bai, **Y. Zhao**, X. Dai, Y. Liu, X. Han, J. Hao*, Enhanced Sonodynamic Bacterial Elimination and Wound Healing Therapy Based on Lanthanide Ion Doped Bi_2WO_6 Nanosheets and Hydrogel Platform. ***Adv. Funct. Mater.*** *2025, 2511512*.

5. F. Guo, W-F. Io, Z. Dang, Y. Zhao, S-Y. Pang, **Y. Zhao**, X. Lao, J. Hao*, Bio-Inspired Optoelectronic Neuromorphic Device Based on 2D vdW Ferroelectric Heterostructure for Nonlinearly Preprocessing Visual Information and Convolutional Operation. ***Adv. Electron. Mater.*** *2025, 11, 2400528*.

6. Y. Liu, X. Lao, M-C. Wong, M. Song, **Y. Zhao**, Y. Ma, Q. Bai, J. Hao*, Intelligent Point-of-Care Biosensing Platform Based on Luminescent Nanoparticles and Microfluidic Biochip with Machine Vision Algorithm Analysis. ***Nano-Micro Lett.*** *2025, 17, 215*.

7. W-F. Io, S-Y. Pang, L-W. Wong, Y. Zhao, R. Ding, J. Mao, **Y. Zhao**, F. Guo, S.

Yuan, J. Zhao, J. Yi, J. Hao*, Direct observation of intrinsic room-temperature ferroelectricity in 2D layered $CuCrP_2S_6$. ***Nat. Commun.*** *2023, 14, 7304*.

8. Y. Zhao, J. Mao, Z. Wu, W-F. Io, S-Y. Pang, **Y. Zhao**, J. Hao*, A clean transfer approach to prepare centimetre-scale black phosphorus crystalline multilayers on silicon substrates for field-effect transistors. ***Nat. Commun.*** *2024, 15, 6795*.

9. Z. Wu, **Y. Zhao**, F. Yang, J. Hao*, Device physics and architecture advances in tunnel field-effect transistors, ***Interdiscip. Mater.*** *2025, 4 (5), 686*.

10. Q. Cui, Q. Cui, W. F. Io, J. Mao, Z. Liu, W. Zhu, F. Guo, **Y. Zhao**, Z. Dang, Z. Wu, A. Delin, L. Song, J. Hao*. Flexoelectric tunnel junctions based on centrosymmetric dielectric monolayer, ***Mater. Today*** *2025, 91, 34*.

11. Y. Ma, M.-C. Wong, M. Song, P. Wang, Y. Liu, **Y. Zhao**, H. Chen, J. Liu, J. Hao*. Machine Learning-Assisted 3D SERS Chip with Acoustic Enrichment for High-Accuracy Diagnosis of Respiratory Viruses and Emerging Pathogens. ***ACS Sensors*** *2025, 10 (10), 7886*.

Presentations at International Conferences

1. **Y. Zhao**, M. Li, S. Ye*, and J. Hao*, Smart Phosphors for Full-Photoluminescent Physical Reservoirs (Jul. 17, 2025), at National Conference on Luminescent Materials and Devices, Guiyang, China 2025. (Oral Presentation)
2. **Y. Zhao**, M. Li, S. Ye*, and J. Hao*, Smart phosphor with neuromorphic behaviors enabling full photo-luminescent Write & Read for all-optical physical reservoir computing (Oct. 25, 2025), at The 12th National Symposium on Rare Earth Luminescent Materials, Changsha, China 2025. (Poster Presentation)

Awards

1. Presentation Award 2024 (Merit)

   @ Postgraduate Research Seminar 2024, AP, PolyU

2. Best Presentation Award

   @ 2025 National Conference on Luminescent Materials and Applications, Guiyang, China (2025 全国发光材料性质及应用研究新进展学术会议)

3. Outstanding Poster Award

   @ The 12th National Symposium on Rare Earth Luminescent Materials, Changsha, China (第十二届全国稀土发光材料学术研讨会)

Acknowledgements

I would like to extend my heartfelt gratitude to all the people who have ever offered me practical, cordial, and selfless support in my PhD study career, as well as writing this thesis.

First and foremost, my sincere and hearty thanks and appreciations go to my supervisor, Prof. Jianhua Hao, for providing an invaluable chance to complete my doctoral study in The Hong Kong Polytechnic University. His expertise, profound insights, and passionate attitude towards research influenced and encouraged me a lot throughout the duration of my postgraduate research. I genuinely admire his selfless support and assistance to all his students in both research study and personal development. It is my honor to benefit from his personality and diligence, which I will treasure my whole life.

I am grateful to all the esteemed academic and technical staffs of our department for their assistance in equipment utilization for my research work. I would also like to extend my sincere appreciation to my dear colleagues: Dr. Zehan Wu, Dr. Feng Guo, Dr. Man Chung Wong, Dr. Xun Han, Dr. Qilong Cui, Dr. Xinyue Lao, Dr. Qianqian Bai, Dr. Yuan Liu, Dr. Zhaoying Dang, Dr. Weng Fu Io, Dr. Sin-Yi Pang, Dr. Shun Lan, Dr. Yingjin Ma, Dr. Yuqian Zhao, Dr. Fumei Yang, Dr. Lihua Li, Dr. Yuecheng Xiong, Dr. Zhongbin Luo, Dr. Xiao Han, Dr Xingyi Dai, Dr. Haisheng Chen, Dr. Menglin Song, Dr. Yi Wei, Ms. Michael Chan, Mr. Liusheng Huang, Mr. Yudong Peng, Fei Xie, Ms. Liuting Li, and Mr. Yunan Lin for their memorable assistance, stimulating suggestions, genuine companionship, and for all the fun we have had in the last three years.

Most profoundly, I owe an immeasurable debt of gratitude to my cherished family for their steadfast encouragement and unconditional love, which sustained me through both the triumphs and tribulations throughout my life. My deepest and most special thanks flow to my wife, Ms. Man Li, whom I married during my doctoral studies. Her unwavering companionship, profound understanding, and constant encouragement were my bedrock throughout this demanding period. Our co-first-authored life manifests equal contribution to this irreplaceable journey and the future beyond.

Finally, I am grateful to all those who devote much time to reading this thesis and providing me with helpful advice, which will greatly benefit me in my future study and career.

Table of Content

Abstract I

List of Publications IV

Acknowledgements VII

Table of Content IX

List of Figures XII

List of Table XXII

Chapter 1 Introduction 1

1.1 PL properties 1

1.1.1 Photophysical process of PL 1

1.1.2 PL tuning in phosphors 4

1.1.3 Applications of phosphors 5

1.2 Smart phosphor 6

1.2.1 Stimuli-responsive PL modulation in smart phosphors 6

1.2.2 Smart phosphors for information applications 7

1.3 FE thin films 10

1.3.1 Ferroelectricity 10

1.3.2 FE HfO_2 13

1.3.3 Coupling between ferroelectricity and optical properties 15

1.4 Motivation and significance of the research 17

1.5 Research objectives of the thesis 19

Chapter 2 Experimental Techniques 22

2.1 Construction of smart nanocomposites and FE ultrathin films 22

2.1.1 Hard-templated Sol-gel synthesis process 22

2.1.2 The PLD process 23

2.2 Material characterizations 24

2.2.1 Powder X-ray diffraction analyses and Rietveld refinement 24

2.2.2 High-resolution thin-film XRD analyses 26

2.2.3 PL spectroscopy 29

2.2.4 X-ray photoelectron spectroscopy.....31

2.2.5 Scanning transmission electron microscopy 32

2.2.6 Energy dispersive X-ray spectroscopy.....34

2.2.7 Scanning probe microscopy 36

2.2.8 FE tester 38

2.2.9 Synchrotron X-ray absorption Spectrometer 40

2.2.10 Theoretical simulations 41

2.2.11 Software-based offline ANN training.....42

Chapter 3 PL-based Neuromorphic Behaviors in MHPe@MYE Smart Nanocomposites.....44

3.1 Introduction 44

3.2 Construction of MHPe@MYE.....46

3.3 PL kinetics characterizations.....50

3.4 Theoretical insights on dynamic PL variations 52

3.5 PL-based Neuromorphic behaviors.....62

3.6 Summary 73

Chapter 4 Full PL-based Physical Reservoir Computing based on MHPe@MYE Smart Nanocomposites 74

4.1 Introduction 74

4.2 Discrimination of 4-bit binary sequences 78

4.3 PL-based handwritten digit classification 81

4.4 PL-based latent UV fingerprint recognition 86

4.5 Extended PL-based physical reservoir 90

4.6 Summary 98

Chapter 5 PL and FE Er-doped HfO_2 Ultrathin Films with High Endurance 99

5.1 Introduction 99

5.2 Theoretical insights into Er-doping effects 104

5.3 Structural characterizations of HErO thin films 112

5.4 UC and DC PL in HErO thin films 121

5.5 High-endurance ferroelectricity in HErO thin films 126

5.6 Summary 132

Chapter 6 Conclusions and Future Prospects 134

6.1 Conclusions 134

6.2 Future prospects 136

References 138

List of Figures

Figure 1.1 The configurational coordinate diagram featuring a PL process from photoexcitaiton and relaxation to PL emission. 2

Figure 1.2 Periodic table featuring the luminescent metal ions categorized into TM, Ln, and main-group metals with the corresponding typical electron configurations. 3

Figure 1.3 Schematic of physical methods of PL tuning.[12] 5

Figure 1.4 Smart phosphors for various applications. (a) Information encryption.[34] (b)Temperature sensing.[31] (c) Bio-sensing.[33] 10

Figure 1.5 *P-E* hysteresis loop for a conventional FE material.[36] P_{sat}: saturated polarization. P_r: remnant polarization. 11

Figure 1.6 Schematics of key attributes of FE and potential device applications.[50] 13

Figure 1.7 Summary of FE HfO_2 in multiple electronic device applications.[56] 15

Figure 1.8. Research progress on the coupling effects between FE and optical/PL properties. (a) Pioneering work in the fields of FE-PL coupling effect in BTO:Yb/Er thin film.[57] (b) Establishment of electro-PL logics in BTO:Yb/Er thin film.[58] (c) Electro-optical modulation of FE PMN-PT for optical memory.[59] (d) Phase-modulated non-volatile PL in FE quasi-2D perovskite quantum wells for electro-PL logics.[60] 17

Figure 1.9 Structure of the research presented in this thesis. 21

Figure 2.1 Photo of the PLD system used in this research. 24

Figure 2.2 Schematic of operating principle of XRD. 25

Figure 2.3 (a) Optics setup of Ge(220) monochromator for high-resolution thin-film XRD. (b) Comparison of XRD signals using normal PB, Ni-filtered PB, 2-bounce

Ge(220), and 4-bounce Ge(220) monochromator, respectively. (c) full-width at half-maximum (fwhm) parameters of XRD peak using different optics.[62] 27

Figure 2.4 Configurations of thin-film XRD measurements. 29

Figure 2.5. Photo of the Edinburgh FLS 920 spectroscopy used in this thesis.....31

Figure 2.6 Block-diagram of scanning transmission electron microscopy.[63] 34

Figure 2.7 Fundamental principle of energy dispersive X-ray spectroscopy.[64].....35

Figure 2.8 Schematic view of the working principle of AFM.[65] 37

Figure 2.9 Schematic of the pulse sequence for the PUND test. 39

Figure 3.1 Flowchart for the hard-template sol-gel and solvent evaporation synthesis of MHPe@MYE "*smart phosphor*" with light-induced PL variations.[97].....48

Figure 3.2 (a) SEM image of the prepared PMMA mesosphere. (b) SEM image of the porous MHPe@MYE. (c) TEM image of MHPe@MYE. (d) Enlarged TEM image showing the porous structure of PMMA. (e) TEM EDX mapping, the green, yellow and red color represents Cl, Pb, and Y elements, respectively, and (f) the original STEM images with the presence of MHPe NPs cycled in red. The green, orange, and white scale bar indicates 200 nm, 80 nm, and 1 μm, respectively.[97]49

Figure 3.3 XRD refinements showing the phase ratio of MHPe and MYE.....50

Figure 3.4 Time-resolved PL mapping of MHPe@MYE under 365 nm irradiation. .50

Figure 3.5 PL properties of MHPe@MYE under "Read" excitation. (a) The PL kinetics monitoring 510 nm MHPe PL emission variations under 365 nm "Read" excitation. (b) PL emission spectrum measured under 365 nm "Read" excitation. 51

Figure 3.6 Dynamics PL variation under "Write" and "Read" excitation. 52

Figure 3.7 (a) TEM images of MHPe NPs prepared by hot-injection method, inset photo shows bare MHPe NPs colloidal solution under 365 nm UV flashlight. Red scale bar indicates 100 nm. (b) The PL spectra of MHPe NPs. (c) The time-

dependent PL emission mapping of the MHPe NC upon excitation of 365 nm. (d) The SEM images of spin-coated bare MHPe film, inset photo shows the MHPe film under 365 nm UV flashlight. The green-colored bar represents 50 μm. (e) The PL spectra of MHPe film. (f) The time-resolved PL mapping of MHPe film under 365 nm excitation. 54

Figure 3.8 Projected electronic band structure of CPB, CPBC and *v*-CPBC. 56

Figure 3.9 Projected electronic band structure of Y_2O_3 and Y_2O_3:Eu^{3+}. 56

Figure 3.10 (a) The Y_2O_3 surfacial sites of Br/Cl adsorption. (b) Surface energies of Br/Cl adsorbed surfaces. 57

Figure 3.11 3D CDD and charge density diagram of (a) Br and (b) Cl adsorption. The red and blue color mapping area indicates the accumulation and depletion of electrons, respectively. 58

Figure 3.12 NEB migration path and energy barriers. 60

Figure 3.13 Br migration path and the corresponding energy landscape in bulk CPB. 60

Figure 3.14 (a) Schematic of a biological synapse. (b) Schematic illustration of the MHPe@MYE smart nanocomposites with macroporous morphology. (c) Light-triggered PL variation in the MHPe@MYE composites by applying both the optical "Write" and "Read" operation, the tagged figures NO.1-5 representing the specific frames during the light-induced PL variations. (d) Illustrative schemes of microscopic variations at Frame No.1-5 in (c). 62

Figure 3.15 History-dependent PL dynamics of MHPe and inert Eu^{3+} PL dynamics co-existing in MHPe@MYE. 64

Figure 3.16 λ_{em}-dependent synaptic PL dynamics behaviors. 65

Figure 3.17 λ_{ex}-dependent synaptic PL dynamics behaviors. 66

Figure 3.18 Summary of stimuli-dependent synaptic PL dynamics behaviors across various spike parameters. 67

Figure 3.19 *x*-dependent LTM features of MHPe@MYE. (a) Definition of N_t, N_n, N_x, I_t, and I_x marked in the PL dynamics at 30 s resting interval (x = 30 s). (b) LTM behavior featuring the long-term *x*-dependent PL dynamics. (c) PL dynamics comparison with varying *x*. 68

Figure 3.20 Δt-dependent PPF results measured with (a) 0.5 s interval, and (b) 3 s interval. (c) Measured PPF indices against interval times and the fitted decay curves. Error bars indicate the s.d. results from four points. 70

Figure 3.21 (a) PL kinetics during the formation of STP and LTP, the inset figure gives the beginning of PL evolution for STP (green) and LTP (red), demonstrating notable reproducibility(f) PL dynamics during the decay of STP and LTP, and the corresponding fitting curves. Inset displays the fitted decay time constants. 71

Figure 3.22 (a) XRD refinement results of new batch of MHPe@MYE, with the phase ratio tagged. (b) SEM images of new batch of MHPe@MYE. White scale bar indicates 1 μm. (c) time-resolved PL mapping of new MHPe@MYE measured under 360 nm laser excitation. (d) the PL emission spectrum measured at "Read" excitation (λ_{ex} = 365 nm, I_{ex} = 33.121 μW·cm^{-2}). (e) PL kinetic under "Read" excitation (λ_{ex} = 365 nm, λ_{em} = 510 nm, I_{ex} = 33.121 μW·cm^{-2}). (f) The PL dynamics acquired under "Write" and "Read" excitations, demonstrating similar history-dependent PL variation behaviors. 72

Figure 4.1 (a) Illustration of the FNN with acyclic and trainable connections, (b) the untrained connections within the network of a reservoir computing.[110] 75

Figure 4.2 Examples of physical reservoir computing based on materials' chemical and physical properties with non-linear characteristics. (a) All-optical physical

reservoir computing based on light-responsive organic materials.[112] (b) In-sensor reservoir computing phototransistors hardware based on GaO_x.[113] (c) Electrical physical reservoir computing based on oxygen ion dynamics of HZO/LSMO thin films.[114] (d) Mixed-mode physical reservoir computing based on FE α-In_2Se_3.[115] 76

Figure 4.3 Waveform setups of 4-bit binary sequence 79

Figure 4.4 16 distinct PL dynamic features correspond cv to all 4-bit binary sequences. 79

Figure 4.5 (a) Configurations of SMP points in the PL dynamic features. (b) The extracted readout intensities of SMP1, SMP2, SMP3, and SMP4..... 80

Figure 4.6 2D PL feature maps for distinguishing 4-bit binary sequences..... 81

Figure 4.7 Example of image preprocessing of MNIST..... 82

Figure 4.8 (a) Crop of MNIST image into width of 4 pixels, and (b) the consequent rejoining of cropped images to form 4-bit strips. 83

Figure 4.9 Device setups using extracted PL features mapped from experimental results. 84

Figure 4.10 Training records for MNIST handwritten digit classification..... 85

Figure 4.11 Confusion matrix of MNIST classification using Dev1 dual-SMP setup. 85

Figure 4.12 Flowchart of latent PL-based UV fingerprint recognition using MHPe@MYE as physical reservoir..... 87

Figure 4.13 Examples for comparing the *Ostu* and adaptive threshold binarization method for 64 × 64 resized SOCOFing images..... 88

Figure 4.14 Crop and rejoin process for SOCOFing fingerprint images..... 88

Figure 4.15 (a) Offline software-based ANN training methods. Training record of SOCOFing fingerprint recognition using MHPe@MYE as PL-based physical reservoir using (b) 64 × 64, and other resized scheme including (c) 96 × 96, (d) 48× 48, and (e) 32× 32 fingerprint images. 90

Figure 4.16 Summary of accuracy and loss metrics among difference resize of SOCOFing.....90

Figure 4.17 Conceptual investigation of PersL-based all-PL reservoir properties. (a) PL emission spectra of PersL phosphor $Sr_2MgSi_2O_7:Eu^{2+},Dy^{3+}$ (blue), SAO (green), and $CaS:Eu^{2+}$ (red) under 365 nm excitation. The "Write-only" feature spaces of potential all-PL 4-bit reservoir using (b) blue PersL of $Sr_2MgSi_2O_7:Eu^{2+},Dy^{3+}$ with 3 Hz light pulse input, (c) green PersL of SAO with 1 Hz light pulse input, and (d) red PersL of $CaS:Eu^{2+}$ with 1.5 Hz light pulse input. Inset diagrams show the corresponding excitation waveforms of light stimuli...92

Figure 4.18 Schematical illustration of the different neuromorphic PL behaviors between existing (a) "Write-only" systems and (b) The constructed variation-type "Write & Read" MHPe@MYE "*smart phosphor*".....93

Figure 4.19 Schematic illustrations of the importance of distinct "Read" operations showing potential prospects in information security, anti-interference, and parallel operation. 95

Figure 4.20 Comparison studies of PL-based physical reservoir for fingerprint recognition without distinct "Read" mechanism. (a) Recognition accuracy and (b) amounts of feature-loss events for 4 different scenarios. (c) Recognition accuracy and (d) number of feature-loss events for different image resizing.....98

Figure 5.1 (a) Review of FE HfO_2, their utilization in various FE devices, and the related cutting-edge applications. Crucial impact of dopants from various aspects,

such as (b) $HfZr_{(1+x)}O_2$ stabilized in alternative FE phase structure,[139] and (c) enhanced polarization switching dynamics in LT:HfO_2.[145] 101

Figure 5.2 Schematic of the research design and key results in this chapter. (a) Illustration of the FE and PL dual-mode HErO thin film. (b) DFT Simulated phase energy of HfO_2 in diffenrent phase. (c) The PUND test of HErO. (d) Benchmarking FE properties of HErO against other dopants. (e) DFT simulation on introctin of the optical-active localized Er 4*f* states. (f) Experimental measured UC and DC PL from HErO at ultrathin films (~11 nm). 103

Figure 5.3 (a) The crystal structure of FE o-HfO_2, the displacive oxygen layer and the fixed oxygen layer during FE polarization are painted in green and blue, respectively. (b) The ionic radius of candidate dopants at 6-fold (for *m*-phase) and 7-fold (for *o*-phase) CN including Yb, Er, Y, and Zr against the pristine Hf. ... 105

Figure 5.4 Phase energies of FE HfO_2 doped with various dopants normalized to the total energies of non-FE *m*-phase, correspondingly. 106

Figure 5.5. Calculated P_z of (b) HErO, (c) HYO, and (d) undoped FE HfO_2. (d) The energy landscapes of the entire polarization-switching process of HErO, HYO, and undoped HfO_2, the inset shows the crystal structures of the initial polarization-down *Pca2₁*, the centrosymmetric *Pbcm*, and the final polarization-up *Pca2₁* states. 107

Figure 5.6 (a) Diffusion paths of $V_O^{\cdot\cdot}$ in metal-ion-doped FE HfO_2. The red, blue and green arrow indicates the migration of $V_O^{\cdot\cdot}$ from O1 to O1, from O1 to O2, and from O1 to O2, respectively. The cycled area indicates the $V_O^{\cdot\cdot}$ migration process close to the metal-ion dopants (tagged as Adjacent) or far from the metal-ion dopants (tagged as Far). (b) The NEB energy landscape of the $V_O^{\cdot\cdot}$ migration process..... 109

Figure 5.7 Binding energy (E_b) as a function of distance between Er and V_O. 110

Figure 5.8 A comparison between the calculated electronic band structures and projected DOS between (a)(b) HErO and (c)(d) HYO. 111

Figure 5.9. (a) the XRD 2θ-ω scan of HErO/LSMO/STO(001) thin films at various thickness, and the rocking curves of (111) plane in (b) LSMO and (c) 11-nm-thick HErO. (d) The XRR and fitting results of the HErO/LSMO/STO(001) thin films. (e) The azimuthal φ scan results of the 11-nm-thick HErO/LSMO/STO(001) thin film at $\chi = 71^o$.....114

Figure 5.10. (a) XRD 2θ-ω scans around the $\{002\}_{pc}$ planes of HErO at various φ angles. (b) A comparison between the XRD of in-plane and out-of-plane $\{111\}_{pc}$ planes. 116

Figure 5.11. φ scans aiming at HErO (-111) with different thickness. 116

Figure 5.12. (a) Low-magnitude HAADF-STEM and the corresponding EDX mapping of (c) Er, (c) Hf, (d) Mn, (e) Sr, (f) Ti, (g) O in the 11-nm-thick HErO/LSMO/STO(001) thin film. The white bar indicates 10 nm. 117

Figure 5.13. EDX spectra selected on the HErO layer, inset shows the atomic fraction of HErO in the thin film. 118

Figure 5.14 The HErO/LSMO/STO epitaxial thin films at the large field of view. .118

Figure 5.15 iDPC and HAADF STEM images of (a) interfaces between HErO/LSMO layer and (b) atomic layouts of Hf/Er and O as superposed by the crystal structure. 119

Figure 5.16 XPS spectra of Hf 4f and Er 4d in 11-nm-thick HErO. 120

Figure 5.17. (a) Schematic of the PL properties of epitaxial HErO/LSMO/STO thin films. (b) The energy level profile of Er^{3+}, instructing the UC and DC transition pathways. 121

Figure 5.18 The UC (upper) and DC (lower) PL spectrum of the 11-nm HErO under 980 nm excitation. 122

Figure 5.19 (a) Excitation-power-dependent UC PL and (b) Excitation-power-dependent DC PL in HErO. (c) The plotted excitation-power-dependent PL intensity for investigating the photon conversion amounts in the PL process... 123

Figure 5.20 PL decay and the corresponding fitting curve of (a) $^2S_{3/2} \rightarrow {}^4I_{15/2}$ (I_{534}) and (b) $^4F_{9/2} \rightarrow {}^4I_{15/2}$ (I_{650}) UC PL, as well as (c) $^4I_{13/2} \rightarrow {}^4I_{15/2}$ (I_{1534}) DC PL under 980 nm excitation. 124

Figure 5.21 (a) XRD of the HErO targets. (b) UC PL spectrum of the HErO targets. (c) Schematic illustration of combining XRD and PL results for determining the phase composition of HErO. 126

Figure 5.22 (a) The microscopic hysteresis loop of the ~11-nm PLD-deposited HErO thin film. (b) The AFM image and (c) the phase image after PFM domain patterning of HErO, where the inset shows a line scan of phase contrast of the tagged cyan line. 127

Figure 5.23 FE properties of 11-nm-thick HErO (a) PUND *P*-*E* and *I*-*E* measurements. (b) *C*-*E* measurements. (c) Retention test with logarithmic fitting with extrapolated 10-year expectation. 128

Figure 5.24 Endurance test of 11-nm-thick HErO. (a) Fatigue tests of 10^{11} cycle at 1MHz. (b) The *P*-*V* and (c) *I*-*V* tests during fatigue tests. 129

Figure 5.25 Endurance test at other parameters. (a) Fatigue tests at 7.5 MV/cm. (b) Fatigue tests at 7.5 MV/cm. (c) Fatigue tests at 10 MHz. (d) Fatigue tests at 100 kHz. 130

Figure 5.26 O *K*-edge XAS of pristine HErO and after 10^2 to 10^{10} switching cycles. 131

Figure 5.27 Benchmarking of HErO against other FE HfO_2. 132

List of Table

Table 4.1 Comparison of existing PL-based neuromorphic systems. …….93

Chapter 1 Introduction

1.1 PL properties

1.1.1 Photophysical process of PL

PL refers to the emission of electromagnetic radiation in the UV to NIR range resulting from photon-induced electronic excitation and subsequent radiative relaxation in luminescent materials. Upon absorption of high-energy photons, electrons are promoted from the ground state to excited states, followed by rapid non-radiative relaxation to the lowest excited state according to the Kasha's rule.[1] The energy is eventually released in the form of light emission, given that the radiative transition is allowed to take place. The configuration coordinate diagram is often used to describe the luminescent process (**Figure 1.1**). The diagram describes the correlation between the internuclear separation of the bond (R) and energy (E). The electronic levels are represented by each quadratic curve in the R-E diagram, and the quantized vibronic levels of electric states are represented by the parallel longitudinal waves plotted within each quadratic curve (black dotted lines). Since the electronic transitions are rather instantaneous with reference to nuclear motions, the electronic transitions are considered to happen instantly with a fixed nuclear position (constant R), which is also known as the Franck-Condon principle of transitions.[2] It is illustrated by the vertical electric transitions of both the excitation and emission processes (orange and purple arrows in **Figure 1.1**).

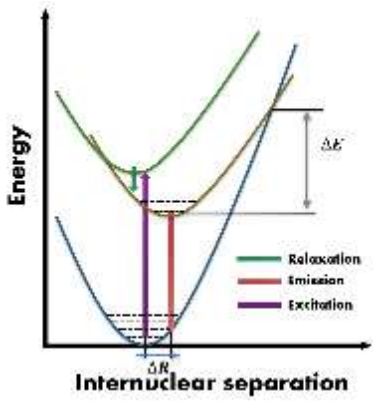

Figure 1.1 The configurational coordinate diagram featuring a PL process from photoexcitaiton and relaxation to PL emission.

Up-conversion (UC) luminescence is a particular nonlinear optical process. UC luminescence is based on two-photon or multi-photon excitation processes mediated by energy transfer (ET). Specific metal ions can absorb or receive the energy of two or more photons successively to transit from the ground state to the higher excited states. The various UC pathways include ET UC, energy migration UC, excited-state absorption (ESA) after ground-state absorption (GSA), cooperative sensitization UC, photon avalanche (PA) UC, as well as the interfacial ET.[3-5] Consequently, the accumulation of photon energies in the process leads to the emission of a high-energy photon. UC luminescence is particularly advantageous for applications such as displays, lasers, and bioimaging, as it allows for visible emission under NIR excitation, reducing background interference and minimizing photodamage in sensitive environments.

As shown in the periodic table in **Figure 1.2**, all the available luminescent metal ions can be divided into three categories as marked correspondingly in different regions, which are transition-metal (TM), lanthanide (Ln), and main-group metal ions. Ln ions are known for their sharp 4*f*-4*f* (Eu^{3+}, Er^{3+}, Tb^{3+}, Sm^{3+}, *etc.*) intraconfigurational

transitions with long PL decay lifetimes, owing to the shielding of outer electrons from the crystal field. In contrast, TM ions typically display broader *d-d* transitions with shorter lifetimes as they are less shielded by the outer orbitals than Ln.[6] As for the main-group metal ions represented by Pb^{2+}, Sb^{3+}, and Bi^{3+} with ns^2 configurations, their luminescence process is more semiconductor-like (between *s* and *sp* hybridized states), and commonly involves hybridization with ligands.[7] The phenomenon can be exemplified by lead halide perovskite, which exhibits pronounced *sp* hybridization between the Pb $6s^2$ lone pair and the *p* orbitals of halogens.[8] These differences enable a wide range of functionalities in photonic materials, supporting diverse applications in lighting, sensing, and information processing.

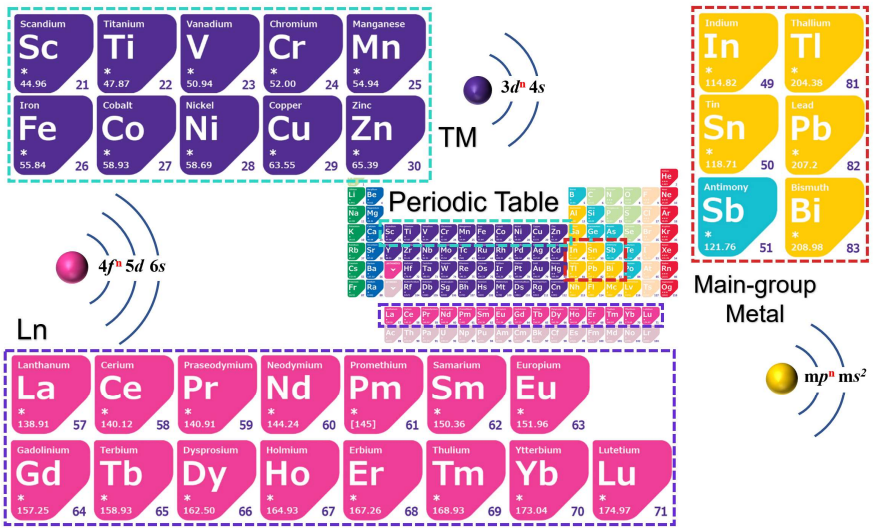

Figure 1.2 Periodic table featuring the luminescent metal ions categorized into TM, Ln, and main-group metals with the corresponding typical electron configurations.

1.1.2 PL tuning in phosphors

PL tuning in phosphors fundamentally alters emission properties by modifying the electronic energy levels, crystal field environments, or band structures. This is done by applying adjustments to dopant configurations, host lattice symmetry, or quantum confinement effects. Based on the underlying tuning mechanisms, PL modulation can be categorized into chemical and physical methods.[9]

Chemical methods enable tuning by permanently altering intrinsic material properties during synthesis.[10] These approaches include varying activator concentrations, modifying host compositions, controlling nanocrystal dimensions, or functionalizing surface ligands. Such modifications directly influence electronic energy transitions and defect states, resulting in shifts in emission wavelengths or intensities. Physical methods achieve dynamic and reversible tuning through external stimuli, such as the electric fields with Stark shifts of PL, magnetic fields with Zeeman splitting. More profound physical tuning can be achieved by applying mechanical stress, temperature variations, plasmonic couplings, or radiation (**Figure 1.3**).

Both of the approaches demonstrate effectiveness because they target fundamental PL mechanisms. Chemical methods can provide the stable modifications through permanent structural changes, while physical methods offer real-time control by externally manipulating same underlying electronic and structural properties as well. In addition, these external stimuli modify the phosphor's electronic structure without chemical alteration, which leads to a class of stimuli-responsive phosphorus, or namely, "*smart phosphors*".[11] This dual capability enables both fixed-property phosphors for specific applications and potentially adaptive systems for dynamic PL control.

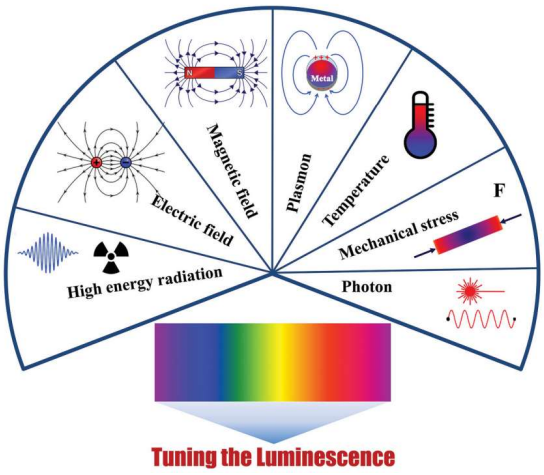

Figure 1.3 Schematic of physical methods of PL tuning.[12]

1.1.3 Applications of phosphors

The most conventional and industrialized application of phosphors lies in the solid-state lighting, particularly through the phosphor-converted light-emitting diodes (pc-LEDs).[13 14] It has transformed illumination and display technologies by achieving higher energy efficiency and better environmental sustainability. Phosphor materials serve as critical components in these systems, converting blue or UV LED emission through the down-conversion (DC) pathway into visible light emission for applications including the general lighting and displays. The evolution of phosphors has progressed through distinct generations. The initial materials prioritized high luminous output for basic white lighting applications, until the discovery of YAG with both ultrahigh stability, quantum efficiency, and preferred blue absorption.[15,16] Subsequently, the developments of phosphors start to focus on enhancing color rendering indices through the introduction of red- and cyan-emitting phosphors,[17,18] as well as narrow-band emitters for backlighting systems where color gamut performance is required.[19] Recent developments target broadband NIR phosphors for specialized functions such as health

monitoring and plant cultivation.[20,21] Other breakthroughs have also been made in ceramic phosphors designed for high-power light sources.[22] Despite these strides, ongoing challenges still persist, including balancing luminous efficacy with color quality and ensuring thermal and chemical robustness at operational temperatures up to 150 °C; The discovery and engineering of such materials remains essential for advancing the performance and versatility of solid-state lighting across many diverse lighting and backlight display applications.[23,24]

1.2 Smart phosphor

1.2.1 Stimuli-responsive PL modulation in smart phosphors

"*Smart phosphor*" represents a class of luminescent materials with emission properties that can be dynamically and reversibly modulated by external stimuli.[11] The stimuli can range from electric or magnetic fields, mechanical stress, temperature, and light. Unlike conventional phosphors, whose luminescence characteristics are largely fixed after the syntheses, "*smart phosphors*" are designed to integrate the functional attributes of smart materials with the optical activity. This is achieved through strategic coupling between the host matrix and activator ions, often leveraging properties such as piezoelectricity, ferroelectricity, or magnetostriction to mediate the interaction between external stimuli and the luminescent centers.[11]

For example, in a piezoelectric-coupled "*smart phosphor*" system such as ZnS:Mn thin films integrated on a PMN-PT ($Pb(Mg_{1/3}Nb_{2/3})O_3$-$PbTiO_3$) piezoelectric substrate, the application of an electric field induces strain in the PMN-PT, which is then transferred to the ZnS:Mn layer.[25] Consequently, the local crystal field environment of

the Mn^{2+} dopant ions is altered, thereby modulating both the PL intensity and spectral profile in a reversible manner. Additionally, in light-driven photochromic "*smart phosphors*" such as Er^{3+}-doped $Na_{0.5}Bi_{2.5}Nb_2O_9$, exposure to specific wavelengths of light induces reversible formation of color centers in the host, which interact with the emission bands of Er^{3+} ions and enable dynamic modulation of luminescence through ET processes.[26] These stimuli-responsive mechanisms not only provide new degrees of freedom for controlling light emission but also open up opportunities for multifunctional optoelectronic devices, adaptive displays, and advanced sensing platforms. The development of "*smart phosphors*" thus marks a significant advance in the field of optical functional materials, offering both fundamental insights and practical pathways toward intelligent photonic technologies.

1.2.2 Smart phosphors for information applications

Building upon the unique stimuli-responsive PL modulation described above, "*smart phosphors*" offer distinct advantages for information-related applications. Their ability to undergo controlled and reversible changes in emission properties under external stimuli enables the direct encoding, concealment, and dynamic retrieval of information using visible light that are observable to the naked eye or simple devices.[27] [28] Besides, "*smart phosphors*" also exhibit other advantages in information encryption and memory storage like the stimuli-responsive optical properties, high color purity, tunable lifetimes, and dynamic behavior under external triggers (**Figure 1.4a**). These characteristics enable the creation of sophisticated anti-counterfeiting systems with enhanced security and multidimensional encryption capabilities.[29] For instance, the time-dimension encryption exploits PersL luminescence decay rates, where varying

doping concentrations of ions like Cr^{3+} or Pr^{3+} generate distinct afterglow durations and color shifts, allowing hidden information (*e.g.*, codes, letter, symbols, patterns, *etc.*) to emerge sequentially post-excitation. Photon-controlled binary storage leverages plasmonic effects in materials such as Y_2O_3:Eu^{3+}-Au, where specific laser powers write ("1") or quench ("0") luminescence states, achieving self-encrypted data storage readable only under precise optical conditions.[30] These approaches ensure high-security information concealment through dynamic, multilevel verification mechanisms without specialized equipment.

Beyond information encryption, the stimuli-responsive characteristics of "*smart phosphors*" also make them promising candidates for information sensing, including temperature monitoring and ultrasensitive biological detection. Recent advances in luminescent thermometry have established "*smart phosphors*" as highly effective materials for temperature sensing, owing to their non-contact, ratiometric, and self-referenced measurement capabilities. The primary mechanism relies on the luminescence intensity ratio between emissions from thermally coupled excited states, such as the $^2H_{11/2}$ and $^4S_{3/2}$ levels of Er^{3+} ions, whose population ratio follows the Boltzmann distribution and therefore vary predictably with temperature. This approach enables accurate temperature readouts that are largely independent of excitation power fluctuations and environmental interference. Recently, the PL-based ratiometric optical fiber thermometry was developed based on $NaLaTi_2O_6$:Yb/Er phosphors as shown in **Figure 1.4b**, enabling an *operando*, solitary, and high-fidelity temperature monitoring within working Li-ion batteries.[31] It can achieve exceptional temperature measurement accuracy of ±0.12 °C, which is higher than conventional optoelectronic counterparts. It also demonstrated robust stability against environmental disturbances.

Furthermore, the advancement of smart luminescent materials, particularly UC nanoparticles (NPs), in biosensing leverages their unique photophysical properties for high-sensitivity pathogen detection. The core mechanism involves anti-Stokes processes like ET UC, where Ln ions (*e.g.*, Yb^{3+}/Er^{3+}) convert NIR photons to visible/UV emissions, enabling deep-tissue penetration and minimal photodamage. Coupled with Förster resonance ET (FRET), UC NPs act as donors to quenchers (*e.g.*, Au NPs or graphene quantum dots), with ET efficiency modulated by analyte proximity, facilitating real-time, label-free detection. Most importantly, PL-based biosensing significantly enhances sensitivity and achieves ultra-low limits of detection (LoD). Recent works demonstrate high accuracy achieved by $BaGdF_5:Yb^{3+}/Er^{3+}$ UC NP-AuNP FRET assays, showing limits of detection of 7 pM for avian influenza virus H7 genes and 300 fM for Ebola oligonucleotides.[32] The high sensitivity PL sensing can be directly integrated with camera and machine vision analyses (**Figure 1.4c**), achieving LoD of 0.021 ng/mL for carcinoembryonic antigen that surpasses commercial lateral flow assay strips by ~100-fold.[33]

In summary, "*smart phosphor*" has already demonstrated broad applicability across information encryption, temperature sensing, and biosensing. Their unique combination of stimuli-responsive PL, high sensitivity, and versatility continues to drive innovation in fields ranging from information security and optical data storage to biomedical diagnostics, underscoring their significance as multifunctional platforms for next-generation information and sensing technologies.

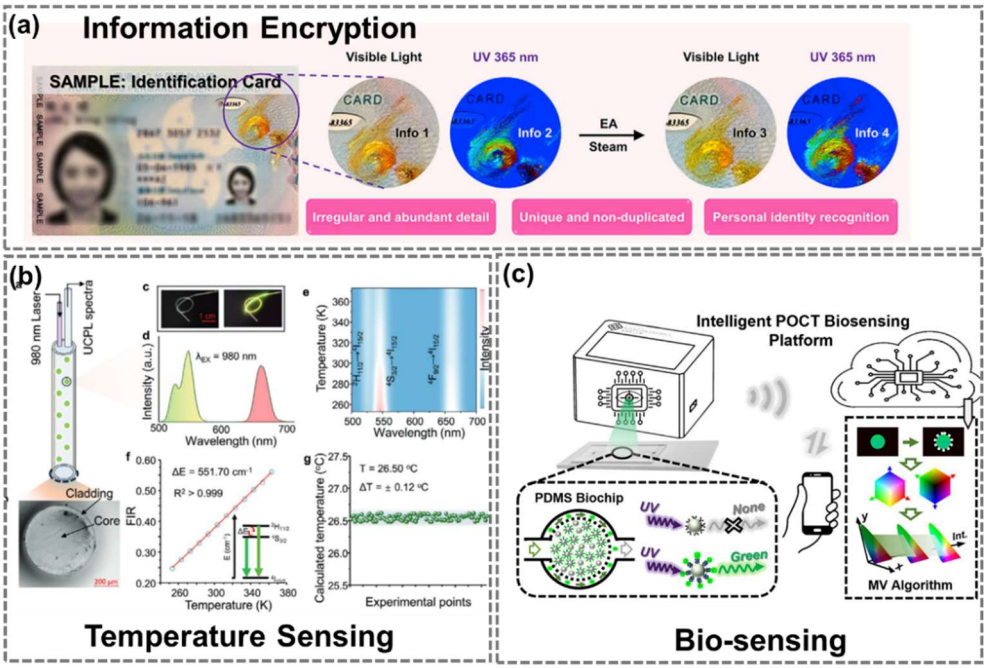

Figure 1.4 Smart phosphors for various applications. (a) Information encryption.[34] (b)Temperature sensing.[31] (c) Bio-sensing.[33]

1.3 FE thin films

1.3.1 Ferroelectricity

Ferroelectrics are a class of dielectric materials that possess a spontaneous electric polarization. This polarization can be reversibly switched by applying an external electric field exceeding the coercive field (E_c) of the FE material.[35] Generally, as the temperature exceeds the Curie temperature (T_c), the spontaneous polarization in FE materials will vanish, associated with a structural transformation from a non-symmetric FE phase to a high-symmetry non-polar paraelectric phase. The macroscopic

spontaneous polarization of FE materials can be characterized by the polarization-electric field (*P*-*E*) hysteresis loops (**Figure 1.5)**. Materials possessing piezoelectric and FE properties hold great potential for the developing functional devices including actuators, sensors, energy harvesters, synapses, and data storage devices, driving advancements in technology.

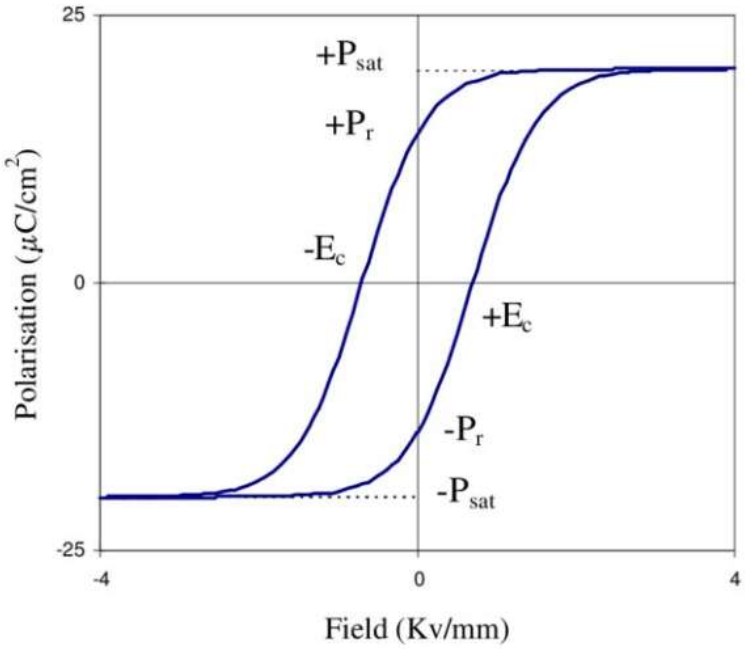

Figure 1.5 *P*-*E* hysteresis loop for a conventional FE material.[36] P_{sat}: saturated polarization. P_r: remnant polarization.

The discovery of ferroelectrics can be dated back to the early 1920s, where Valasek report the first demonstration of ferroelectricity in the Rochelle salt.[37] Since then, extensive efforts have been devoted to discovering new FE materials.[38] The most investigated FE materials have been oxide perovskites with general formula of ABO_3, where A can range from alkali earth, TM, to Ln ions, whereas B is mostly chosen from

TM ions.[39,40] The ferroelectricity in these perovskites arises from a structural phase transition at the T_c. For example, $BaTiO_3$ (BTO) transforms from the high-symmetry and paraelectric cubic phase to the non-symmetric tetragonal FE phase. During the process, relative displacements between the cations (*e.g.*, B-site metal) and the anion (oxygen) sublattice occur spontaneously along a specific crystallographic axis, breaking inversion symmetry and generating the stable and switchable spontaneous polarization along the axis within the unit cell. These dipoles can be persistently remanent until switched by reverse bias or gradually faded due to the depolarization fields. Again, taking the most representative FE material of BTO as an example, a displacement of 0.05 Å was found in the Ti ion at the body center along +*b* direction upon applying electric fields. At the same time, oxygen atoms are displaced 0.08 Å in the -*b* direction.[41] Therefore, a spontaneous electric dipole is thus formed. Comprehensive research on FE materials and their unique electrical properties has significantly advanced the understanding of FE mechanisms and the discovery of novel FE materials. Notably, emerging FE materials demonstrate a distinct trend towards miniaturization into the two-dimensional (2D) and ultrathin regimes (**Figure 1.6)**.[42] The family of FE materials has been substantially expanded beyond traditional oxide perovskites to include organic FE polymers, hybrid organic-inorganic halide perovskites, and particularly 2D materials such as α-In_2Se_3,[43] $CuInP_2S_6$,[44,45] and WTe_2,[46,47] alongside with engineered heterostructures and exfoliated ultrathin freestanding membranes.[48,49]

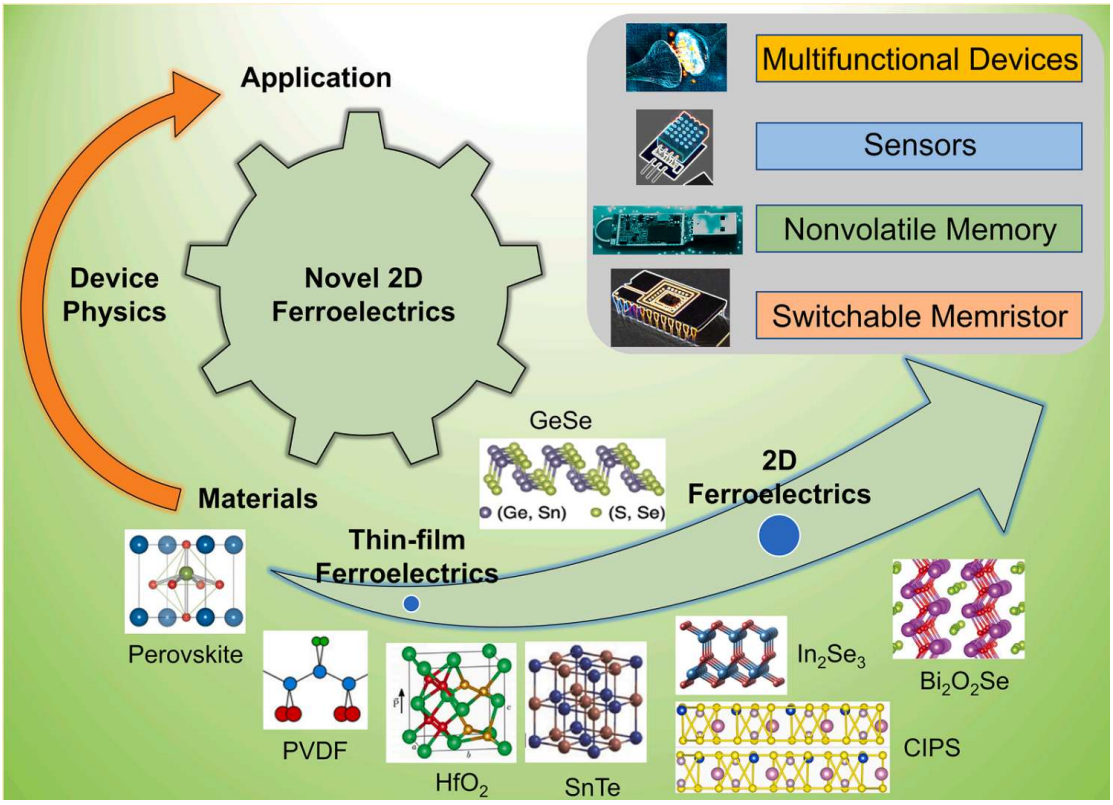

Figure 1.6 Schematics of key attributes of FE and potential device applications.[50]

1.3.2 FE HfO_2

HfO_2 is a simple binary metal oxide. It has long been recognized for its high-*k* dielectric properties.[51] However, a paradigm shift occurred in 2011 with the discovery of FE in the thin and Si-doped polycrystalline HfO_2 films.[52] This fluorite-structured material features a metastable polar orthorhombic (*o*-) phase ($Pca2_1$) that enables spontaneous polarization switching, facilitated by singly oxygen anion displacement rather than metal cation off-centering typical of perovskite ferroelectrics. Since then, FE HfO_2 oxide has attracted significant attention in recent years due to its unique combination of CMOS compatibility, scalability, and robust FE at ultrathin thicknesses. Unlike traditional perovskite ferroelectrics, FE HfO_2-based films maintain stable FE polarization even at thicknesses below 10 nm, which is the ultrathin scale compared to

conventional oxide and polymer ferroelectrics. The ferroelectricity in hafnium oxide is primarily associated with the stabilization of the non-centrosymmetric *o*-phase, which can be achieved through various processing conditions and, in some cases, appropriate doping. The reported P_r values typically ranging from 10 to 30 μC/cm^2. However, major challenges also persist in front of practical applications of FE HFO_2, including the electrical wake-up effect, insufficient endurance, retention loss, imprint, and device-to-device variability arise from oxygen vacancies and phase instability.[52]

Recent advances have focused on understanding the scaling behavior, domain dynamics, and the influence of interfaces and grain boundaries on device performance. State-of-the-art studies have demonstrated the integration of HfO_2 ferroelectrics into FE field-effect transistor (FET) and capacitors, achieving sub-10 nm device dimensions with low operating voltages and high endurance. Furthermore, emerging research is exploring the potential of HfO_2-based materials in neuromorphic computing and negative capacitance (NC) devices.

As extensively summarized in **Figure 1.6**, FE HfO_2 has demonstrated significant potential in a wide range of FE devices. The early work on initial planar FE FETs with Si-doped HfO_2 gate dielectric was fabricated just one year after the discovery of FE HfO_2.[53] It demonstrated nonvolatile memory functionality at 28 nm channel lengths, which can be used for binary data storage at highly compatible scales. Fin-type FE FETs designs further improved gate controllability and achieved operational speeds reaching the GHz range, suitable for central processing unit applications. The adoption of gate-all-around (GAA) configurations provides superior electrostatic control, effectively suppressing the short-channel effects and hence facilitating device scaling.[54] In the meantime, the NC effect in FE-HfO_2-based NC-FETs enables the pursuit of sub-

60 mV/decade subthreshold swing, offering a pathway to overcome the Boltzmann limit for ultralow-power switching.[54] Very recently, the integration of FE HfO_2 as FE gate on GaN-based high-electron-mobility transistors achieves simultaneous increase in the ON current and decrease in the leakage current.[55] Collectively, these implementations across varied transistor architectures validate FE HfO_2 as versatile materials for next-generation electronic devices (**Figure 1.7**). The continuous evolution in related device structures also underscores the adaptability of FE HfO_2 to increasingly demanding semiconductor technology.

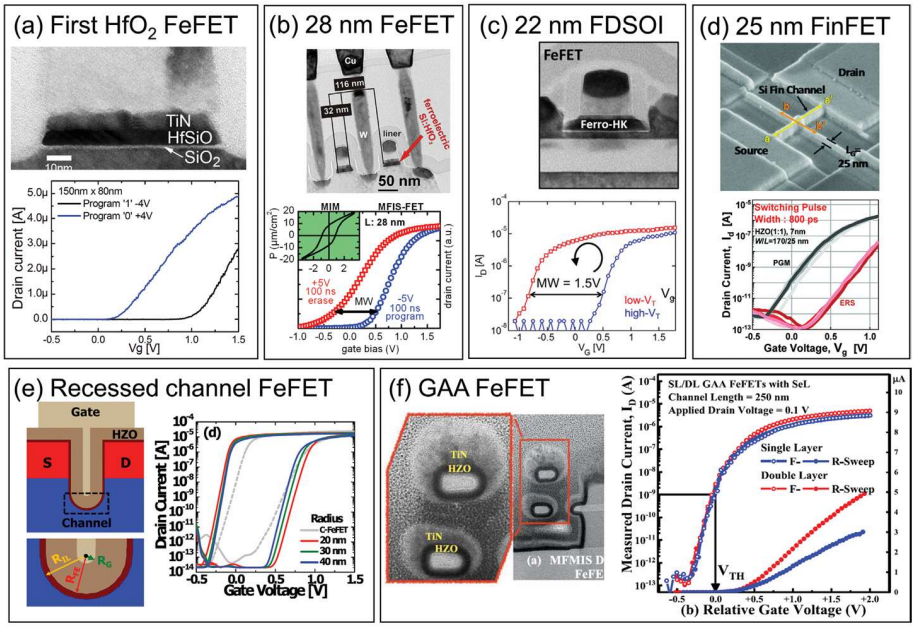

Figure 1.7 Summary of FE HfO_2 in multiple electronic device applications.[56]

1.3.3 Coupling between ferroelectricity and optical properties

Electro-optical coupling leverages the reversible polarization and strain effects inherent in FE/piezoelectric materials to dynamically manipulate optical processes. FE

gating exploits the ultrahigh dielectric constant and hysteretic *P-E* response of perovskite oxides (*e.g.*, BTO, PMN-PT) to nonvolatility modulate carrier density and band alignment in adjacent semiconductors, as demonstrated in MoS_2-based photodetectors where FE Poly(vinylidene fluoride) polymer gating significantly enhanced responsivity and extended spectral response to ~1550 nm. Concurrently, piezoelectric strain engineering utilizes giant piezoelectric coefficients to induce biaxial strain through converse piezoelectric effects, enabling in-situ tuning of semiconductor band structures.

The coupling between PL and FE was pioneered by our group in the year of 2011 in the Er^{3+}-doped in FE BTO thin films, which arises from the hypersensitive response of Er^{3+} activators to the local crystal-field symmetry.[57] It can be dynamically altered by FE polarization switching by applying external electrical fields. The electric-field-induced lattice distortion selectively enhanced the hypersensitive green UC PL transitions by 270% (**Figure 1.8a**). Such coupling effect further leads to the electro-PL modulation for construction of dual-mode logics (**Figure 1.8b**).[58]

In the meantime, the non-volatile electro-optic modulation can be achieved in FE PMN-PT crystals.[59] By applying electrical pulses, the alignment of FE domains in PMN-PT can be precisely controlled, enabling stable and multi-level changes in refractive index and optical phase (**Figure 1.8c**). The mechanism relies on FE domain engineering, where switched domains enhance the electro-optic effect and allow programmable phase shifts. The demonstrated electro-optical modulation shows fast switching within 100 ms, low energy consumption of 234 nJ. Similarly utilizing FE domain control, PL tuning can be achieved in the metal-ion-luminescence in hybrid halide perovskites. Researcher synthesized Mn-doped $(BA)_2CsPb_2Br_7$ to achieve

tunable PL modulation by FE domains and lattice distortion.[60] The films show excellent stability and FE properties, enabling multi-state signal encoding and logic gate functions based on non-volatile and multistate PL multiplexity (**Figure 1.8d**).

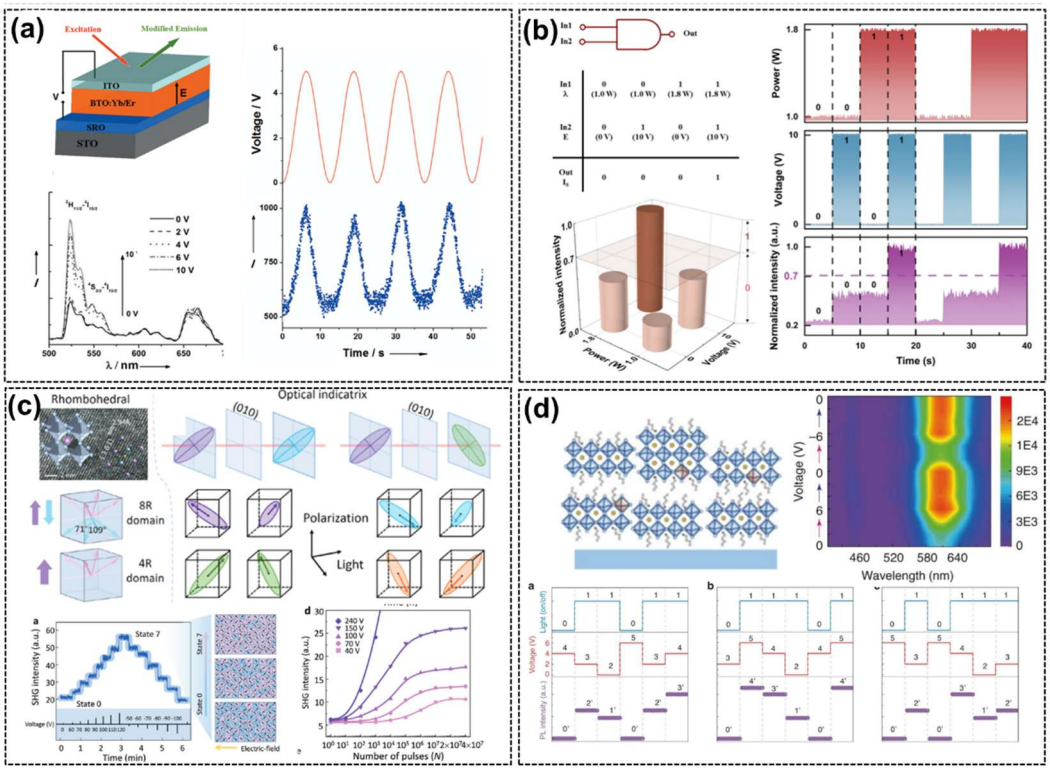

Figure 1.8. Research progress on the coupling effects between FE and optical/PL properties. (a) Pioneering work in the fields of FE-PL coupling effect in BTO:Yb/Er thin film.[57] (b) Establishment of electro-PL logics in BTO:Yb/Er thin film.[58] (c) Electro-optical modulation of FE PMN-PT for optical memory.[59] (d) Phase-modulated non-volatile PL in FE quasi-2D perovskite quantum wells for electro-PL logics.[60]

1.4 Motivation and significance of the research

The motivation for this research arises from the increasing demand in the information era for advanced multimodal information processing capabilities that

transcend traditional electrical approaches. In the information era, the exponential increase in data volume and complexity, together with the widespread emergence of multimedia information sources, has highlighted the inadequacies of traditional electrical paradigms in meeting the demands of modern information processing. As light being the most common media of information, PL has long served as a cornerstone for optical information storage and display. Nevertheless, existing PL-based systems are predominantly restricted to static or passive functionalities, with their dynamic and neuromorphic capabilities remaining largely unexplored. There is mounting need for phosphor materials to go beyond the boundaries of singly stimulus-responsive mechanisms, and to exhibit sophisticated functionalities as in-memory information processors. On the other hand, the practical application of PL-based mechanisms in information processing faces significant obstacles related to miniaturization and integration. As device architecture continues to scale down to the ultrathin and nanoscale dimensions, PL-active materials are increasingly susceptible to quenching effects, reduced emission intensity, and compromised uniformity; all of which collective diminish their effectiveness for potential dynamic optical information processing ability. These scaling challenges not only impair PL efficiency but also hinder the integration of PL functionalities with other main-stream platforms, such as the electronic systems, thereby constraining the realization of multifunctional and multimodal devices.

Motivated by these challenges, this research seeks to pioneer the use of PL in smart nanocomposites to first examine the potential of PL-based from the dynamic aspects and explore PL-based information processing. The work further intends to explore the integration of PL into FE ultrathin films, aiming to establish novel and multi-mode

information processing platform at the nanoscale, aiming to unlock the full potential of PL for as the emerging information technologies.

1.5 Research objectives of the thesis

As illustratively displayed in the flowchart in **Figure 1.9**, the main objectives of the present work are:

1. To construct smart nanocomposites with PL-based neuromorphic behaviors, and to examine the feasibility of neuromorphic computing based on PL functions.
2. To integrate PL functions into FE HfO_2 at ultrathin-film scale for future dual-mode devices.

The thesis is structured into six chapters as follows:

Chapter 1: **Introduction**. This chapter first presents a general background of the photophysical process of PL. Their widespread applications in information storage, display, lighting, and sensing are then discussed. Next, the concept of "*smart phosphor*" with stimuli-responsive PL modulation and their emerging applications has been introduced. Finally, the structure of the research objectives is schematically illustrated.

Chapter 2: **Experimental methods**. This chapter describes the major experimental procedures used for materials preparation and thin-film growth in this thesis. The characterization methods as well as their mechanisms are then described. Lastly, theoretical simulations and software-based ANN simulation setups are introduced.

Chapter 3: MHPe@MYE smart nanocomposites with PL-based neuromorphic behaviors. This chapter reports on the construction of porous smart nanocomposites MHPe@MYE with light-induced and dark-recoverable dynamic PL properties. Their

PL variation process exhibits synaptic-like behaviors, including PPF, LTM, and both short- and long-term potentiation (STP and LTP), closely mimicking biological synaptic plasticity. The system also enables distinct "Write" and "Read" operations through PL functions, establishing the platform for all-optical neuromorphic functionalities with high reproducibility.

Chapter 4: PL-based Physical Reservoir Computing based on MHPe@MYE smart nanocomposites. The work in this chapter exploits the intrinsic nonlinear and history-dependent PL dynamics of MHPe@MYE smart nanocomposites to process temporal optical information as physical reservoir. The system demonstrates discrimination of 4-bit binary sequences through unique PL kinetic signatures and is further integrated with software-based artificial neural networks (ANN) for downstream recognition tasks, evidencing the full potential of PL in neuromorphic computing upon proper materials design.

Chapter 5: Integrating DC/UC PL and high-endurance ferroelectricity into HfO_2 towards dual-mode ultrathin-film platform. The work present in this chapter features the development of Er-doped HfO_2 (HErO) ultrathin films by PLD. Theoretical simulations first elucidate the dual role of Er dopants in stabilizing the FE *o*-phase and introducing localized 4*f* states that enables both UC and DC PL. The resultant PLD-grown high-quality HErO exhibits robust FE with notable endurance up to 10^{11} polarization switching cycles. In the meantime, PL measurements reveal both the visible UC and NIR DC emissions under 980 nm excitation of HErO at ultrathin level (~11 nm). The findings establish HErO as a dual-mode platform, potentially paving the way for advanced multi-mode devices at the nanoscale.

Chapter 6: Conclusions and future prospects. This section gives an overall view of the major findings in this thesis, whereas future works on extending PL-based neuromorphic functions and coupling FE with PL at ultrathin-film platform are further proposed.

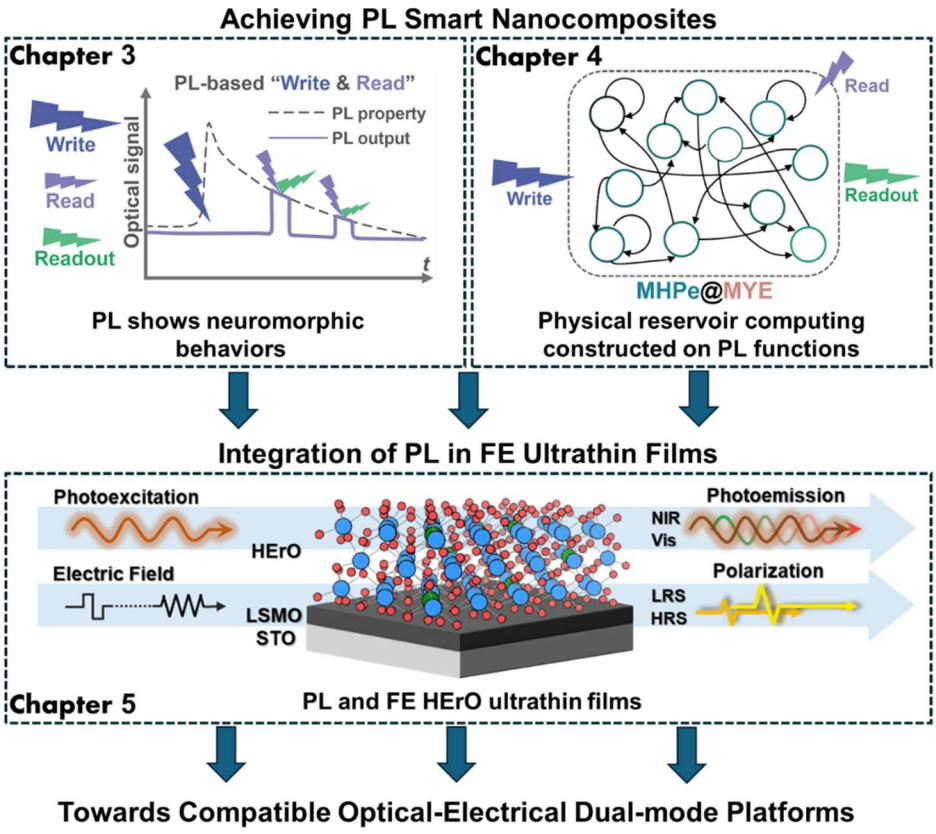

Figure 1.9 Structure of the research presented in this thesis.

Chapter 2 Experimental Techniques

2.1 Construction of smart nanocomposites and FE ultrathin films

2.1.1 Hard-templated Sol-gel synthesis process

The hard-templated sol-gel synthesis of porous oxides is a versatile strategy that combines the use of a pre-formed template, such as silica or poly(methyl methacrylate) (PMMA), with sol-gel chemistry to achieve well-defined nanoscale porous structures.[61] In this approach, the template provides a rigid, ordered framework that dictates the final pore architecture, while the sol-gel process enables the infiltration and subsequent formation of the inorganic oxide network within the template's voids. Typically, the procedure in synthesizing MHPe@MYE smart nanocomposites involves preparing a colloidal crystal of close-packed PMMA spheres, followed by infiltration of the interstitial spaces with the sol precursor of target metal oxides. Upon gelation and thermal treatment, the inorganic precursor solidifies and the PMMA template can be removed by calcination, resulting in a porous oxide that is a negative replica of the original template. This method allows precise control over pore size and connectivity, as determined by the template, and circumvents the challenges of direct assembly in sol-gel systems, such as phase separation or collapse of the mesostructured.

2.1.2 The PLD process

PLD is a versatile thin-film growth technique that harnesses pulsed lasers to ablate target material from a solid target and deposit it onto a substrate. The photo of the PLD chamber used in this study is shown in **Figure 2.1**. When a laser pulse, such as the KrF excimer beam at 248 nm with a pulse duration of ~20 ns, is focused at energy density of ~1.0-2.0 J/cm^2 onto the target surface under an ultra-high vacuum or controlled atmosphere chamber, the intense and localized energy can be absorbed within the optical penetration depth (tens of nanometers), resulting in a rapid heating above the target's vaporization threshold. This impulsive heating generates a transient and high-temperature plasma plume containing atoms, ions, clusters, and particulates. The plume would expand perpendicular to the target surface under a combination of thermal effects and Coulombic forces, which is also strongly influenced by the atmosphere, substrate temperature, the distance target between substrate, and laser repetition rate. Such multiple parameters can be finely tuned during experiments to optimize the kinetic energy of ablated species before arrival on the substrate. On critical merits of PLD is that it can enable near-stoichiometric transfer of multi-element targets, making it ideally suited for complex oxides, such as $La_{0.7}Sr_{0.3}MnO_3$ (LSMO). In this work. In this thesis, the FE ultrathin films of HErO (3-30 nm), together with the buffer LSMO layer (20-50 nm), were grown on $SrTiO_3$ (STO) (001) substrates (5×5 mm) by PLD.

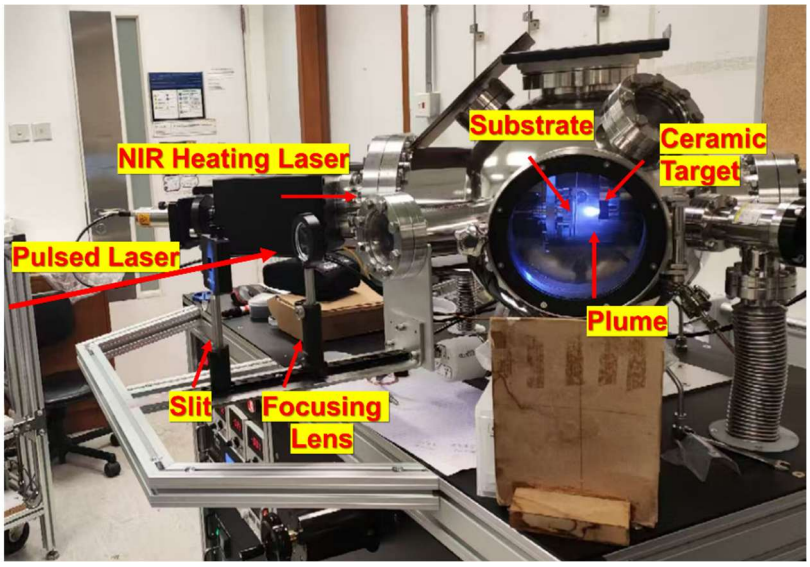

Figure 2.1 Photo of the PLD system used in this research.

2.2 Material characterizations

2.2.1 Powder X-ray diffraction analyses and Rietveld refinement

X-ray diffraction (XRD) analysis is widely used for non-destructive characterization for determining the structure and crystalline information of samples. The schematic illustration of the XRD working principle is shown in **Figure 2.2**. The waves scattered by the lattice planes can be effectively collected provided that the incident angle (θ) satisfies the Bragg's-law criterion:

$$2d_{hkl} \sin\theta = n\lambda$$

where d_{hkl} is the lattice plane spacing and λ is the wavelength of X-ray source (here, Cu K_α, λ = 1.5406 Å). During scanning, the specimen stage and detector are kept in the θ-2θ configuration, and diffraction peaks corresponding to different crystallographic planes are recorded over a continuous scanning angular range. Specifically for the smart nanocomposite samples of this research in powder form, a

Rigaku SmartLab 9kW was used with the Bragg-Brentano (BB) focusing optic alignments. The utilized BB mode can maximize intensity by concentrating diffracted X-rays from large sample areas while maintaining adequate angular resolution, which are highly suitable for polycrystalline and bulk samples.

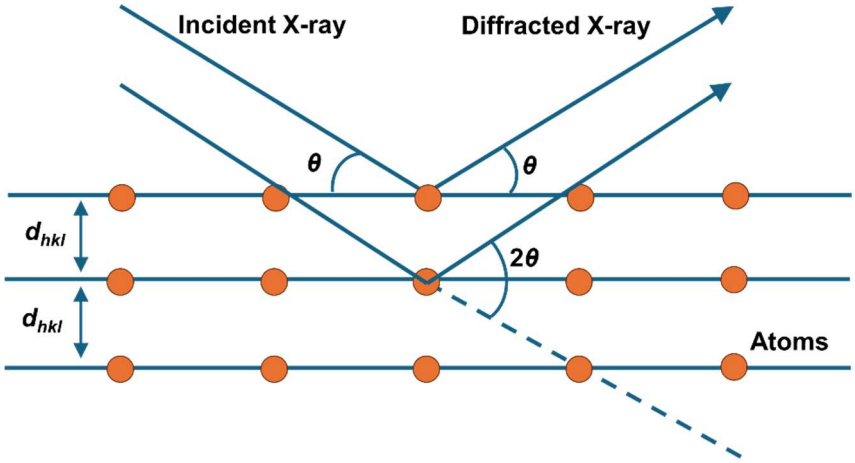

Figure 2.2 Schematic of operating principle of XRD.

After data collection, the Rietveld refinement method is applied to extract the quantitative crystallographic and microstructural parameters, such as crystalline parameters, strains, dopant occupations, phase ratio, thermal displacement factors, *etc.* Rietveld refinement is performed in a full-pattern fitting approach, where the algorithm iteratively fits these parameters to minimize the overall difference between measured and simulated intensities curve across the full 2θ range. The quality of a refinement can be assessed by statistical indicators, such as the weighted profile R-factor (Rwp) defined as:

$$R\text{wp} = \sqrt{\frac{\sum_{\text{i}} w_i \left(Y_{\text{obs},i} - Y_{\text{calc},i}\right)^2}{\sum_i w_i {Y_{\text{obs},i}}^2}}$$

where w_i is the weight of step i; $Y_{\text{obs},i}$ and $Y_{\text{calc},i}$ indicate the observed and calculated fractional discrepancy at step i, respectively. 10% is a commonly accepted

criteria for acceptable Rwp, with lower value indicates even better agreement of the fitting. Furthermore, goodness-of-fit (GoF) can be qualified by:

$$\text{GoF}\ (\chi^2) = (\frac{R\text{wp}}{R\text{exp}})^2$$

with $R\text{exp}$ representing the statistically expected R-factor. An acceptable χ^2 should be below 3.00, with the ideal value of being 1.00. The above two parameters can give a rapid and quantitative check on the reliability of the refined results.

2.2.2 High-resolution thin-film XRD analysis

For epitaxial multilayer thin films, high-resolution XRD is commonly required for detailed structural analyses to achieve both high angular resolution and strong suppression of unwanted spectral components. In these cases, Ge(220) single-crystal monochromator is usually required. The Ge{220} lattice planes satisfy Bragg's law for the Cu $K_{\alpha 1}$ radiation. Therefore, as the X-ray beam undergoes two- or four-bounce Bragg reflections within the monochromator (**Figure 2.3a**), the unwanted $K_{\alpha 2}$, K_{β}, and background noise can be effectively filtered out. The sharp difference before and after monochromator treatment has been demonstrated in **Figure 2.3b** and **Figure 2.3c**.[62]

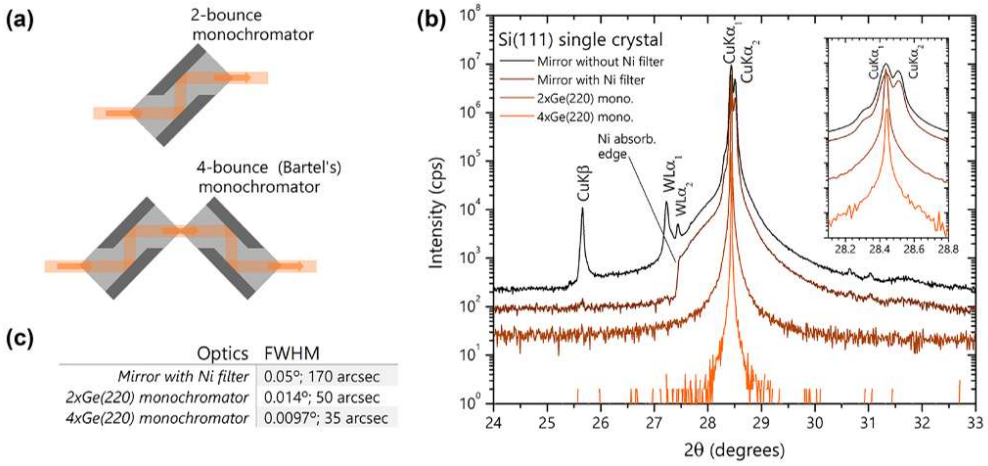

Figure 2.3 (a) Optics setup of Ge(220) monochromator for high-resolution thin-film XRD. (b) Comparison of XRD signals using normal PB, Ni-filtered PB, 2-bounce Ge(220), and 4-bounce Ge(220) monochromator, respectively. (c) full-width at half-maximum (fwhm) parameters of XRD peak using different optics[62].

The fundamental measurement for epitaxial thin-film crystallography is the unsymmetric 2θ-ω scan. The direction of ω, χ, and φ in the sample measurement plane is illustrated in **Figure 2.4**. Compared to the default θ-2θ configuration, in this mode, the incident angle ω was calibrated to ensure that the bisector of incident and diffracted beams can always remain normal to the sample surface. This configuration ensures that only crystallographic planes parallel to the film plane contribute to the diffraction signal, ensuring the best representation of the crystallography information of the thin film. Also, because all the thin-film layers in this work are a few tens of nanometers thick, film diffraction peaks, together with all related crystallographic information, can be orders of magnitude weaker than substrate peaks. Accordingly, the pattern is frequently plotted onto a logarithmic intensity scale for the better visualization of the XRD results.

ω rocking curve measurements are then employed to quantify the angular spread of the given crystallographic plane in order to determine the domain mosaicity and dislocation density. Here, the detector is fixed at a specific Bragg angle 2θ corresponding to the chosen *hkl* reflection of interests, while the incident beam is relatively rocked through small variations around the ideal orientation ($\omega = 2\theta/2$), giving the rocking curve of a specific crystalline plane. The fwhm of this rocking curve directly reflects the distribution of local tilt angles among adjacent coherent domains, which are key judgements of the epitaxial quality. While the fwhm of polycrystalline and textured films often exceed 1°, a high-quality epitaxial film can exhibit small value below 0.1°.

In addition, X-ray reflectivity (XRR) is a complementary low-angle technique that exploits the total external reflection and thin-film interference of X-ray to extract film thickness, interface roughness, and mass-density contrast. At incident glancing angles below the critical angle (θ_c), the X-ray beam can be mostly reflected by the thin-film sample, producing a high-intensity plateau. As the incident angle increases above θ_c, the transmitted and reflected waves from the surface and interface of the thin film interfere with each other, generating a series of periodic oscillations (Kiessig fringes) in the reflected intensity. The fringe period is inversely proportional to the total film thickness, while the trend of amplitude decay is controlled by the roughness and mass density of the thin film. Therefore, fitting the XRR curve can yield thin-film thickness to sub-nanometer precision, which is a powerful tool for thin-film characterizations. In this research, the fitting of XRR utilizes an open-source software GenX 3.

Lastly, the in-plane epitaxial orientation relationships of the thin films have been probed *via* azimuthal φ scans. After aligning the samples at a chosen set of lattice planes

at fixed ω, 2θ, and χ corresponding to the interplanar angle between the film normal and the chosen planes, the in-plane φ angle was rotated through 0°-360°. The number of distinct peaks and their angular spacing directly reveal the in-plane symmetry and the number of rotational domains of the epitaxial thin films. Additional peaks imply multiple domains or rotational variants, and a continuous intensity ring indicates random in-plane orientation.

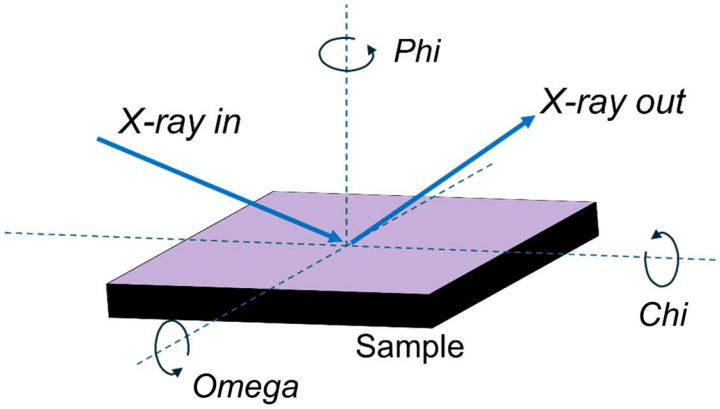

Figure 2.4 Configurations of thin-film XRD measurements.

2.2.3 PL spectroscopy

The PL spectroscopy serves as an effective non-invasive optical method for analyzing the PL properties of the luminescent materials. It is also widely used to probe the electronic structure, defect states, and band gap characteristics of semiconducting materials. The PL phenomenon refers to a specific luminescence process, where the matter absorbs photons to reach excited electronic states, and then falls back to the ground states by emitting photons. The photon energy of PL emission is related to the various energy-level differences between each two electronic states, which is generally lower than the photon intakes. The redshifts between absorption photon to emitted

photon is known as Stokes shifts, while those emitting higher photon energy is accordingly categorized as anti-Stokes shift emissions. Categorized by the PL delay lifetimes, which can be influenced by the trapped states, Laporte and spin selection rules, and electron-phonon coupling effects,[7] PL is further divided into fluorescence (short lifetimes within μs) and phosphorescence (> ms-level). The PL process related in this thesis is all fluorescence. In a typical PL experiment, incident photons from excitation light sources reach and become absorbed by the sample materials, pumping electrons from the valence band or ground state into higher energy levels. These electrons then relax back to lower energy levels via radiative transitions, generating light emission to reach the photodetector or photomultiplier tube (PMT). The analyses of both the steady emission spectrum and the decay kinetics offers detailed insight into trap states, dopant levels and ET pathways within the sample.

In this thesis, the steady state and time-resolved PL measurements reported here were carried out on an Edinburgh Instruments FLS 920 spectroscopy. A photo of the equipment used is shown in **Figure 2.5**. This modular system features two excitation arms, each able to accommodate either a continuous xenon lamp, pulsed diode laser, or LED light sources and a common emission arm that delivers the signal to a high sensitivity PMT detector. The utilized excitation sources of FLS 920 in this thesis were Xeon lamp, laser diodes of 980 nm and 360 nm, and LEDs as the excitation sources.

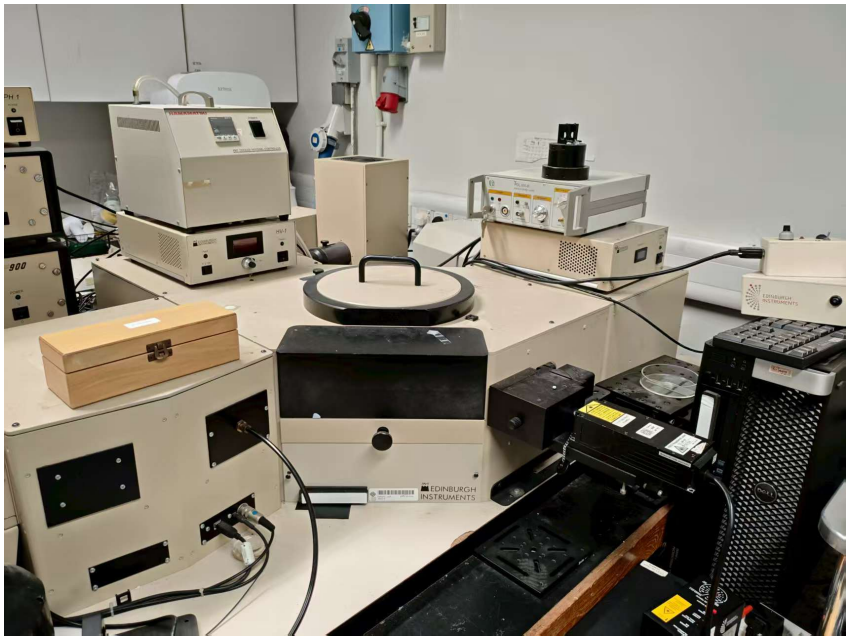

Figure 2.5. Photo of the Edinburgh FLS 920 spectroscopy used in this thesis.

2.2.4 X-ray photoelectron spectroscopy

X-ray photoelectron spectroscopy (XPS) is a surface-sensitive analytical tool that provides quantitative information on the elemental identity, chemical stoichiometry, and electronic/chemical states on the surfacial layers of the sample. The characterization mechanism relies on the photoelectric effect. In XPS analysis, the sample surface is irradiated with X-rays, resulting in the emission of photoelectrons whose kinetic energies are characteristic of their binding energies within the microstructural or crystalline structure of the material. By measuring the kinetic energy of these emitted electrons, it is possible to construct a photoelectron spectrum that reveals distinct peaks corresponding to specific elements, and their corresponding chemical environments can be further studied. In this thesis, a Thermo Scientific Nexsa X-ray photoelectron spectrometer was employed for XPS analyses of the HErO thin

films to probe the doping environments of Er and Hf upon introducing Er dopants to stabilize the FE phase of HfO_2.

2.2.5 Scanning transmission electron microscopy

Scanning transmission electron microscopy (STEM) operates by directing a highly focused and accelerated electron beam onto an ultrathin specimen (**Figure 2.6**). As the incident electrons interact with the atoms in the sample, they are scattered at various angles, a process known as solid-angle scattering. The extent of this scattering is influenced by both the density and thickness of the material, resulting in image contrast that reflects these properties. The scattered electrons are subsequently detected by imaging devices such as phosphor screens or photosensitive detectors, where the signal is magnified and focused to produce high-resolution images. Due to the extremely short de Broglie wavelength of electrons, STEM can achieve spatial resolutions up to an order of 1 angstrom, far surpassing that of conventional optical microscopy, with magnifications reaching several million times. This exceptional resolution enables direct visualization of fine structural details, including individual atomic columns, which are orders of magnitude smaller than the features resolvable by light microscopy. At lower magnifications, image contrast in TEM primarily arises from differences in electron absorption, which are dictated by variations in sample thickness and composition. At higher magnifications, however, complex electron wave interference effects can influence image intensity, necessitating advanced analytical approaches to interpret the resulting data. STEM offers a range of imaging and analytical modes, allowing for comprehensive investigation of materials in terms of their chemical

composition, crystallographic orientation, electronic structure, phase shifts, and conventional absorption characteristics.

In this work, STEM techniques was employed for four principal purposes: (1) high-resolution TEM (HRTEM) imaging for direct insight into the atomic arrangement and lattice structure of nanocomposites; (2) cross-sectional TEM (CSTEM) imaging, used for mapping large-scale epitaxial layers of the HfO_2 thin films; (3) energy-dispersive X-ray spectroscopy (EDX) and elemental mapping, aiming to reveal the elemental composition and distribution of both smart nanocomposites and FE ultrathin multilayers; (4) Integrated differential phase contrast (iDPC)-STEM and high-angle annular dark-field (HAADF)-STEM imaging, to capture both light (oxygen) and heavy (metals like Hf, La, Sr, *etc.*) elements with high contrast and angstrom precision, provides critical insights on the quality, epitaxial orientation, and domain structure of FE ultrathin multilayers. STEM analyses for the Chapter 3 and 4 were conducted by a Tecnai TF30 transmission electron microscope, while the STEM images in Chapter 5 were taken in a Thermo Fisher Spectra 300 using cross-section samples prepared by focused ion-beam-cutting.

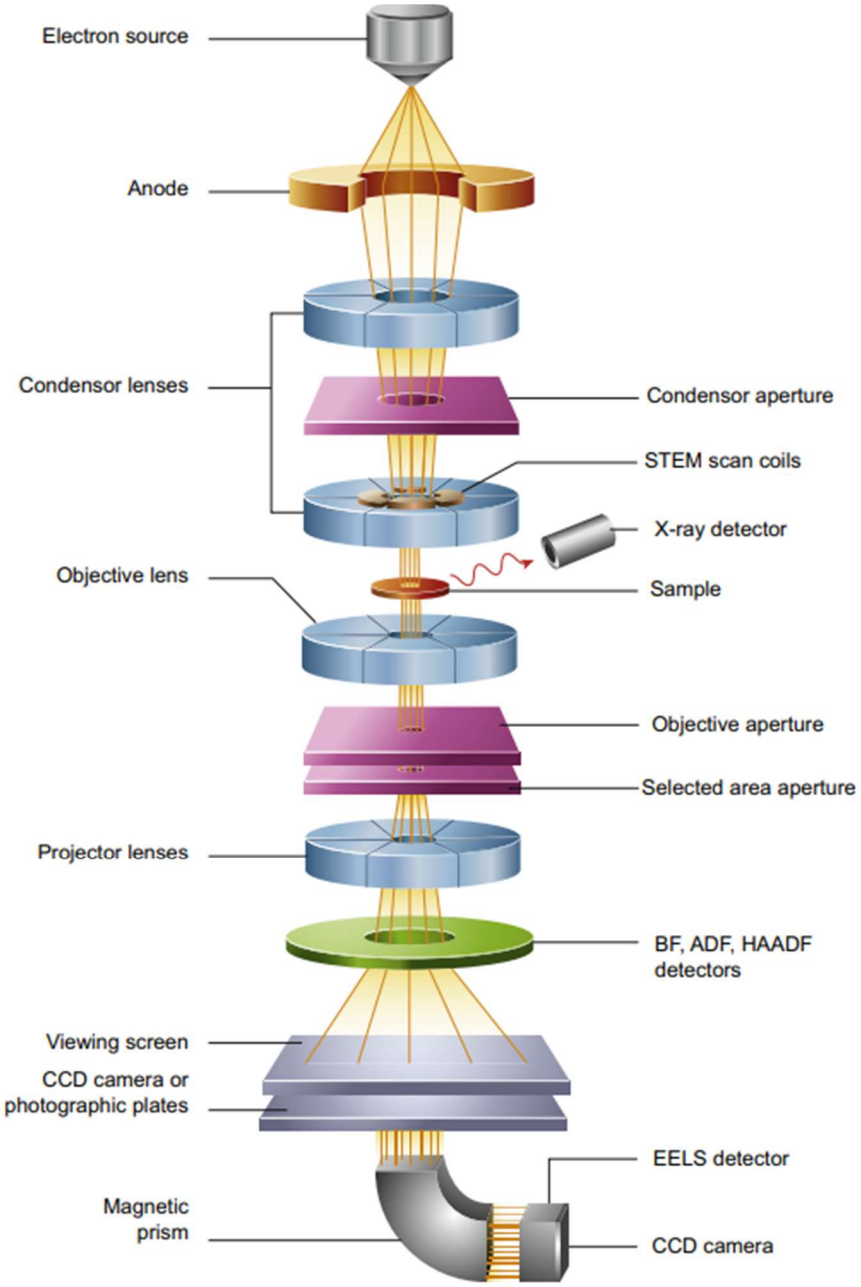

Figure 2.6 Block-diagram of scanning transmission electron microscopy.[63]

2.2.6 Energy dispersive X-ray spectroscopy

Energy-dispersive X-ray spectroscopy (EDS) is a micro-analytical technique that identifies and quantifies the elemental constitution of a specimen by measuring the

energy and intensity of its characteristic X-ray emissions. The method is conventionally coupled with SEM and STEM equipment to obtain spatially resolved chemical information. The physical basis of EDS lies in the interaction between a focused electron beam and the measured sample. The physical scheme is shown in **Figure 2.7.** Upon electron irradiation, core-shell ionization occurs; when higher-shell electrons fill the resulting vacancies, the excess energy is released as X-ray photons rather than being re-absorbed by the atom. These emitted photons possess energies equal to the difference between the involved electronic states, which enables the element-specific recognitions. Consequently, the emitted spectrum constitutes fingerprint signals of the corresponding elements present in the sample, enabling semi-qualitative identification based on the integrated intensity. This is enabled by the fact that each characteristic line scale is monotonically related to the concentration of the detected element.

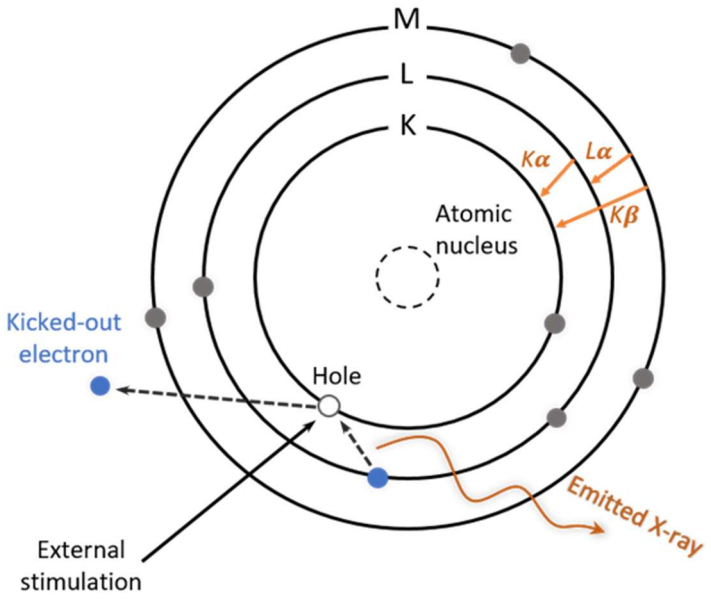

Figure 2.7 Fundamental principle of energy dispersive X-ray spectroscopy.[64]

2.2.7 Scanning probe microscopy

Scanning probe microscopy (SPM) encompasses a family of advanced techniques that enable the investigation of material properties and surface features at the atomic or nanoscale. The fundamental principle of SPM is based on the detection and analysis of various interaction forces between a nanometer-scale probe and the sample surface. Among the diverse SPM techniques, atomic force microscopy (AFM) is the most widely utilized due to its versatility in imaging surface topography, height, roughness, and phase contrast. In AFM, a nanoscale probe attached to a cantilever scans the sample surface, and its deflection as monitored by a laser can reflect surface features (**Figure 2.8**). AFM can operate in contact, tapping, and non-contact modes.[65] Contact mode offers high accuracy but risks damaging the sample, while non-contact mode is non-destructive but less accurate. Tapping mode, used in this study, oscillates the tip near the resonance frequency to capture high-resolution images without harming the sample.

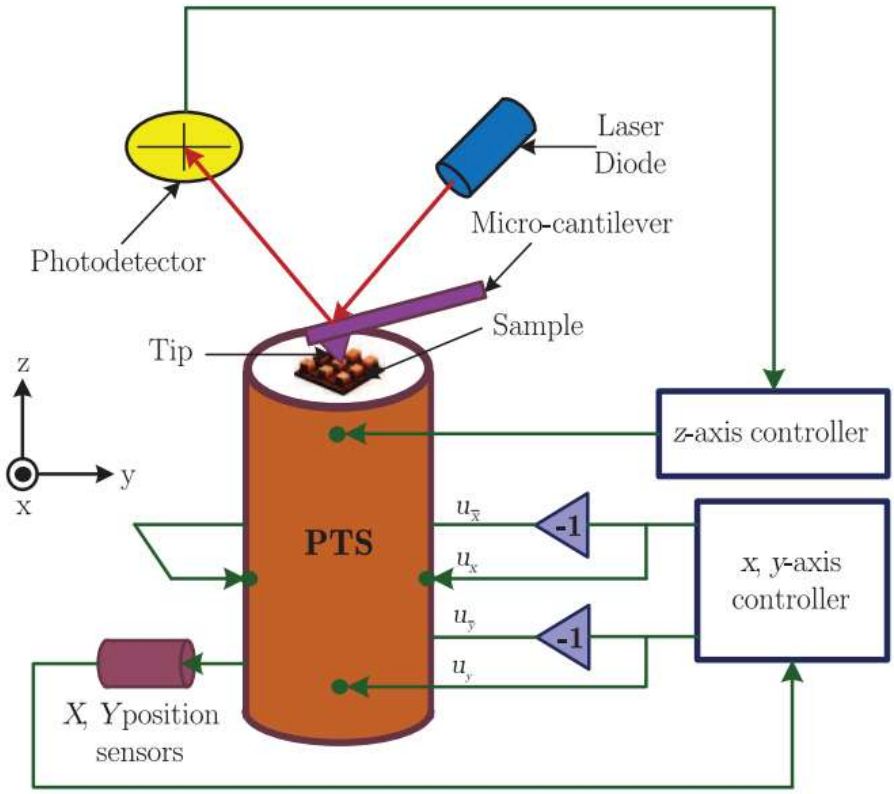

Figure 2.8 Schematic view of the working principle of AFM.[65]

Piezoresponse force microscopy (PFM) is a direct method to investigating FE domains in the ultrathin FE materials. A conductive tip is brought into contact with the sample, and an AC voltage is applied, inducing a periodic strain in piezoelectric materials via the inverse piezoelectric effect, which in turn causes periodic deflection of the cantilever. Because the piezo-induced displacements are extremely small (in the order of pm/V), measurements are typically performed near the contact resonance frequency of the tip to amplify the response. The phase and amplitude of the resulting signal, measured using lock-in amplifiers, can provide direct information about the orientation and distribution of FE domains.

In this work, PFM measurements were conducted using an Asylum MFP-3D Infinity SPM in dual AC resonance-tracking (DART) mode. By tracking frequencies on both sides of the contact resonance peak, the driving frequency is maintained near resonance, amplifying response signals. Lock-in amplifiers simultaneously measure amplitudes and phase, enabling imaging of topography, piezoelectric responses, and FE domains of HfO_2 thin films.

2.2.8 FE tester

Compared to conventional *P-E* hysteresis measurements, the positive-up-negative-down (PUND) test offers significant advantages in accurately characterizing the intrinsic FE switching behavior of materials. In standard *P-E* measurements, the extracted polarization values can be affected by non-FE contributions such as the leakage currents, charge injections, and capacitive effects, especially in thin films and materials with relatively high conductivity. These parasitic effects can distort the hysteresis loop and lead to an overestimation of the true FE polarization. A typical PUND measurement employs a sequence of five voltage pulses, as shown in **Figure 2.9**. The first pulse (pulse 1) sets the polarization of the sample to a defined state. The second pulse, applied in the opposite direction, maintains the maximum voltage for one pulse width to ensure complete polarization switching, at which point the polarization value P_1 is recorded. Further after a waiting period as long as one pulse width, second polarization value P_2 is then measured. Following a certain pulse delay, the third pulse is consequently applied and the polarization value P_3 is recorded. Another waiting period allows for the measurement of another polarization value P_4. The difference (ΔP) between P_1 and P_3 ($\Delta P = P_1 - P_3$) isolates the true remanent polarization from other

factors, as P_1 contains both switching and non-switching components, while P_3 reflects only non-switching contribution. Typically, the ΔP_r between P_2 and P_4 can be also used to represent the remanent polarization after accounting for relaxation effects, and ΔP_r should be equal to ΔP. Pulses 4 and 5 mirror the procedure of pulses 2 and 3 but are applied in the opposite direction to obtain the $-\Delta P$ and $-\Delta P_r$ values. Through this pulse sequence, the PUND test effectively separates the genuine FE response from non-FE artifacts, enabling a more reliable and precise assessment of the "net" FE properties.

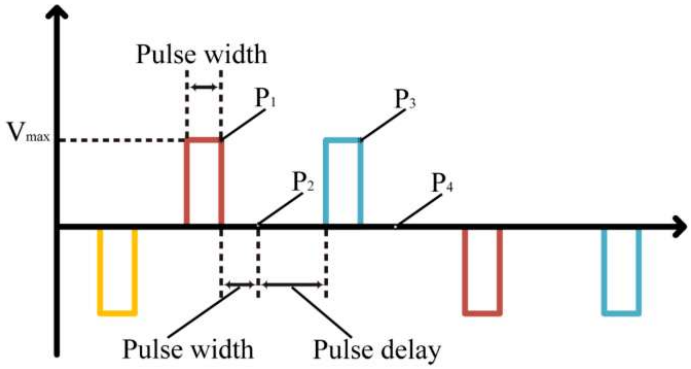

Figure 2.9 Schematic of the pulse sequence for the PUND test.

In addition, endurance test was performed by subjecting FE HErO thin films to repeated bipolar polarization switching cycles using triangular voltage waveforms. The voltage was biased at the LSMO bottom electrode while the top Au/Ti (deposited by E-beam deposition) was grounded. The cycling was performed at frequencies spanning 100 kHz to 10 MHz with the total accounts from 10^8 to 10^{11}. At each order of magnitude, three PUND measurements at a test frequency of 1 kHz were carried out so to obtain the P_r. By tracking P_r as a function of switching cycles and simultaneously monitoring the shifts in the E_c, the onset and progression of FE fatigue can be systematically characterized.

2.2.9 Synchrotron X-ray absorption Spectrometer

Synchrotron radiation constitutes electromagnetic radiation emitted by high-speed electrons undergoing radially accelerated motion within magnetic fields. Its spectrum spans from IR to hard X-ray, offering brightness several orders of magnitude greater than conventional X-ray sources. This radiation possesses unique advantages including a broad spectrum, high collimation, tunable polarization, and a pulsed time structure, establishing it as a pivotal experimental tool for fields such as condensed matter physics and materials science In materials characterization, synchrotron radiation proves particularly effective for probing atomic-scale local structure and electronic state information, enabling detailed analysis of chemical valence states, spin states, coordination environments, electronic band structures, and magnetic ordering behavior. Furthermore, its inherent time-resolved and spatially resolved capabilities facilitate the dynamic capture of structural and electronic state evolution in materials under external stimuli.

In parallel, X-ray absorption spectroscopy (XAS) represents a powerful characterization technique based on synchrotron radiation, primarily employed for investigating the local electronic structure and atomic environment of specific elements in materials. Its fundamental principle involves the strong absorption of incident X-ray photons when their energy approaches or exceeds the binding energy of an inner-shell electron, such as a 1*s* or 2*p* electron, exciting the electron into unoccupied conduction band states or continuum states. Here in this thesis, XAS is utilized to investigate the atomic environment of Hf of FE HfO_2 thin films before and after electrical cycling,

which effectively provide insights on the microstructural variations behind the fatigue phenomenon of FE HfO_2.

2.2.10 Theoretical simulations

In this thesis, DFT simulations were performed to provide key insight into the physical mechanisms of materials' properties, including the progressively changed halogen migration behaviors in MHPe@MYE and the Er-stabilized oxygen motion during electrical cycling of FE HfO_2. All simulation utilize the generalized gradient approximation (GGA) Perdew−Burke−Ernzerhof (PBE) exchange-correlation functional in the Vienna *ab initio* simulation package (VASP) simulation code.[66]

For DFT simulations of MHPe@MYE, the plane-wave cutoff energy was set to be 400 eV for all calculations. A 3 × 3 × 3 **k**-mesh centered at the gamma point was used for investigating the bulk MHPe and Y_2O_3 (Eu^{3+}). For investigating the surface adsorption and interface NEB of MHPe@MYE migration processes, a 3 × 3 × 1 **k**-mesh grid was used. The converge criteria were settled for all calculations as follows: 1) the Hellmann-Feynman forces should not exceed 0.1 eV/Å; 2) the total energy difference should not be over 1×10^{-5} eV. Surface energy (γ) of halogen adsorption is calculated by the following equation:

$$\gamma = \frac{E_{\text{slab}} - NE_{\text{bulk}} - E_{\text{Halogen}}}{2A}$$

Where the E_{slab} is the total energy of the constructed surfacial model and E_{bulk} is the total energy of the original structure of MHPe and Y_2O_3, N denotes the number of supercell, A shows the area of the surfacial model, E_{Halogen} is the reference energy of Br and Cl, which can be derived from Br_2 and Cl_2, respectively. The CDD diagram (ρ_{diff}) of halogen adsorption on the Y_2O_3 surface was plotted using the below equation:

$$\rho_{\text{diff}} = \rho(\text{Y}_2\text{O}_3 - \text{X}) - \rho(\text{Y}_2\text{O}_3) - \rho(\text{X})$$

where $\rho(\text{Y}_2\text{O}_3 - \text{X})$, $\rho(\text{Y}_2\text{O}_3)$, and $\rho(\text{X})$ represent charge density of the X-absorbed Y_2O_3, pristine Y_2O_3 surface, and the sole X structure in vacuum, respectively. NEB has been employed for investigating the energy barrier during the halogen migration path starting from surface absorption, the surface MHPe layers, the subsurface layers, and eventually deep into the fixed lattice MHPe layers.

For simulation in HErO, A similar 3×3×3 Monkhorst-pack *k*-point mesh was employed to sample the Brillouin zone, and the criteria for geometry optimization ensure the energy on the atoms was less than 1.0×10^{-5} eV and all the forces on atoms were below 0.01 eV·Å^{-1}. The NEB method was used to model the FE and non-FE oxygen migration. The Berry phase method was applied to calculate the FE polarization based on optimized pristine *Pca2₁* HfO_2 structures and the centrosymmetric *Pbcn* structure for the interpolation. During calculation of the electronic structure of HErO, since the traditional GGA-PBE functional is inadequate for partially filled *f*-electron systems with strong interactions,[67] the GGA+U method was employed on the case of HErO, where the applied Hubbard U parameter to Er *f* orbitals is 6 eV after tests.

The whole DFT computations in this thesis has been performed with assists from the VESTA software,[68] vaspkit codes,[69] and VTST scripts.[70,71]

2.2.11 Software-based offline ANN training

Python code employing *TensorFlow*/*Keras* package performed offline ANN training to assess the MHPe@MYE physical reservoir's performance on MNIST. The empirical PL mapping features serve as the direct inputs to the *python* ANN software

for further training and acquiring the recognition accuracies of the different device configurations. The ANN was trained in the *PyCharm* IDE platform using *Adam* optimizer using the sparse categorical cross-entropy for the loss function (L), which can be given by:

$$L = -\sum_{i=1}^{N} y_i \log(\hat{y}_i)$$

where N is the number of classes, y_i is the true label, and $\hat{y}_i$ is the predicted probability for class i. The optimizer updates the weights (w) at each step (t) according to:

$$w_{t+1} = w_t - \frac{\eta}{\sqrt{\hat{v}_t}+\epsilon}\hat{m}_t$$

where the $\hat{m}_t$ and $\hat{v}_t$ terms indicate both the bias-corrected first and second moment estimates of the gradients. In the meantime, the initial learning rate is given by η.

.

Chapter 3 PL-based Neuromorphic Behaviors in MHPe@MYE Smart Nanocomposites

3.1 Introduction

The explosive growth of the Internet of Things has generated unprecedented volumes of data across diverse media, driving an urgent demand for information processing technologies beyond conventional electrical approaches.[72-75] Such demands are driving the rapid development of multi-functional materials and devices, especially the ones using bioinspired algorithms for the enhanced efficiencies and adaptabilities.[76] As the most ubiquitous form of information, optical signal processing offers unique advantages over traditional electrical systems, including the ultrafast operation speeds, parallel processing capabilities, and minimal signal crosstalk.[77-79] Consequently, the emergent multimodal platform majorly exploits the coupling between electrical and optical inputs and outputs, leading to four major categories: both electrical input/output, optical-input electrical-output, electrical-input optical-output, and both optical-input/output. Among all the emergent modes, the optoelectronic ones that transform input light signals into electrical signals by the photoelectrical or photovoltaic effects have accomplished significant practical implementations.[80-84] Recently, the electric-field-modulated optical and PL response have also exhibited promising potential in constructing electro-optical logic applications.[57-59,85,86] However, all-optical devices relying exclusively on light stimulus with PL output remain significantly underexplored.

Multi-modal phosphors have emerged as essential components for applications spanning information security, detection, and optical data storage technologies.[87-95] Conventional approaches in these fields have primarily exploited static PL diversity or the capacity for reversible PL emission changes when subjected to external triggers, establishing the foundation of "*smart phosphor*".[11] However, to cope with the exploding information in multiple dimensions, these materials should go beyond the boundaries of simple stimuli-responsive functions, aiming at more complex capability in active optical information processing. This evolution aims to extend the functions of "*smart phosphor*" to comprehensive luminescence-based computing, including transmission, modulation, processing, switching, and amplification of information.

Based on these insights, this thesis develops a smart nanocomposite phosphor system consisting of mixed-halide perovskite embedded in macroporous Y_2O_3:Eu (MHPe@MYE). The nanocomposite exhibits distinctive neural-like characteristics during the light-induced PL modulation processes. DFT simulation indicates that dynamic halogen ion migration at the MHPe@MYE's interfaces serves as the primary mechanism that driving the adaptive PL emission responses upon exposure to optical excitation. This platform successfully realizes complete PL-based "Write" and "Read" operations through programmed light spike excitations, while spectral characterization demonstrates sophisticated neuromorphic properties that intriguingly replicate the functional characteristics observed in biological synaptic networks. Leveraging these features, an all-optical neuromorphic computing platform was constructed using MHPe@MYE as physical reservoir, successfully achieving 4-bit binary sequence discrimination thoroughly utilizing optical stimuli and PL readout. The system further demonstrated promising potential in biometric security applications, achieving 94.4%

accuracy in detecting manipulated fingerprints from UV images. This research presents an innovative nanocomposite of "*smart phosphors*" materials featuring engineered neural-like characteristics, potentially establishing pathways for comprehensive optical neuromorphic systems that incorporate PL functions for neuromorphic computational applications.

3.2 Construction of MHPe@MYE

The preparation of MHPe@MYE porous nanocomposites involves the synthesis of poly-methyl methacrylate (PMMA) mesosphere templates (~80 nm in diameter), hard-templated sol-gel synthesis of MYE host, and incorporation of MHPe into MYE by thermal evaporation of the precursor. The procedure was modified based on previous reports as illustrated in the flowchart in **Figure 3.1**.[96] First, 5 mL of MMA monomer was mixed with 50 mL of deionized water in a three-neck flask, followed by the addition of 0.05 g $K_2S_2O_8$. The mixture was maintained at 65 °C for 1 hour with stirring at 350 rpm under inert atmosphere for colloidal polymerization. After cooling to room temperature, the product was washed with deionized water twice and centrifuged at 4000 rpm to discard the precipitates containing large particles, followed by a second centrifugation at 16000 rpm to collect the desired PMMA mesosphere. The MYE material was prepared via a sol-gel process wherein a solution was formed by dissolving 5 mmol each of $Y(NO_3)_3$ and $Eu(NO_3)_3$ in 25 mL of deionized water, followed by the addition of 10 mmol of citric acid. The solution was heated at 80 °C to obtain a uniform sol. Next, a layered assembly of PMMA mesosphere template was first prepared by filtering through the vacuum pump. The MYE sol was then added to fill into the intervals of the above template. The obtained samples were then dried at 60 °C and

calcined at 400 °C at the inert atmospheres, where the PMMA hard templates can be discarded and make MYE in the negative replica of assembled PMMA. The final MYE host phase was formed by a concluding calcination step at 1000 °C. Incorporation of MHPe has been achieved through thermal evaporation within the DMSO precursor containing 0.33 mmol $PbCl_2$, 0.67 mmol $PbCl_2$, and 1 mmol CsCl dissolved in 1 mL DMSO. 0.1 g MYE host was weighed and immersed into the as-prepared DMSO precursor for 1 h, followed by washing twice with DMSO to remove remnant precursors on outside surfaces of MYE. The final MHPe@MYE smart nanocomposites were obtained by heating the DMSO-contained MYE under 150 °C for 15 min.

The as-constructed MHPe@MYE composites demonstrate intriguing PL variations under light illumination. As demonstrated in the inset photo of **Figure 3.1**, upon UV light excitation, it first shows moderate red PL emission from Eu^{3+}. As irradiation continues, intense green light emission gradually emerges and becomes dominant. After switching off the UV light, PL signal ceases immediately with no afterglow decay. In the meantime, the PL properties of MHPe@MYE gradually recover with no obvious changes under natural light. Within approximately 3 min later, the PL properties can be fully recovered, which can be prompted to PL variations again.

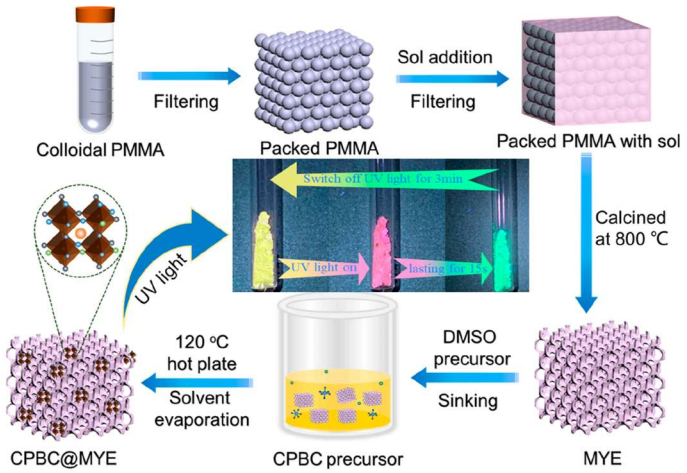

Figure 3.1 Flowchart for the hard-template sol-gel and solvent evaporation synthesis of MHPe@MYE "*smart phosphor*" with light-induced PL variations.[97]

The morphological characteristics of MHPe@MYE porous nanocomposites were systematically examined through various electron microscopy techniques. First, the PMMA hard template exhibits uniformly spherical shapes of approximately 150 nm in diameter (**Figure 3.2a).** Following removal and calcination of PMMA with regular and monodisperse distribution, the porous structure of MHPe@MYE is also well-defined and evenly distributed with ~80 nm, as shown in **Figure 3.2b**. The relatively shrunk porous size compared to the original template is a common phenomenon. The construction of nanoscale porous structure in MHPe@MYE can also be evidenced in TEM images in **Figure 3.2c** and **d.** Further elemental distribution analysis via STEM-EDS mapping demonstrates the presence of MHPe NPs inside the channel of MYE porous matrix, as indicated by the aggregated Cl (green) and Pb (yellow) signals in **Figure 3.2e** within the marked regions (red dot cycles) in original STEM images (**Figure 3.2f)**, where no Y signal has been detected. In the meantime, the Y element (purple) was found predominantly distributed across the MYE host porous matrix. The above microscopic investigation evidences the successful preparation of uniform porous MYE host, and the presence of MHPe NPs embedded in the channel.

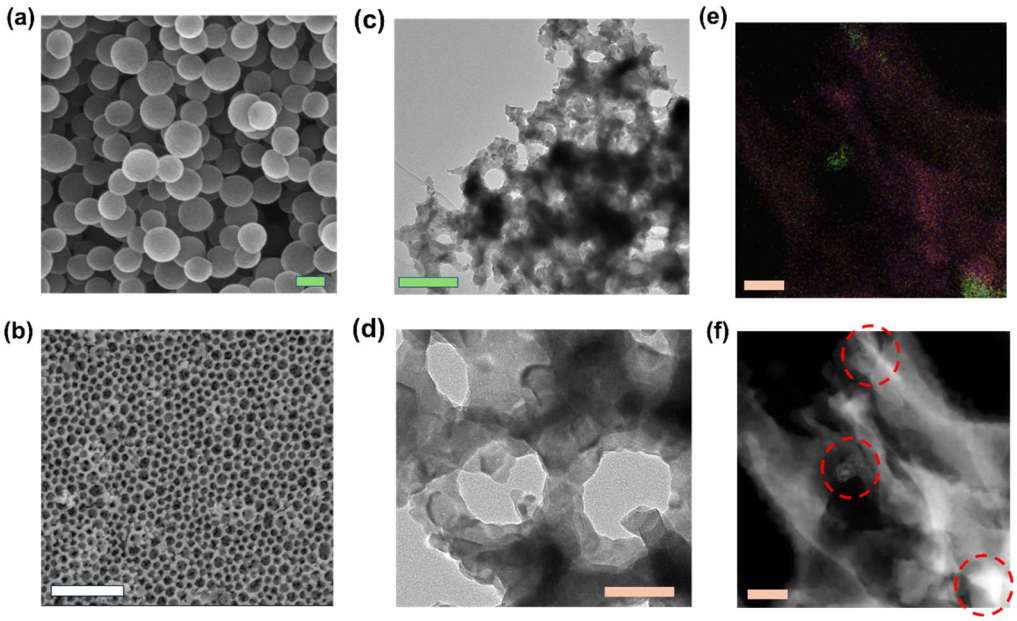

Figure 3.2 (a) SEM image of the prepared PMMA mesosphere. (b) SEM image of the porous MHPe@MYE. (c) TEM image of MHPe@MYE. (d) Enlarged TEM image showing the porous structure of PMMA. (e) TEM EDX mapping, the green, yellow and red color represents Cl, Pb, and Y elements, respectively, and (f) the original STEM images with the presence of MHPe NPs cycled in red. The green, orange, and white scale bar indicates 200 nm, 80 nm, and 1 μm, respectively.[97]

The phase composition of the porous nanocomposites was then investigated by confined XRD refinements (**Figure 3.3**). The 2θ diffraction peaks can be well indexed into the mixture of orthorhombic $CsPbCl_3$ (PDF #18-0036) and cubic Y_2O_3 (PDF # 43-1036) without noticeable presence of impurity phases. The phase ratio of $CsPbCl_3$: Y_2O_3 is estimated as 5%: 95%, indicating a majority of MYE hosts in the MHPe@MYE smart nanocomposites.

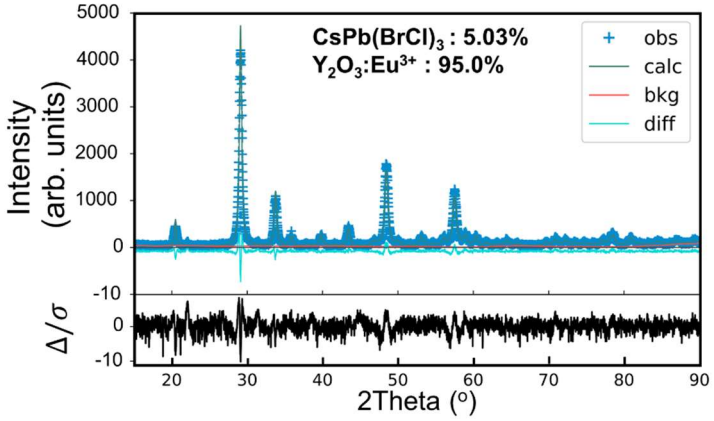

Figure 3.3 XRD refinements showing the phase ratio of MHPe and MYE.

3.3 PL kinetics characterizations

Detailed investigation on the dynamic light-induced PL variation process of MHPe@MYE was then carried out.[98] The time-resolved PL mapping of MHPe@MYE under continuous 360 nm excitation is given in **Figure 3.4**. It consists of two part of PL signals: one is the red PL peaks at ~613 nm from Eu^{3+} in MYE host (marked by red dot lines), which is constant throughout the measurements; another is the PL signals at ~ 500 nm from MHPe (cycled by blue dot lines), which gradually enhances and slightly red-shifted over time, as well as several steady Eu^{3+} peak at around 613 nm.

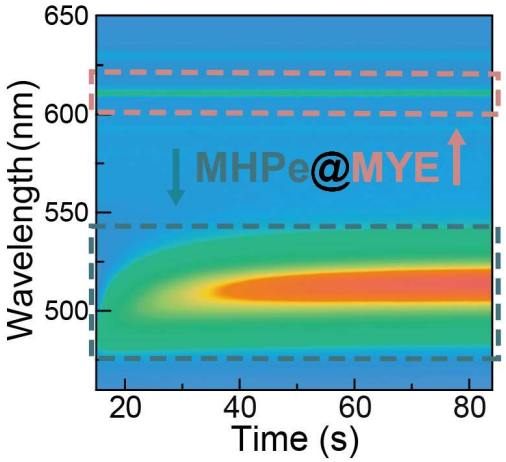

Figure 3.4 Time-resolved PL mapping of MHPe@MYE under 365 nm irradiation.

After switching off the excitation source, a spontaneous dark recovery process takes place. Notably, it is confirmed that the PL property variations during recovery can be effectively "Read" by using weak UV excitation conditions, which does not interfere the PL variation processes. As shown in **Figure 3.5a**, no PL variation can be observed under weak UV light excitation, where the MHPe PL signal only exhibits inert "On" and "Off" states that are solely dependent on the excitation power. These mild conditions also revealed the initial PL characteristics of MHPe@MYE, featuring a weak peak at 470 nm originating from defect-rich and Cl-rich MHPe (**Figure 3.5b**).

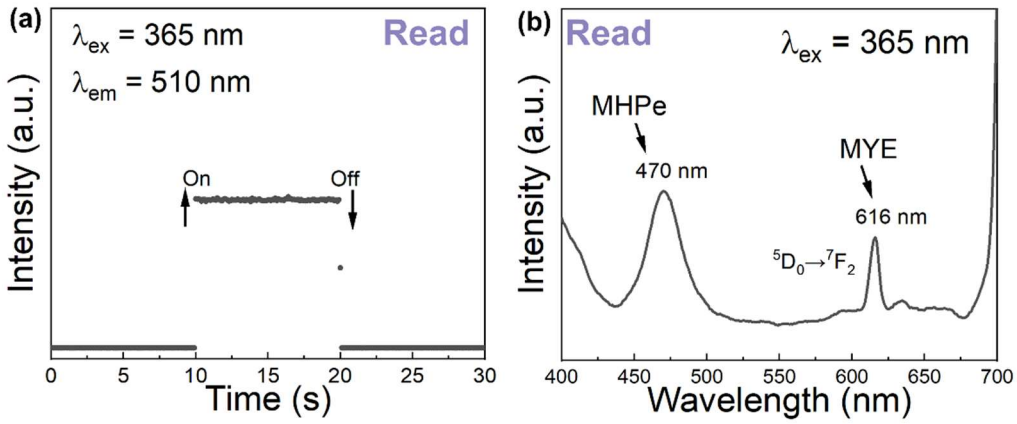

Figure 3.5 PL properties of MHPe@MYE under "Read" excitation. (a) The PL kinetics monitoring 510 nm MHPe PL emission variations under 365 nm "Read" excitation. (b) PL emission spectrum measured under 365 nm "Read" excitation.

Using strong and weak UV excitation as the "Write" and "Read" operation, respectively, an intriguing temporal optical memory can be constructed based on the PL variation process of MHPe@MYE. As demonstrated in **Figure 3.6**, it shows an enhanced PL intensity upon "Write" process and the effective monitoring of the PL states during recovery process through "Read" signals. The multiple alternating rounds of "Write" and "Read" further reveal the intriguing temporal dynamics. After the initial

"Write" phase, switching to "Read" mode showed partial recovery of PL properties, with subsequent cycles demonstrating progressively slower recovery rates. Similar behavior was observed when slightly elevating the upper cutoff (red dot lines), clearly indicating the incipient synaptic-like characteristics in MHPe@MYE's PL property variations. Additionally, during alternating "Write" and "Read" operations, the transition points, specifically represented by the "Read" recovery endpoints and their immediately following "Write" initiation points, maintain high degree of uniformity as denoted by the green lines. Such a consistency can prove the equivalent PL states of these critical turning points in spite of the altered absolute PL intensity of "Write" and "Read" conditions.

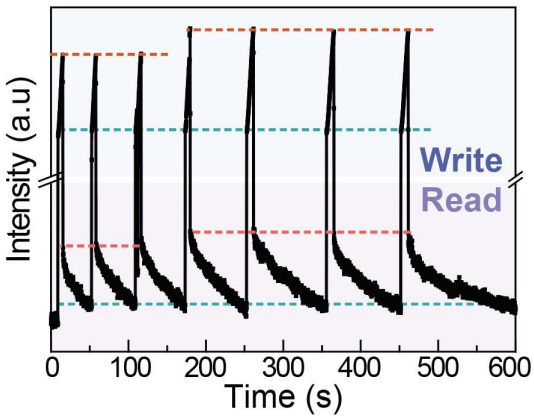

Figure 3.6 Dynamics PL variation under "Write" and "Read" excitation.

3.4 Theoretical insights on dynamic PL variations

The observed PL variation phenomenon in MHPe@MYE smart nanocomposites can be attributed to light-induced halogen migration, which converts defective Cl-rich regions into Br-rich MHPe. Notably, the construction of interfaces within the MHPe@MYE is crucial for realizing neuromorphic PL behaviors of MHPe. Although

it is common for hybrid organic inorganic and mixed I/Br perovskite to exhibit halogen migration using intense light stimuli, all-inorganic Cl/Br perovskites shows better structural robustness and hence is rarely reported to show such halogen migration behaviors.[99,100] Bare MHPe of same mixed-halide composition $CsPb(Br/Cl)_3$ (CPBC) in alternative forms were prepared as comparison studies of the light-induced variations. In specific, Bare MHPe NPs were prepared by conventional hot-injection methods.[101] 1 mmol $PbBr_2$ and $PbCl_2$ were dissolved in a 50 mL 3-neck flask containing 20 mL octadecene as solvent, 1.5 mL oleylamine and 1.5 mL oleic acid as capping ligands, as well as 1 mL n-trioctylphosphine to help dissolve $PbCl_2$. The solution was degassed for half an hour at 120 ºC under vacuum before heating to 150 °C under vigorous stirring and N_2 flow. Afterwards, 0.5 mL preheated cesium oleate precursor was swiftly injected into the mixture, followed by immediate cooling with an ice bath. The precipitates were collected and washed with ethyl acetate and hexane (volume ratio of 1:3) twice to discard the supernatants and finally dispersed in toluene to form a clear colloidal solution of free-standing MHPe NPs. TEM images of the obtained MHPe NPs evidence uniform and monodisperse morphology of ~10 nm in dimensions (**Figure 3.7a**). The inset photo also demonstrates the strong cyan emission of MHPe NPs colloidal solution under 365 illuminations peak at ~485 nm (**Figure 3.7b**). However, no PL variation can be observed, as the time-resolved PL mapping in **Figure 3.7c** features a constant PL property under continuous excitations. Similar results were obtained in bare MHPe films prepared by conventional spin-coating methods. In specific, 0.67 mmol $PbBr_2$, 0.33 mmol $PbCl_2$, and 1mmol CsCl were dissolved into 5 mL mixture solutions of DMF and DMSO (1:2). Prior to film deposition, SiO_2/Si substrates were subjected to standard cleaning procedure with acetone, isopropanol, deionized water, and N_2 purging, followed by O_2 plasma treatment for 15 min. The MHPe precursor solution was spin-

coated onto the pretreated SiO_2/Si substrates at 400 rpm for 10 s and 3500 rpm for 40 s for the spread and thinning phase, respectively. The substrates were then thermally annealed at 110 °C for 10 min in air to crystallize the MHPe polycrystalline films. SEM image in **Figure 3.7d** depicts the rough surfaces of bare MHPe films with polycrystalline features, which also exhibit cyan emission under UV excitation (inset photo). The PL emission spectrum (**Figure 3.7e**) is similar to bare MHPe NPs, while the time-resolved PL mapping features a decreasing intensity at fixed ~480 nm peak (**Figure 3.7f**).These results demonstrate that, without incorporation into porous MYE host matrices, bare MHPe in both NPs and thin-film forms demonstrate only inert PL properties upon UV excitation.

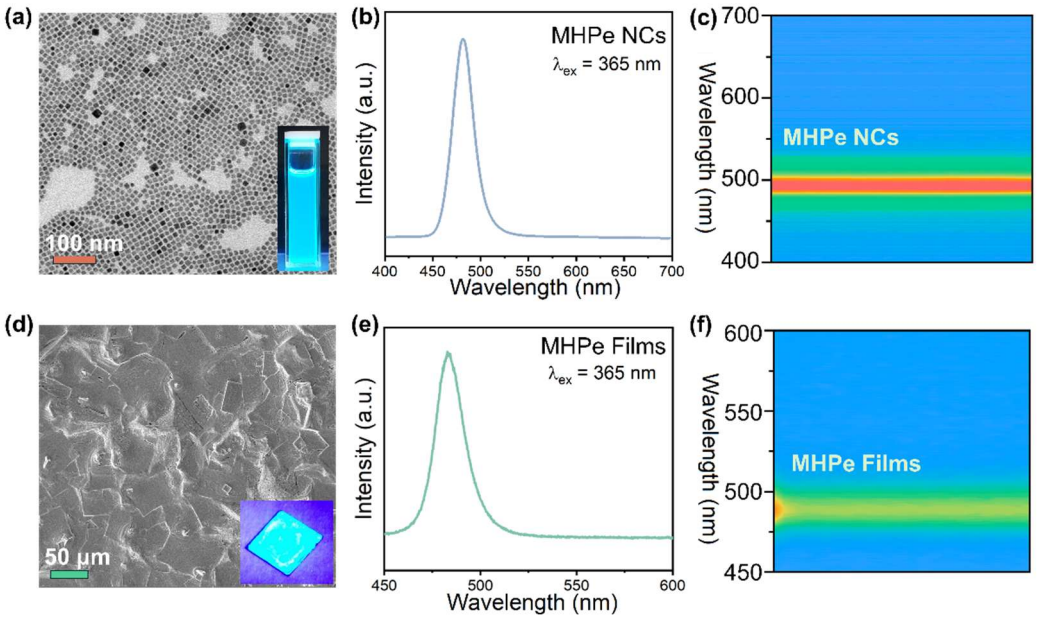

Figure 3.7 (a) TEM images of MHPe NPs prepared by hot-injection method, inset photo shows bare MHPe NPs colloidal solution under 365 nm UV flashlight. Red scale bar indicates 100 nm. (b) The PL spectra of MHPe NPs. (c) The time-dependent PL emission mapping of the MHPe NC upon excitation of 365 nm. (d) The SEM images of spin-coated bare MHPe film, inset photo shows the MHPe film under 365 nm UV

flashlight. The green-colored bar represents 50 μm. (e) The PL spectra of MHPe film. (f) The time-resolved PL mapping of MHPe film under 365 nm excitation.

The above results demonstrate that, without incorporation into porous MYE host matrices, bare MHPe in both NPs and thin-film forms demonstrate only inert PL properties upon UV excitation. On the other hand, the halogen migration process in metal-halide perovskites is known to be highly susceptible to surface effects;[102] Whereas porous materials have demonstrated vast potential in providing interface interactions in luminescent materials.[96,103,104] In this context, the presence of the MYE porous interface plays a crucial role in facilitating halogen migration within all-inorganic Cl/Br systems, which is difficult to achieved otherwisely. This observation motivated a deeper exploration of the underlying mechanism.

Therefore, DFT calculations were then performed in order to elucidate the influence of the MHPe@MYE interface on halogen migration dynamics. The initial focus was placed on examining halogen vacancy defects within MHPe. As shown in **Figure 3.8**, introducing halogen vacancies does not significantly alter the electronic band structures of $CsPbBr_3$ (CPB), CPBC, or $CsPb(Br/Cl)_3$ with halogen vacancies (*v*-CPBC), which highlights the inherent defect tolerance of lead halide perovskites. Additionally, Y_2O_3, with its wide bandgap of 4.2 eV, remains optically inactive in the PL process and primarily serves as a host matrix for Eu^{3+} doping (see **Figure 3.9**).

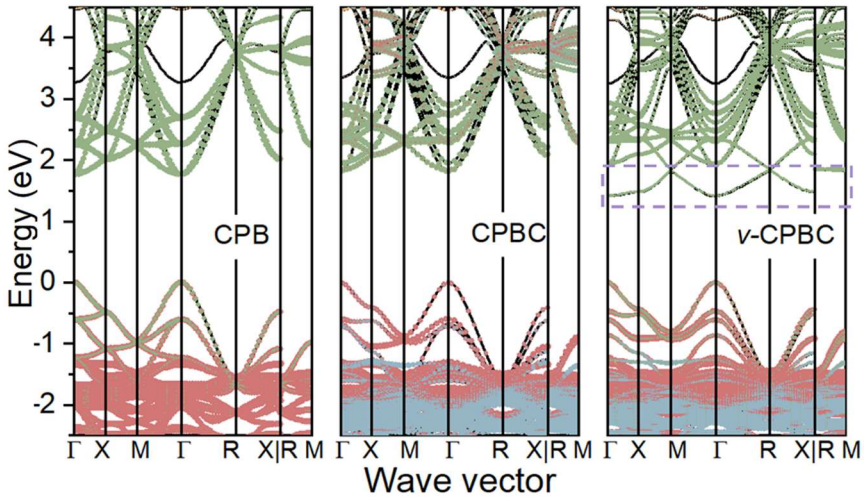

Figure 3.8 Projected electronic band structure of CPB, CPBC and *v*-CPBC.

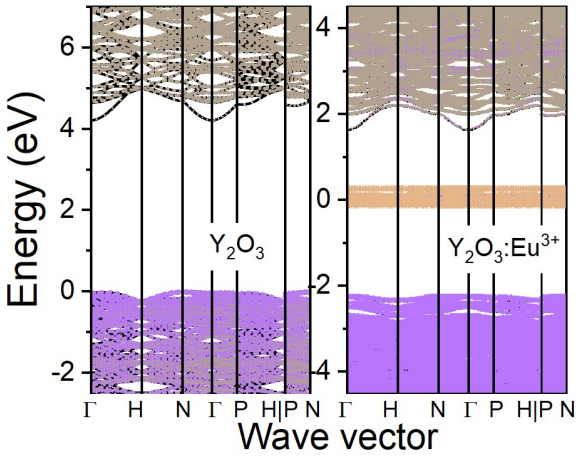

Figure 3.9 Projected electronic band structure of Y_2O_3 and Y_2O_3:Eu^{3+}.

The low formation energy of halogen vacancies accounts for their common presence in halide perovskites. In addition, the strong adsorption of Br and Cl species onto the Y_2O_3 surfaces further induces a defect-rich MHPe in the channel of MYE, as evidenced in previous work. On the other hand, Y_2O_3 may have selectively stronger adsorption to Cl rather than Br. The surface energy of Br/Cl adsorbed on different symmetric sites of Y_2O_3 surfaces was then compared (as marked in **Figure 3.10a**),

which shows that values of Br-adsorbed ones are always larger than the corresponding Cl counterparts (**Figure 3.10b**).

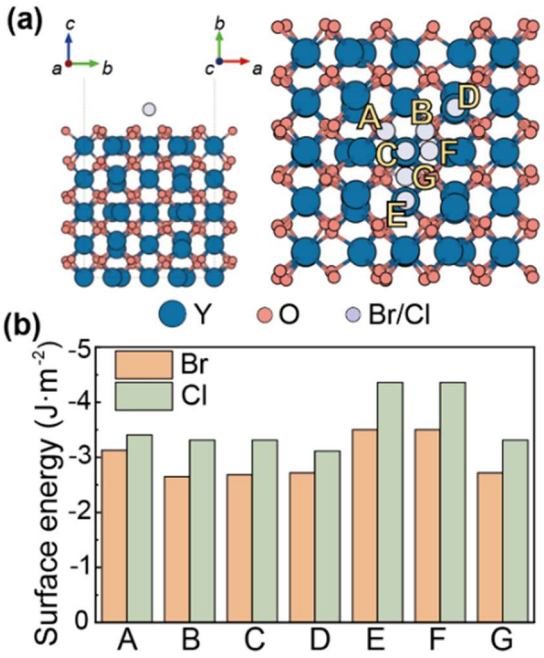

Figure 3.10 (a) The Y_2O_3 surfacial sites of Br/Cl adsorption. (b) Surface energies of Br/Cl adsorbed surfaces.

The charge density difference (CDD) diagrams of halogen-adsorbed Y_2O_3 are also calculated. As shown in **Figure 3.11**, the electron interaction between Y and Cl is stronger than Y and Br, demonstrating a selectively stronger affinition. These can be understood by the difference in electronegativity (χ) and ionic radius (R) between Br (χ = 2.8, R = 1.96) and Cl (χ = 3.0, R = 1.81), where a larger χ and smaller R may form a stronger bound with Y on the Y_2O_3 surface.

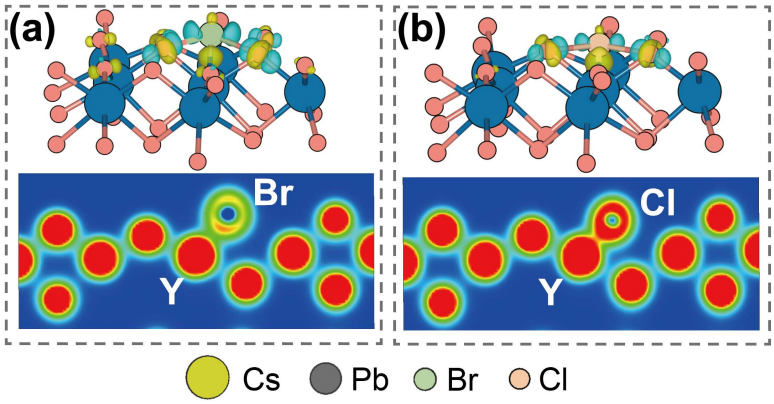

Figure 3.11 3D CDD and charge density diagram of (a) Br and (b) Cl adsorption. The red and blue color mapping area indicates the accumulation and depletion of electrons, respectively.

Combining the surface energy and CDD investigation, the DFT findings collectively indicate a selective halogen-binding mechanism at the MHPe@MYE interface. In specific, a stronger Y-Cl interaction immobilizes Cl^-, while the less stably adsorption of Br^- makes them more readily released upon external stimuli. This differential adsorption alters the local halogen balance and kinetically favoring Br^- incorporation into the perovskite lattice. It leads to increased Br composition, which further reduces the bandgap of MHPe. This mechanistic insight can be directly explained by the observed PL red-shift and enhanced green emission in our experiments.

To further elucidate the kinetic implications of this interfacial halogen migration, the halogen migration process was subsequently investigated, specifically tracking the movement of Br/Cl ions from their adsorption sites on the MYE surface to the surface of MHPe crystal, and ultimately into the bulk of the MHPe lattice. This was achieved using the NEB method. The constructed model, as shown in **Figure 3.12a**, which represents a heterostructure of Y_2O_3 and CPBC. The migration of Br ions into a CPBC lattice with mixed halide content was first examined, where the energy barriers

encountered at each migration step have been calculated. To move from the Y_2O_3 surface to the MHPe surface, Br ions must overcome a relatively low energy barrier of 1.0 eV (**Figure 3.12b**). This step corresponds to the initial phase observed in PL experiments, where Br ions are released from Y_2O_3 and migrate to the defect-rich surface of MHPe under light excitation. Since the presence and subsequent passivation of surface defects are critical for the quantum efficiency of halide perovskites, this migration step is expected to enhance luminescence intensity.[105,106] However, as Br ions penetrate deeper into the CPBC lattice, the energy barriers increase significantly, reaching 3.9 eV for the subsurface and 7.0 eV for the inner layers. As Br migration continues, the halide composition within MHPe changes, which can further influence the migration barriers. To capture this effect, the Br migration from the Y_2O_3 surface into a pure CPB lattice was also examined, which aligns with the later stages of PL evolution characterized by strong green emission from CPB. In this scenario, the interfacial migration barrier for Br drops to 0.71 eV, and the subsequent barriers are reduced to 2.7 eV and 4.5 eV, respectively. This indicates that as the Br content in MHPe increases, Br migration becomes progressively easier, accounting for the observed acceleration in PL property changes. In contrast, Cl migration is associated with higher energy barriers, which is consistent with the predominance of green emission from CPB during the PL evolution. In the meantime, bulk CPB shows a higher Br migration barrier (2.3 eV) (**Figure 3.13**), highlighting the critical role of MHPe@MYE interfaces in enabling adaptive PL changes with neuromorphic behaviors. The backward recovery can be easily achieved by overcoming a relatively small barrier of 0.71 ~ 1 eV. However, the driving force to achieve the dark-recovery could arise from the halogen desorption-adsorption equilibrium at the MHPe@MYE interface, as

well as the diffusion-driven re-homogenization of halogen ions around the interfaces.[99,100,107] Detailed reason should be further explored.

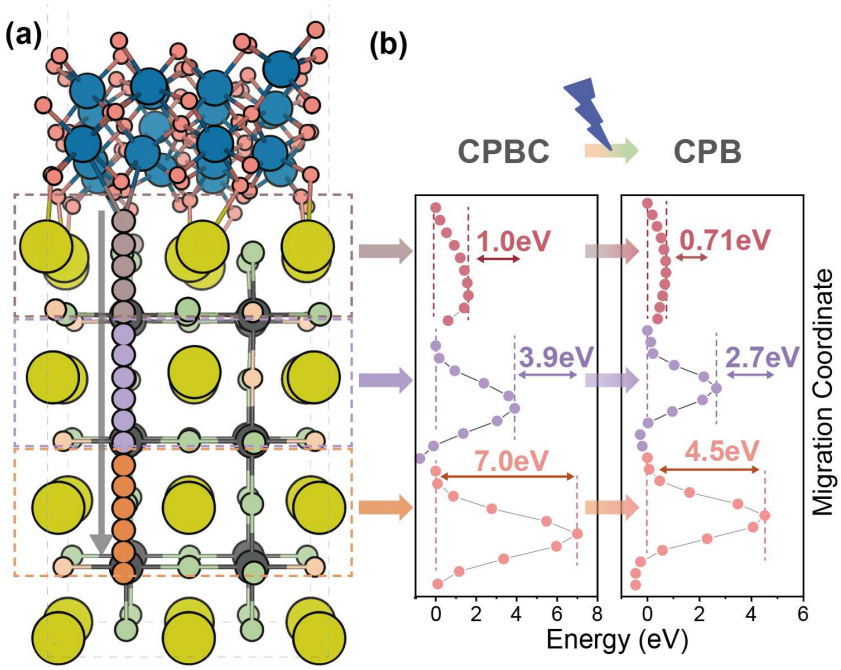

Figure 3.12 NEB migration path and energy barriers.

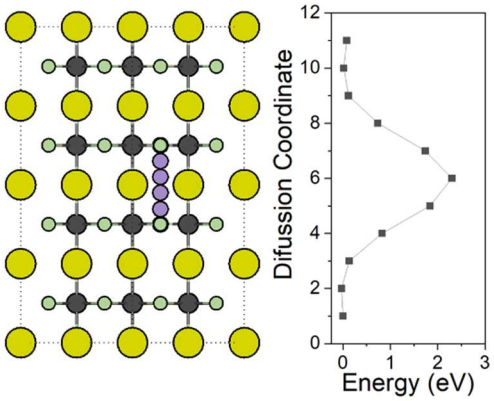

Figure 3.13 Br migration path and the corresponding energy landscape in bulk CPB.

Building upon the theoretical findings, the microstructural mechanisms behind the PL dynamics can then be constructed, which intriguingly replicate the behaviors of biological neurons (**Figure 3.14a**). Notably, the interface within MHPe@MYE (**Figure**

3.14b) is evidenced both experimentally and theoretically important behind the phenomena, giving rise to the memristor-like PL variation as shown in **Figure 3.14c**.

In specific, **Figure 3.14d** presents the illustrative process flowchart of high-energy "Write", dark recovery, and low-energy "Read" operations, with focus on the microscopic materials configuration evolutions, which corresponds to the NO. 1-5 frames as marked in **Figure 3.14c**. Frame 1 shows the initial state, featuring an interfacial area of defective MHPe and Br/Cl-anchored MYE surface. Upon intense "Write" light stimulation, the adsorbed halogen species would migrate to MHPe (Frame 2), with a progressively evolving energy barrier as evidenced in previous DFT simulation section. Consequently, the halogen composition of MHPe is altered under light stimulation, leading to changes in its PL properties. When the light stimulus is removed, these PL characteristics gradually recover in the dark as halogen species gradually migrate back to the MYE surfaces (Frame 3), enabling reversibility of PL variations. The "Read" operation utilizes a low-energy probing light that preserves the PL state for non-destructive readout (Frame 4), with the system subsequently returning to its initial state after resting without intense UV irradiation (Frame 5). After a period of rest, the system returns to its original state, supporting the repeatable "Write" and "Read" cycles essential for PL-based neuromorphic functionality in MHPe@MYE. Additionally, the stable Eu^{3+} luminescence from the MYE host provides a reliable baseline for calibrating optical responses.

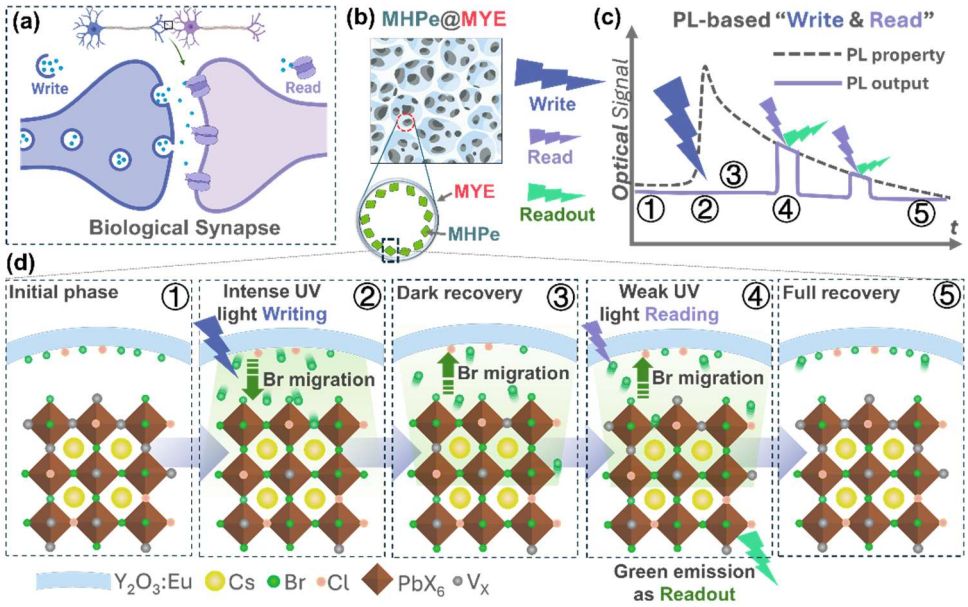

Figure 3.14 (a) Schematic of a biological synapse. (b) Schematic illustration of the MHPe@MYE smart nanocomposites with macroporous morphology. (c) Light-triggered PL variation in the MHPe@MYE composites by applying both the optical "Write" and "Read" operation, the tagged figures NO.1-5 representing the specific frames during the light-induced PL variations. (d) Illustrative schemes of microscopic variations at Frame No.1-5 in (c).

3.5 PL-based Neuromorphic behaviors

Building upon the theoretically adaptive halogen migration behaviors of MHPe@MYE, Further conducted comprehensive analyses of the PL excitation-emission relationships were conducted to investigate the neuromorphic behaviors of MHPe using programmed excitation light pulses.[98] **Figure 3.15** shows the proof-of-concept result of the synaptic PL behaviors of MHPe@MYE monitoring the 510 nm and 613 nm for MHPe and MYE emission, respectively. The excitation source utilizes

a commercial LED of 365 nm UV output controlled by the arbitrary waveform generator (AWG) with 2 Hz frequency and duty ratio of 50%. The initial stage required 85 high-energy "Write" excitation pulses (~161.15 μW/cm^2) to reach a pre-defined upper threshold as marked by blue dot line, followed by a dark recovery process monitored using low-energy probing pulses (~7.96 μW/cm^2). It then got to lower threshold, as marked in lavender line, after 72 "Read" spikes. Notably, subsequent cycles demonstrated an adaptive response, fort the 2nd round required only 36 "Write" pulses to reach the upper threshold but needed more time (equivalent to 90 "Read" pulses) to return to lower threshold. It indicates that the MHPe@MYE "*smart phosphor*" can memorize the lately excitation, results in faster PL variation and slower recovery. Such a memory effect was even more strengthened in the 3rd round, with 32 and 112 pulses for the "Write" and "Read" process, respectively. This progressive modification persisted though slightly faded after a brief recovery interval (1 min) as demonstrated in the 51 "Write" and 89 "Read" pulses for the 4th round potentiation. This intriguing PL variation behavior of MHPe@MYE resembles the adaptive memory effect known as experience-dependent plasticity observed in biological synapses. It refers to how a system's response to stimulation is modified by its prior excitation history, influencing both acquisition and recovery rates. In sharp contrast, Eu^{3+} PL emission from the MYE host only shows the single "on" and "off" states singly influenced by the energy density of excitation spikes, (~161.15 μW/cm^2 or ~7.96 μW/cm^2) showing on sign of neuromorphic characteristics. Furthermore, in MHPe@MYE smart nanocomposites, the coexistence of two types of synaptic (MHPe) and inert (Eu^{3+} in MYE) PL can be utilized for calibration inside the systems. In addition, similar consistency can be observed during the switching between "Write" and "Read" operation. To further characterize these neuromorphic properties, Further conducted detailed investigations

were performed into the PL variation process in search of specific biological phenomena and metrics, including stimuli-dependent synaptic plasticity, LTM, PPF, STP, and LTP effects.

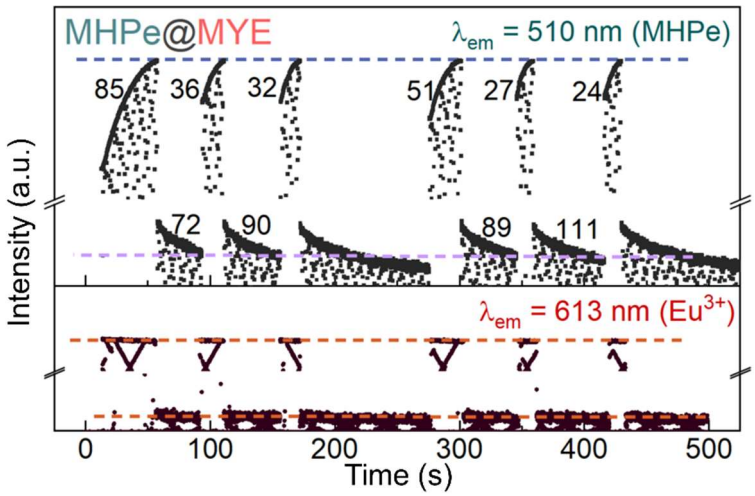

Figure 3.15 History-dependent PL dynamics of MHPe and inert Eu^{3+} PL dynamics co-existing in MHPe@MYE.

Biological neurons exhibit synaptic plasticity, which allows synapses to adapt their synaptic weight (SW) to varying stimuli. Such ability is crucial for the neurons in processing information and forming memory. PL-based SW of smart nanocomposites can be quantified by comparing the emission output intensities before and after receiving light spikes. SW's variation tendency under different stimuli further reveals stimulus-dependent synaptic behaviors of MHPe@MYE. In this research, the stimulus-dependent synaptic behaviors are investigated by changing the parameters of excitation light spikes, including emission wavelength (λ_{em}), excitation wavelength (λ_{ex}), excitation intensity (I_{ex}) and frequency (f). Taking the λ_{em} series as a reference (**Figure 3.16**), when monitoring shorter wavelengths (470-490 nm), the PL intensity exhibits faster growth at early spikes and tend to saturate earlier. For longer wavelength such as

510 and 520 nm, the variation at early stage becomes less significant. This is due to the slight redshift from 470 nm to 510 nm during early PL variations. The above tendency addresses the distinct synaptic behaviors under different λ_{em}. Notably, following 45-second gaps, fewer numbers of spike can suffice for MHPe@MYE to reclaim the same PL intensity, which is linked to its history-dependent adaptation ability.

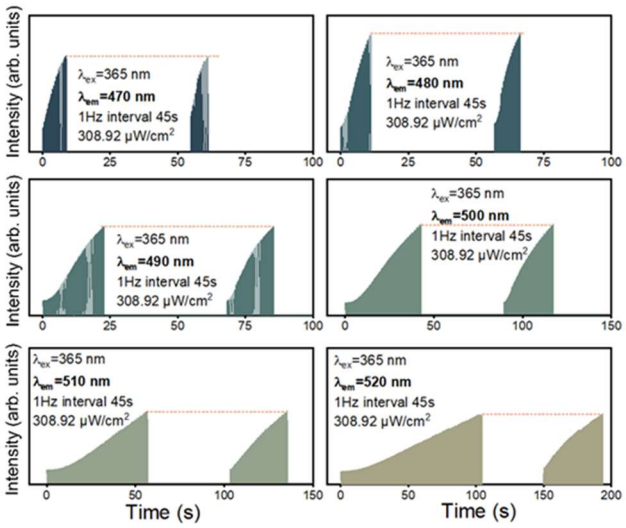

Figure 3.16 λ_{em}-dependent synaptic PL dynamics behaviors.

Similarly diverse synaptic evolution trends can be observed in the I_{ex} series. As demonstrated in **Figure 3.17**, the PL intensity values and variation speeds decrease monotonically as I_{ex} decreases, whereas the accelerated recovery behavior after 45 s interval can also be observed. When I_{ex} is further reduced to ~33.12 μW/cm^2, approaching the energy density of "Read" pulses (~7.96 μW/cm^2), MHPe@MYE's PL variations can no longer be observed.

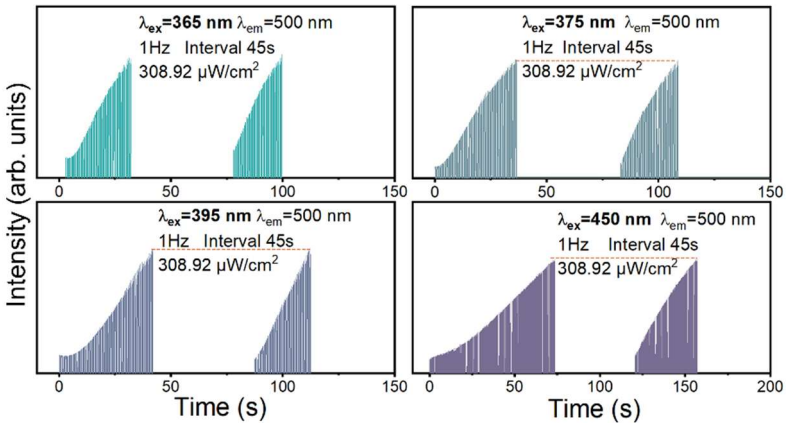

Figure 3.17 λ_{ex}-dependent synaptic PL dynamics behaviors.

As summarized in **Figure 3.18** similar progressive adaptations and preservation after short resting periods can be observed when varying other spike parameters (*i.e.*, *f*, λ_{ex}). In short summary, it demonstrates a positive correlation between larger SW values with shorter λ_{ex} and higher *f*. Across four measurements, the stimuli-dependent synaptic behaviors exhibited reliable performance with acceptable standard deviation (abbreviated as s.d., as marked in **Figure 3.18**). The rich and adjustable synaptic behaviors of MHPe@MYE smart nanocomposites through multiple excitation parameters can enhance the information bandwidth while providing flexibility in the neuromorphic functions. This could potentially lead to the design of task-adaptive physical reservoirs.[108] Moreover, this ability to sustain neuromorphic characteristics after notable *x* is similar to the LTM phenomena.

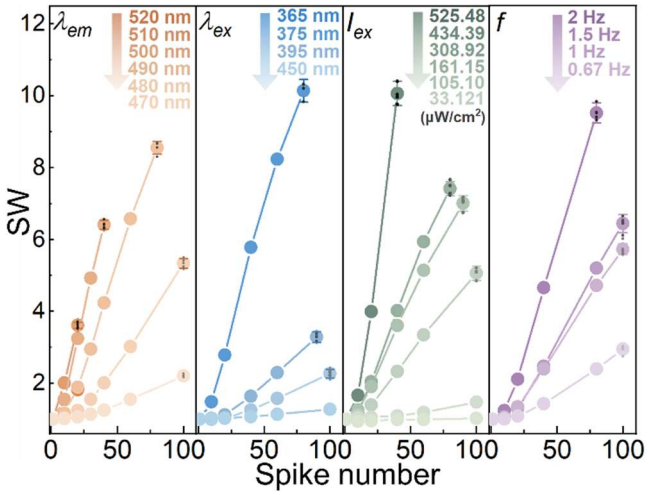

Figure 3.18 Summary of stimuli-dependent synaptic PL dynamics behaviors across various spike parameters.

In biological neurons, the LTM behavior represents a persistent modification of synaptic strength over relatively long periods. This phenomenon is often linked to the activation of receptors and subsequent Ca^{2+} influx, contributing to stable and experience-dependent memory. Here, the LTM effect of MHPe@MYE has also been carefully examined. A consistent "Write" pulse was programmed (1 Hz, duty 0.5 s, 365 nm, ~161.15 μW/cm^2) to trigger the PL variation of MHPe@MYE. The PL kinetics of **Figure 3.19a** demonstrate how the LTM factors were quantified. N_t depict the pulse number used for first-round excitation to the final intensity (I_t). After resting x, the PL intensity partially restored (I_x), and N_x shows the pulse number required to reclaim I_t. In addition, N_n represents the pulse number from I_x to I_t at the first round of excitations. After a dark recovery period (*e.g.*, 30 s), the system was subjected to "Write" pulses again from the second initial intensity (I_{30}). N_{30} represents the number of "Write" pulses needed to reach the threshold again after 30 seconds of rest, while N_n indicates the number of pulses required from I_{30} to I_t during the first round. Other N_x and I_x values (x

= 15, 30, 45, 60, 90, 120) were similarly determined despite the different resting time used at the interval of two rounds. **Figure 3.19b** summarizes the LTM parameters measured at various x, with corresponding raw PL kinetic diagrams displayed in **Figure 3.19c**. It demonstrates that a shorter resting time leads to a stronger I_x and fewer "Write" pulses (N_x) required to arouse the same I_t again. In addition, the N_x values are consistently smaller than N_n, with the memory gap (N_n - N_x) narrowing with longer resting times (larger x). In other words, a more recent potentization of MHPe@MYE results in better-preserved memory states and faster recalls, intriguingly replicating the LTM effects in biological neurons. Despite minor fluctuations, the five rounds of LTM measurements demonstrated stable correlations and margin s.d. error, confirming the reproducibility of MHPe@MYE's LTM behavior in the form of adaptive PL variation.

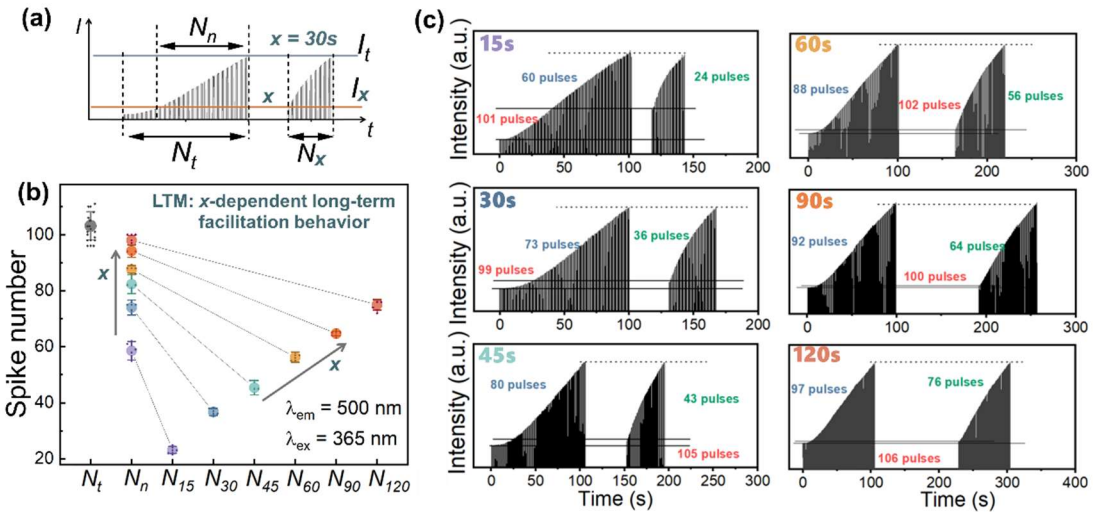

Figure 3.19 x-dependent LTM features of MHPe@MYE. (a) Definition of N_t, N_n, N_x, I_t, and I_x marked in the PL dynamics at 30 s resting interval (x = 30 s). (b) LTM behavior featuring the long-term x-dependent PL dynamics. (c) PL dynamics comparison with varying x.

Conversely, PPF determines the short-term plasticity of neuromorphic systems. It describes the phenomenon when two identical presynaptic stimuli delivered in succession elicits an increasingly strong postsynaptic response. In this work, the PPF has been measured at ~668.78 μW/cm^2 (365 nm,) and λ_{em} was chosen at 500 nm, since their fast adaptation is fastest during the initial phase. The PPF index is defined as the ratio of the two consecutive PL intensities. It generally exhibits a negative exponential relationship with the pulse interval (Δt):

$$PPF\ index = C_0 + C_1\ exp\left(-\frac{\Delta t}{\tau_1}\right) + C_2 exp\left(-\frac{\Delta t}{\tau_2}\right)$$

where C_0 is a constant, and C_1 and C_2 represent the initial facilitation degrees of these two phases. In the meantime, τ_1 and τ_2 are characteristic relaxation lifetimes for the fast-decay and slow-decay channel, respectively. **Figure 3.20a** and **b** show the PPF measurements at 0.5 s and 3 s intervals, respectively, and the resultant fitting curve is shown in **Figure 3.20c**. The fitted τ_1 and τ_2 values are 0.205 s and 5.04 s, respectively. These values are indicative of the fast and slow relaxation phases: the short τ_1 value suggests a rapid initial facilitation decay, which is crucial for the system to respond quickly to successive stimuli; the longer τ_2 value reflects a more gradual change in facilitation, which is essential for maintaining memories of previous stimuli over extended periods. The dynamics of such a dual-phase relaxation intriguingly replicate biological synaptic function, where both fast and slow components jointly underpin the intricate neural signal processing.

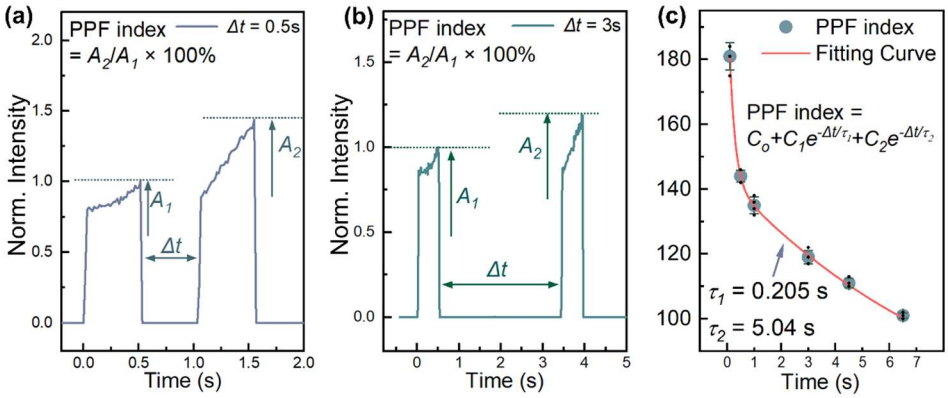

Figure 3.20 *Δt*-dependent PPF results measured with (a) 0.5 s interval, and (b) 3 s interval. (c) Measured PPF indices against interval times and the fitted decay curves. Error bars indicate the s.d. results from four points.

STP and LTP are fundamental mechanisms in biological systems that underlie the processes of learning and memory formation in the biological systems. STP acts as a transient filter for working memory, while LTP stabilizes salient data through lasting synaptic gain.[109] MHPe@MYE can replicate both phases in PL manners, with distinct decays readout after stimuli as monitored under "Read" excitations. As shown in **Figure 3.21a**, the MHPe@MYE's PL states are divided into STP after several "Write" spikes (green trace) and LTP upon receiving more excitation spikes (red trace). Eight separate measurements are superposed to confirm consistent trends for both STP and LTP with marginal deviations. Decay time constants can be acquired from the decay curves (**Figure 3.21b**) from STP and LTP, respectively, by fitting in the double exponential decay function:

$$y = y_0 + A_1\, exp\left(-\frac{\Delta t}{\tau_1}\right) + A_2 exp\left(-\frac{\Delta t}{\tau_2}\right)$$

The fitted decay lifetimes of LTP (τ_1 = 6.5 s, τ_2 = 41 s) is apparently larger than those of STP (τ_1 = 1.3 s, τ_2 = 29 s), while both showing tolerable s.d. errors (inset figure in **Figure. 21b**). By sustaining the potentiation beyond the STP timescales towards LTP, MHPe@MYE effectively replicates enduring synaptic changes. This alignment with core principles of biological synaptic plasticity and confirms its emulation of biomimetic function.

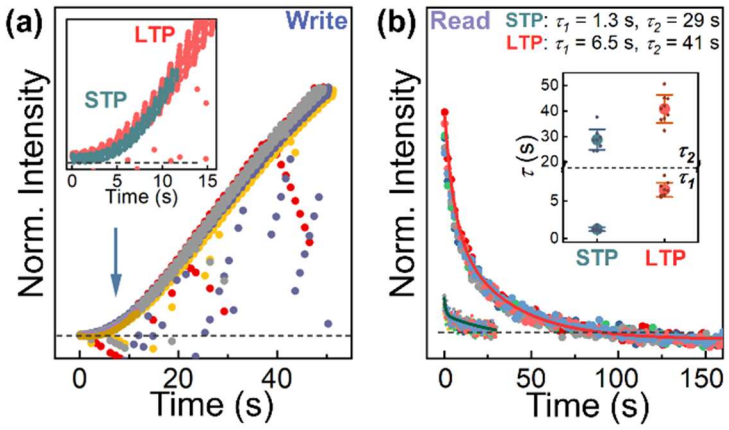

Figure 3.21 (a) PL kinetics during the formation of STP and LTP, the inset figure gives the beginning of PL evolution for STP (green) and LTP (red), demonstrating notable reproducibility(f) PL dynamics during the decay of STP and LTP, and the corresponding fitting curves. Inset displays the fitted decay time constants.

Four additional batches of MHPe@MYE synthesized using identical procedures confirm the reproducible nanocomposite structure and neuromorphic PL profiles across all MHPe@MYE samples. A high batch-to-batch uniformity is observed in both the PL properties and structural features of the newly prepared MHPe@MYE samples. As shown in **Figure 3.22a**, the XRD profiles and phase ratios are almost identical to the previous XRD results. SEM images of the new sample also demonstrate the similar

morphology of the porous structure compared to previous data (**Figure 3.22b**). More importantly, the PL properties of the new batch of MHPe@MYE closely match those of the previous samples in several key aspects:

1. PL dynamics with progressively enhanced MHPe emission and stable Eu emission—the ability of dark-recoverable PL variations (**Figure 3.22c**);
2. Inert PL dynamics of MHPe at weak excitation—important for the "Read" operation (**Figure 3.22d, e**);
3. History-dependent PL variation at "Write" and "Read" operations—indicative of PL-based neuromorphic behaviors (**Figure 3.22f**).

These findings confirm that the properties and performance of the materials are highly consistent, suggesting that MHPe@MYE smart nanocomposites generally exhibit good reproducibility in materials syntheses. In fact, inorganic phosphor materials are known for their stable PL properties when synthesized using optimized procedures, which further leads to predictably stable performance.

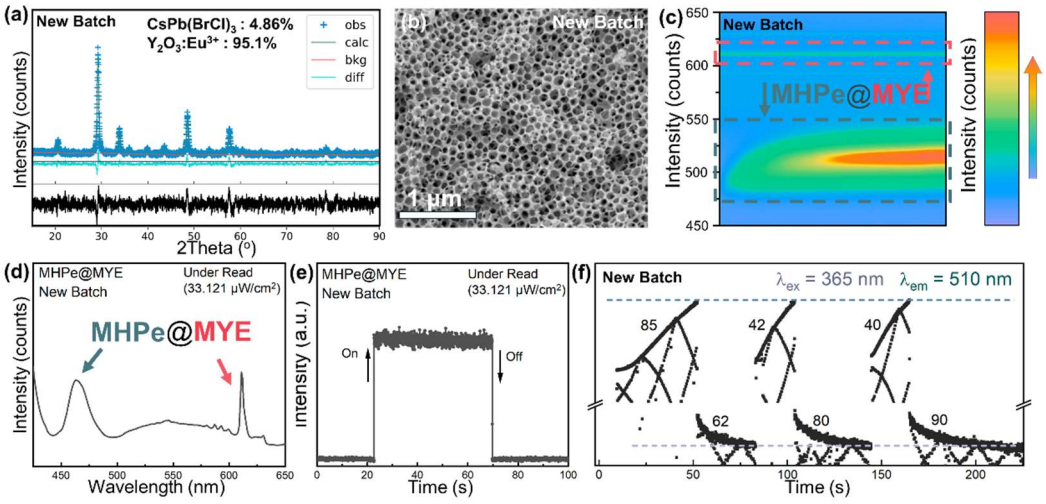

Figure 3.22 (a) XRD refinement results of new batch of MHPe@MYE, with the phase ratio tagged. (b) SEM images of new batch of MHPe@MYE. White scale bar indicates

1 μm. (c) time-resolved PL mapping of new MHPe@MYE measured under 360 nm laser excitation. (d) the PL emission spectrum measured at "Read" excitation (λ_{ex} = 365 nm, I_{ex} = 33.121 μW·cm^{-2}). (e) PL kinetic under "Read" excitation (λ_{ex} = 365 nm, λ_{em} = 510 nm, I_{ex} = 33.121 μW·cm^{-2}). (f) The PL dynamics acquired under "Write" and "Read" excitations, demonstrating similar history-dependent PL variation behaviors.

3.6 Summary

In this chapter, the MHPe@MYE "*smart phosphor*" is developed and systematically characterized.[98] The synthesis procedure combined hard-templated sol-gel techniques with solvent evaporation to yield uniform porous nanocomposites. Structural analyses confirmed phase purity and uniform dispersion. Dynamic PL studies show an increasing green emission from MHPe and a stable red emission from the MYE host. DFT calculations highlight the stronger Cl adsorption on Y_2O_3 surfaces and a progressively evolving Br migration barriers at the interfaces. Such an interface-mediated process enabled reversible compositional modulation of MHPe under light stimuli, resulting in light-induced PL properties variations. Under programmed excitation light spikes, the PL variations of MHPe@MYE exhibit intriguing synaptic-like behaviors, including PPF, LTM, STP, and LTP with notable reproducibility. A weak-energy "Read" mechanism is also established for non-destructive probing of the temporal PL states of MHPe@MYE. These results establish the MHPe@MYE smart nanocomposites as a potential neuromorphic platform. It is anticipated that MHPe@MYE can empower full-PL-based neuromorphic computing with optical-stimuli and PL-readouts.

Chapter 4 Full PL-based Physical Reservoir Computing based on MHPe@MYE Smart Nanocomposites

4.1 Introduction

Leveraging the intrinsic physical properties of materials to design neuromorphic computing systems has emerged as a promising strategy for reducing device complexity and enabling novel computational functionalities. Physical reservoir computing exemplifies this approach by utilizing the natural nonlinear dynamics and high-dimensional state space inherent to physical substrates to process temporal information. Thereby it can eliminate the need for elaborate device architectures or precise control over internal parameters. This paradigm not only simplifies hardware implementation but also opens the door to exploiting unique material phenomena for signal processing and pattern recognition tasks.

From the algorithmic point of view, reservoir computing is a brain inspired computational paradigm that reconfigures the nonlinear transient dynamics of a high dimensional dynamical system to map temporal inputs onto desired outputs through a trainable linear readout layer rather than by altering the internal parameters of the reservoir itself.[110] This structure fundamentally differs from feedforward neural networks (FNN). As compared in **Figure 4.1a**, FNN implements directed acyclic graphs and lack recurrent connections necessary for temporal dynamics and fading

memory; while in **Figure 4.1b,** the reservoir acts as a fixed spatiotemporal kernel that expands low dimensional signals into a rich feature space where linear separation becomes feasible while simultaneously providing fading memory that encodes historical context. By decoupling the complex recurrent dynamics from the learning process reservoir computing circumvents the vanishing and exploding gradient issues that plague conventional recurrent neural networks and enable efficient hardware implementation even when precise device engineering or detailed physical models are unavailable. In this framework only the final readout weights are optimized typically via ridge regression that could dramatically reduce computational cost of training. It thus makes the approach compatible with unconventional substrates, whose internal states cannot be continuously tuned. The essential requirement of physical reservoir is that the system can exhibit sufficient nonlinearity, high state dimensionality, and the echo state property that ensures reproducible responses to specific input sequences, while maintaining the short-term memory at time domains.

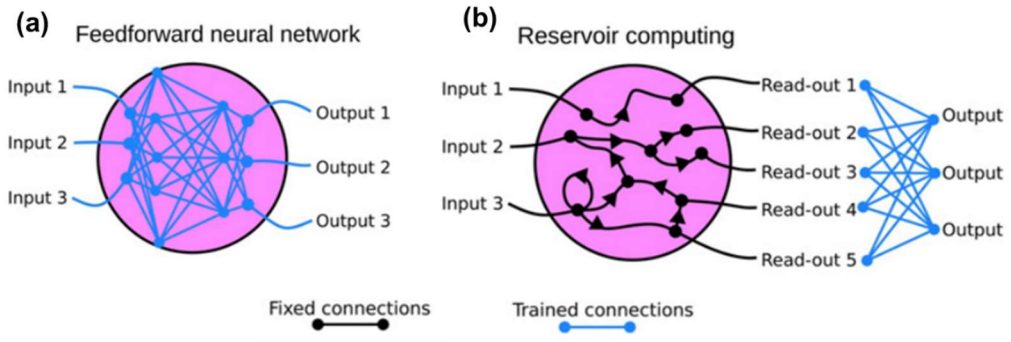

Figure 4.1 (a) Illustration of the FNN with acyclic and trainable connections, (b) the untrained connections within the network of a reservoir computing.[110]

Physical reservoir computing potential has been exploited based on material-specific implementations across multiple media (**Figure 4.2**).[111] The conventional electronic reservoirs have been mostly capitalized on the electrical nonlinearity and

memory effects in analog circuits and memristive devices, which has secured a promising path to hardware implementations. The optoelectronic reservoirs have also been extensively studied by exploiting the dynamics features of photodetectors and phototransistors. Recently, the spintronic and mechanical reservoirs also emerged with distinct dynamic mechanisms and input/output modes. Notably, the potential of phosphor materials as physical reservoir remains unexplored despite their promising potentials. PL-based reservoirs could utilize light-matter interactions where input-driven excitation generates emission spectra as high-dimensional states, enabling direct optical readout of reservoir dynamics. Crucially, employing PL emission output offers unique advantages, such as the direct visualization of reservoir states as spectral features or spatial patterns, which can effectively provide an intuitive diagnostic tool for reservoir system without additional transduction mechanisms. Such transparency also aligns well with the core principle of leveraging untrained physical dynamics while further reducing operational complexity through intrinsic state visualization.

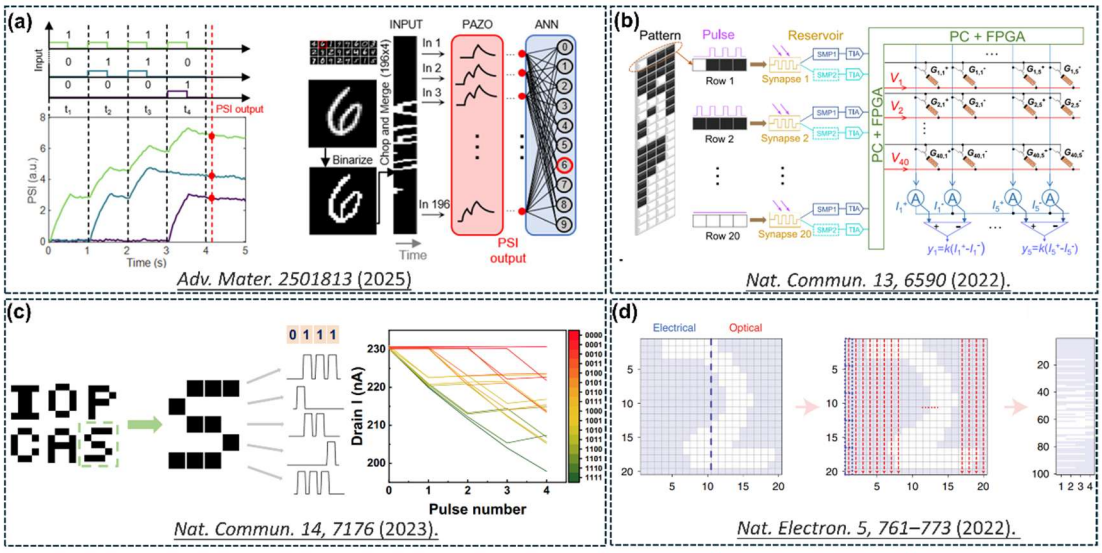

Figure 4.2 Examples of physical reservoir computing based on materials' chemical and physical properties with non-linear characteristics. (a) All-optical physical reservoir

computing based on light-responsive organic materials.[112] (b) In-sensor reservoir computing phototransistors hardware based on GaO_x.[113] (c) Electrical physical reservoir computing based on oxygen ion dynamics of HZO/LSMO thin films.[114] (d) Mixed-mode physical reservoir computing based on FE α-In_2Se_3.[115]

Following the previous experimental characterization of neuromorphic PL behaviors in MHPe@MYE smart nanocomposites, this chapter examines their implementation as all-optical physical reservoir computing platforms. Experimental results demonstrate that the engineered MHPe@MYE is capable of processing temporal optical information through programmable "Write" excitation inputs, which progressively induce reversible PL state variations. The as-established non-destructive "Read" operations enable the extraction of converted PL emission features, serving as computational outputs of the reservoir. Such an ability to process temporal information is further evidenced by the distinct PL dynamic mapping of 4-bit binary sequences, where unique input patterns generate separable high-dimensional PL feature spaces within the PL dynamics. The PL-based physical reservoir can facilitate downstream recognition tasks when integrated with software-based ANN. The effectiveness of this approach has been validated in MNIST handwritten digit recognition and SOCOFing UV fingerprint authentication, confirming the feasibility of PL-based reservoir computing for image recognition tasks. This strategy maintains fully optical input-output operation and leverages intrinsic material dynamics to achieve efficient and robust computational performance.

4.2 Discrimination of 4-bit binary sequences

The previously discussed neuromorphic properties of MHPe@MYE in PL variation process offer an interesting opportunity to construct a full PL-based neuromorphic computing systems with both optical input and output.[98] Particularly, the volatile, progressively adaptive, and nonlinear responsive characteristics match well with the fundamental principles of reservoir computing, *i.e.,* the nonlinear transformation of input signals, temporal memory effects, and high-dimensional projection of data.[110,116] Consequently, MHPe@MYE can be adapted for all-optical physical reservoir computing. In the designed experiment, "1" represents a duty cycle in the "Write" waveform, while "0" corresponds to a blank cycle. For "Read" operations, a continuous LED light source is used to effectively track the feature space. Optical inputs use 365 nm "Write" pulses (~668.78 μW/cm^2), and outputs were the resultant PL intensity at 500 nm under low power excitation (~7.96 μW/cm^2). The input architecture encoded 4-bit binary sequences using 1 Hz periodic pulses with a 0.5s duty ratio, as demonstrated by the "1011" waveform shown in **Figure 4.3**. Appropriate long-pass filters (395 nm or 460 nm) were used to avoid excitation light interference. A synchronized transistor-transistor-logic-controlled electronic shutter (Keshengda Optoelectronic) was installed in the front of the PMT photodetector, where any high-intensity "Write" duty leads to the closure of the electronic shutter. The detection system was optimized by adjusting slit width to specifically monitor "Read" signal intensities.

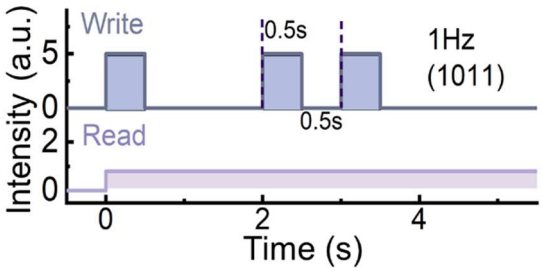

Figure 4.3 Waveform setups of 4-bit binary sequence

The 16 possible 4-bit binary codes are then transformed into 16 set of PL dynamics features of MHPe@MYE. As shown in **Figure 4.4**, all 16 I_{em}-t curves (from "0000" to "1111") exhibit distinct PL dynamics features with notable reproducibility as marked in 16 different colors. Such results illustrated that MHPe@MYE physical reservoir can retain a stable fading PL property for every binary sequence input. In other words, the output PL signals reflect both the immediate input and the system's real-time state, demonstrating consistent mapping of nonlinear 4-bit input sequences to corresponding output PL dynamics.

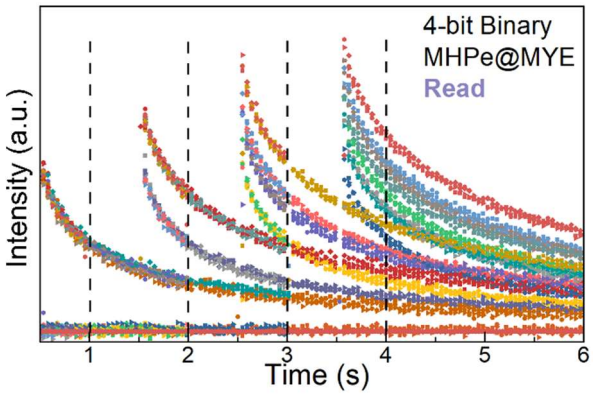

Figure 4.4 16 distinct PL dynamic features correspond cv to all 4-bit binary sequences.

In device operation, discrete measurements of sampling point (SMP) can efficiently reconstruct the input 4-bit signal rather than continuous "Read" operations, facilitating a more efficient and streamlined analyses. In that case, several SMPs were selected in the specific time position in the measured PL dynamics. **Figure 4.5a** gives the marked time locations of SMP1, SMP2, SMP3, and SMP4, and the corresponding PL readouts of 16 binary sequences are listed in **Figure 4.5b**. However, some overlaps can be found among the possible PL readouts. For instance, the SMP1 and SMP2 were located before the duty range of the 4th sequence, caused the last digit becomes totally undistinguishable. On the other hand, the PL readout intensity table of SMP3 and SMP4 also demonstrate slight overlaps in, for example, between "1001-0101" and "1011-0111". The reason can be assigned to the information of 1st digit become less significant when "Reading" at the 4th digit.

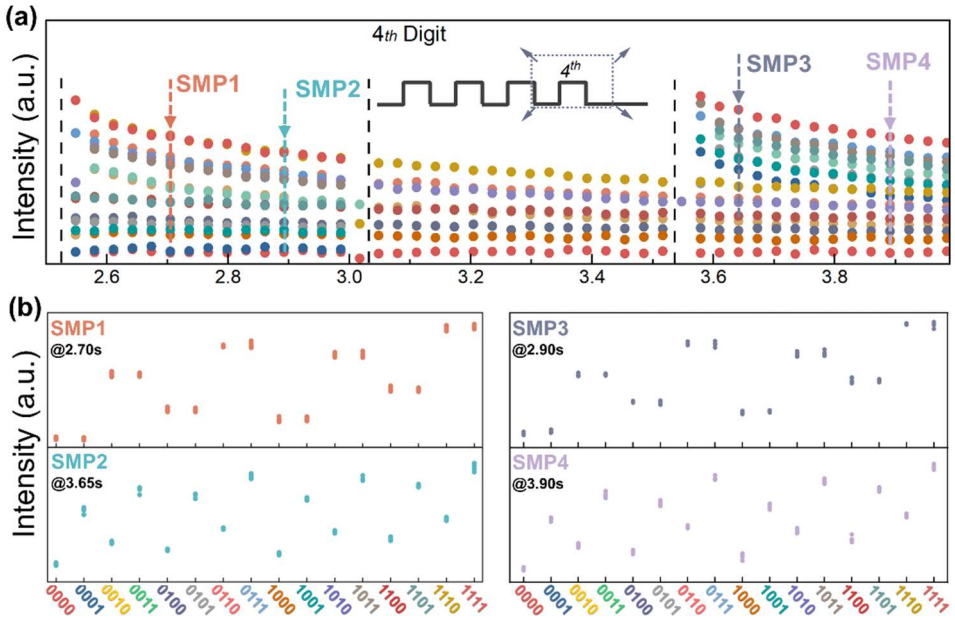

Figure 4.5 (a) Configurations of SMP points in the PL dynamic features. (b) The extracted readout intensities of SMP1, SMP2, SMP3, and SMP4.

The indistinguishable sequences could lead to deviated correlation among PL features and original 4-bit sequences. As a consequence, it may induce wrong readouts during the data conversion of physical reservoirs. Such wrong readouts may greatly impede the downstream tasks, especially for complex and large tasks. In order to diminish overlaps in PL features and therefore avoid wrong readouts, a feasible method is to apply multiple SMP points. While multiple SMPs decrease the dimension of data projection and may increase converted data amount, it facilitates the higher quality of the convert data. **Figure 4.6** demonstrate the 2D PL intensity features using both SMP1 and SMP2, showing the clear discrimination of all 16 4-bit binary sequences by dual-SMP approaches.

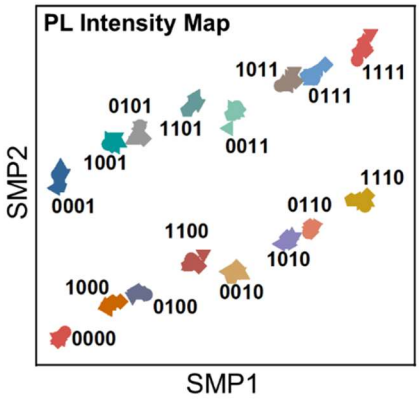

Figure 4.6 2D PL feature maps for distinguishing 4-bit binary sequences.

4.3 PL-based handwritten digit classification

Building upon the demonstrated capability of MHPe@MYE to function as a PL-based physical reservoir, its intrinsic material properties enable the transformation of time-resolved sequential optical pulse inputs into PL intensity readouts at designated SMPs. This mechanism establishes a versatile platform for processing all forms of

binary encoded temporal signals, where information can be mapped through a full PL manner. In order to further examine feasibility of MHPe@MYE to be used in all-optical physical reservoir, the MNIST dataset is first employed to test the handwritten digit classification capability.[117] To cope with the MHPe@MYE physical reservoir's PL-based "Write" and "Read" processes, the MNIST images are preprocessed into stripes of 4-bit binary codes. In specific, the MNIST dataset was preprocessed by binarizing and resizing to 28 × 28 pixels using default *OpenCV* methods (**Figure 4.7**).[118] Then, the original image is divided into columns of 4 pixels in width from left to right (**Figure 4.8**a). These columns are sequentially re-connected end-to-end to form a long strip of 196 pixels in length, as indicated by the colored dot cycles (**Figure 4.8b**). Each line of the processed images represents a 4-bit binary number, which are then used to modulate the input light waveforms as "Write" signal to MHPe@MYE physical reservoir. Three virtual device models were simulated: Dev1 with dual-feature (SMP1 & SMP2) reading capabilities and other two single-SMP "Read" modes (SMP1 for Dev2 and SMP2 for Dev3). The PL intensity readouts at different SMPs are mapped from the experimental PL readouts, are randomly assigned as processed results.

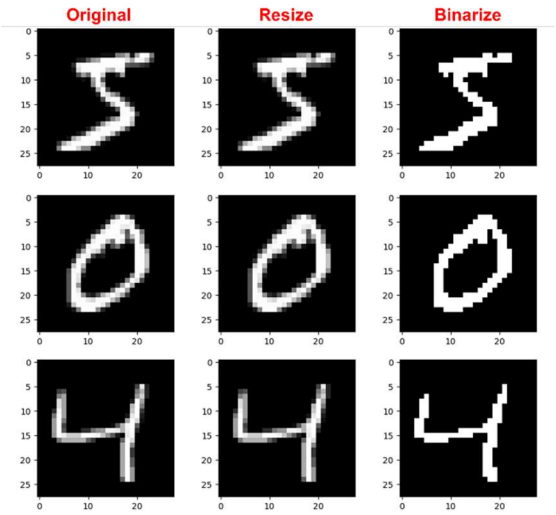

Figure 4.7 Example of image preprocessing of MNIST.

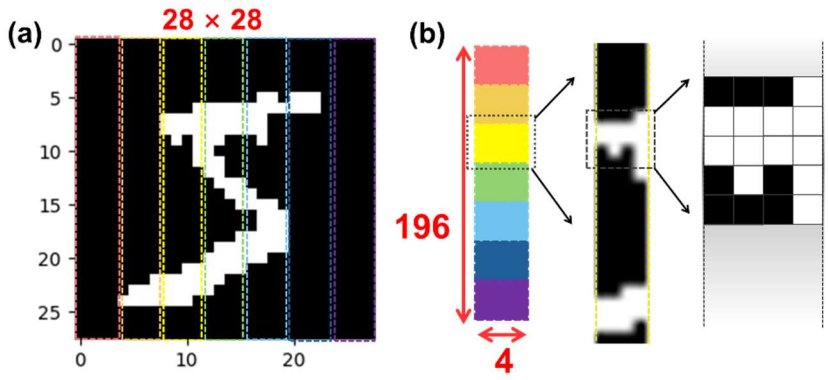

Figure 4.8 (a) Crop of MNIST image into width of 4 pixels, and (b) the consequent rejoining of cropped images to form 4-bit strips.

As discussed above, the overlaps in PL readouts of different input sequences impede the reconstruction of original data. As compared in **Figure 4.9a** and **b**, it demonstrates the converted images from simulated PL readouts using different SMPs, which shows noticeable loss of feature in Dev2 and Dev3; Especially for Dev3 with SMP2 only, the exclusion of last digit has induced a significant loss of origin features during physical reservoir computing, which is detrimental to downstream classification tasks. The processed results are fed into a software-based ANN, which has a simple structure for comparing the reliability of different SMP readouts (**Figure 4.9c**). It consists of an input layer with 196 nodes, a hidden layer with 16 neurons using *ReLU* activation, and an output layer with 10 nodes using *SoftMax* activation representing digit classifications (10 classes representing 0-9). The ANN employs the *Adam*[119] optimizer, which adaptively adjusts the learning rate using the first and second moment estimates of the gradients.

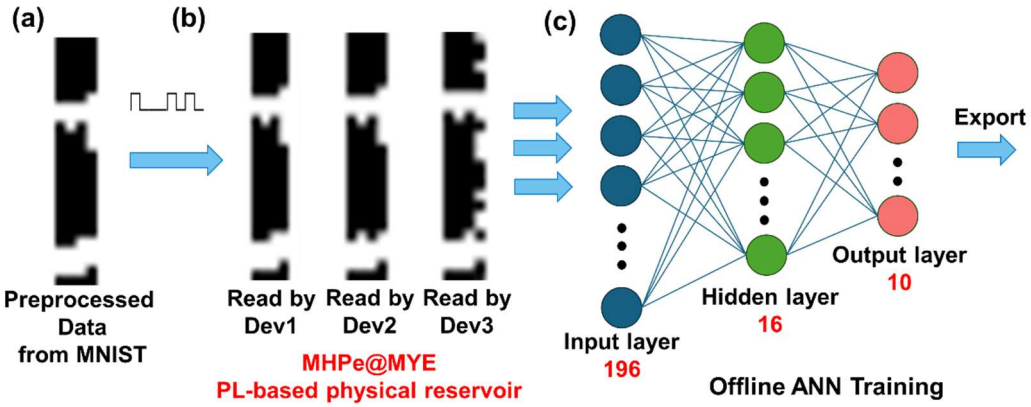

Figure 4.9 Device setups using extracted PL features mapped from experimental results.

Training outcomes in **Figure 4.10** indicate 92% accuracy for Dev1 (SMP1 & SMP2) at epoch 20, compared to 87% (Dev2, SMP1) and 90% (Dev3, SMP2). respectively. Notably, Dev2 and Dev3 exhibited faster learning on the training set but performed poorly on the validation set due to overfitting caused by system errors in the single-feature SMP modes. This result highlights that the dual-feature SMP device offers more reliable performance for all-optical data processing tasks even at simple MNIST classification tasks. The dual-SMP mode of Dev1 further illuminates specific strengths in digit classification capabilities across all 10 numbers without notable weakness as illustrated in the confusion matrix in **Figure 4.11**. It shows robust performance through high diagonal counts like 929 for digit 0 and 1107 for digit 1, showing robust overall reliability in handling the MNIST dataset.

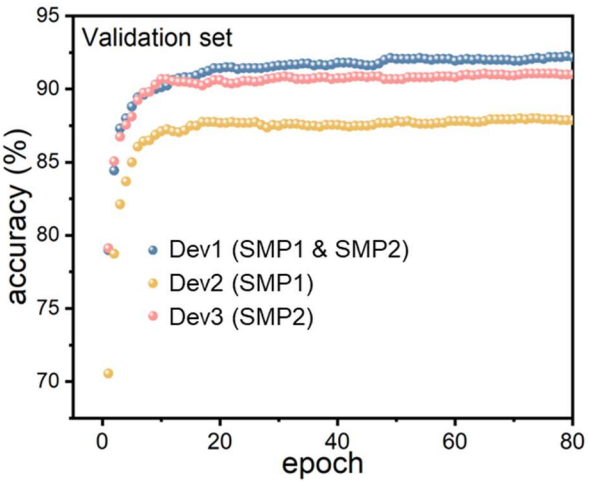

Figure 4.10 Training records for MNIST handwritten digit classification

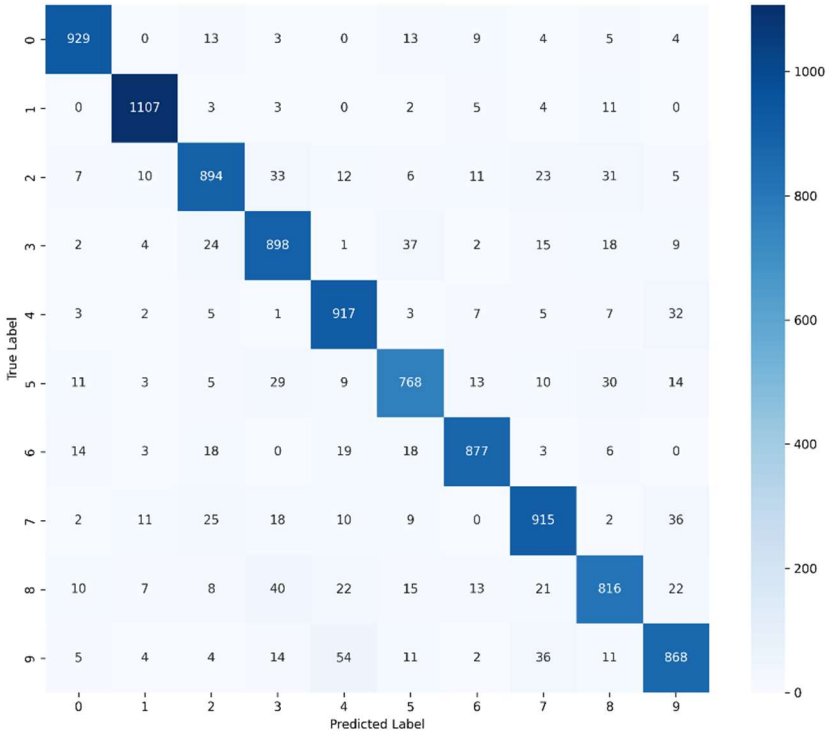

Figure 4.11 Confusion matrix of MNIST classification using Dev1 dual-SMP setup.

4.4 PL-based latent UV fingerprint recognition

Building upon the validated capabilities of MHPe@MYE's as a physical reservoir and optimized SMP setups, its potential application in all-optical fingerprint recognition based on UV images from the SOCOFing dataset has been further examined.[120] The importance of distinguishing between authentic and counterfeit fingerprints has significantly increased in modern security systems. While optoelectronic and capacitive sensors are typically employed for processing UV light inputs, these traditional devices are susceptible to environmental interference and can be fooled by high-quality replicas, thereby necessitating the development of alternative methods. Here, this study shows that MHPe@MYE "*smart phosphor*" can potentially replicate this process through a full PL-based manner. The workflow of proposed PL-based physical reservoir computing for fingerprint authentication using MHPe@MYE "*smart phosphors*" is schematically illustrated in **Figure 4.12**. The UV camera captures fingerprint patterns based on their unique UV adsorption properties, which are then directly converted into sequences of UV light pulses (365 nm) for processing by the MHPe@MYE. The simulated PL readouts are then similarly fed into software ANN for offline training. Notably, only the weights in the readout layer should be updated by capitalizing on the inherent data transformations of the MHPe@MYE "*smart phosphor*" as physical reservoir. This approach not only harnesses MHPe@MYE's preprocessing capabilities but also enhances specificity towards a defined outcome while mitigating the risks of overfitting.

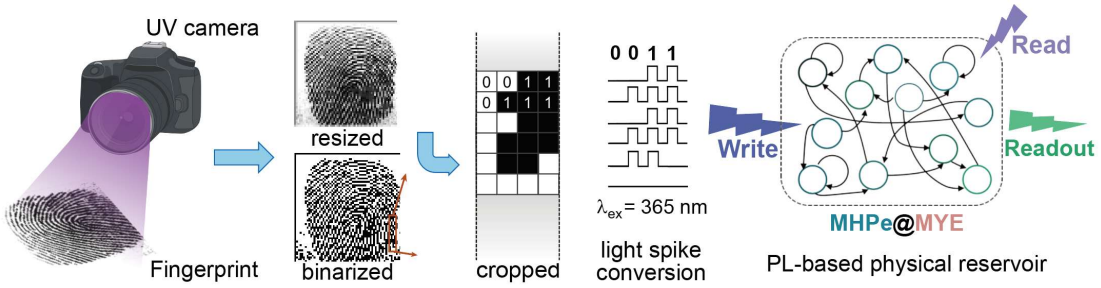

Figure 4.12 Flowchart of latent PL-based UV fingerprint recognition using MHPe@MYE as physical reservoir.

Notably, artificial fingerprint recognition involves more complicated tasks compared to MNIST, particularly due to the much larger images in the SOCOFing dataset (*96* × *106* pixels). These larger fingerprint images contain significantly more information per pixel, posing a greater challenge for traditional data preprocessing methods to effectively extract and recognize the relevant features. Therefore, the data preprocessing capabilities of the "*smart phosphor*" MHPe@MYE synaptic device become pivotal in order to simplify the computation while maintaining accuracy. Extensive binarization and resizing techniques were explored as compared in **Figure 4.13**, where the adaptive thresholding method is selected during binarization upon resizing the image to *64* × *64* pixel due to their good performance in balancing the training cost and preservation of features. As shown in **Figure 4.14**, the cropping, rejoining preprocessing, and experimentally extracted PL features as inputs for offline training, are similar to the case of MNIST

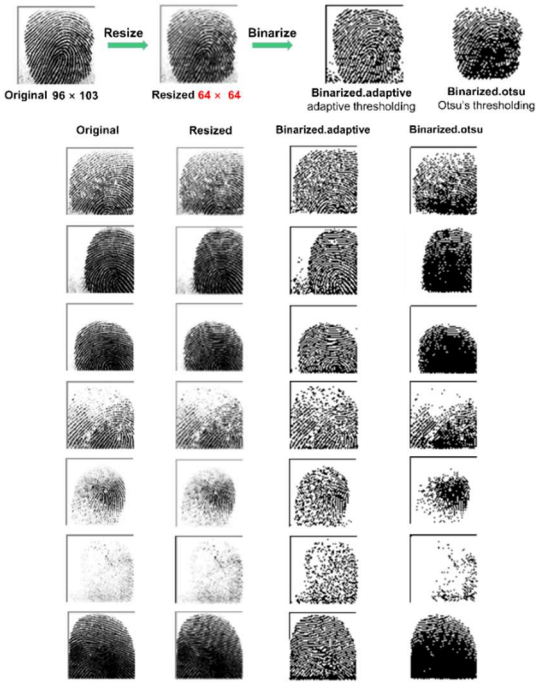

Figure 4.13 Examples for comparing the *Ostu* and adaptive threshold binarization method for 64 × 64 resized SOCOFing images.

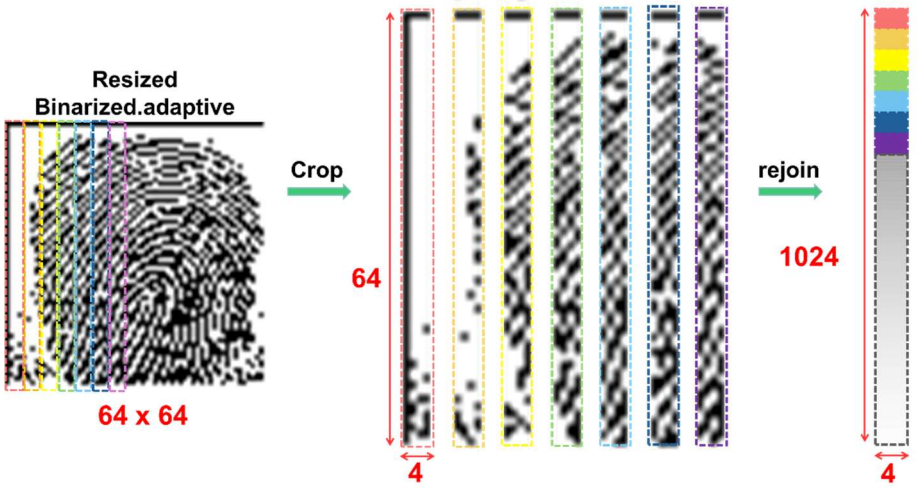

Figure 4.14 Crop and rejoin process for SOCOFing fingerprint images.

To cope with the complex fingerprint recognition tasks, a more complex ANN structure was used. As shown in **Figure 4.15a,** it consists of three convolutional layers

(32, 64, and 64 filters with 2×2 kernels) with Rectified Linear Unit (*ReLU*) activation and max-pooling layers (2×2), followed by two dense layers (64 neurons and 2 neurons) for binary classification. Following an 0.64/0.16/0.2 for train/validation/test split, the ANN was trained with the *Adam* optimization with initial η = 0.001. Additional optimization techniques were implemented including learning rate reduction and callbacks like *ModelCheckpoint* and *EarlyStopping* to prevent overfitting. To ensure reproducibility of training records, a fixed seed was set for consistent randomization across all computational steps.

The software-based offline training results were plotted in **Figure 4.15b**, showing that the dual-feature reading method (Dev 1) leads to a much higher accuracy throughout the training process, and finally reaches an accuracy of 94.4% after 60 epochs. The recognition records after training are found similar to other reported neuromorphic devices in spite of the different input/output modes or mathematical algorithms.[82-84,121] On the other hand, the Dev 2 (using SMP2 only) gives a much lower recognition accuracy of 84.2% after training the same databases. As compared in **Figure 4.15b** to **e**, such a difference between Dev1 (dual-SMP) and Dev2 (single-SMP) methods is observed through different resizing criteria. It highlights the importance of effective PL feature discrimination by employing two SMPs when dealing with complex image recognition tasks like fingerprints. In addition, **Figure 4.16** gives a summary of the training records, including the accuracy and loss of SOCOFing recognition of various resizing strategies. Further reduction in image size during preprocessing leads to drastic feature loss, resulting in diminished accuracy and increased loss. The *64 × 64* resize method demonstrated a balanced high accuracy with minimal computational overhead.

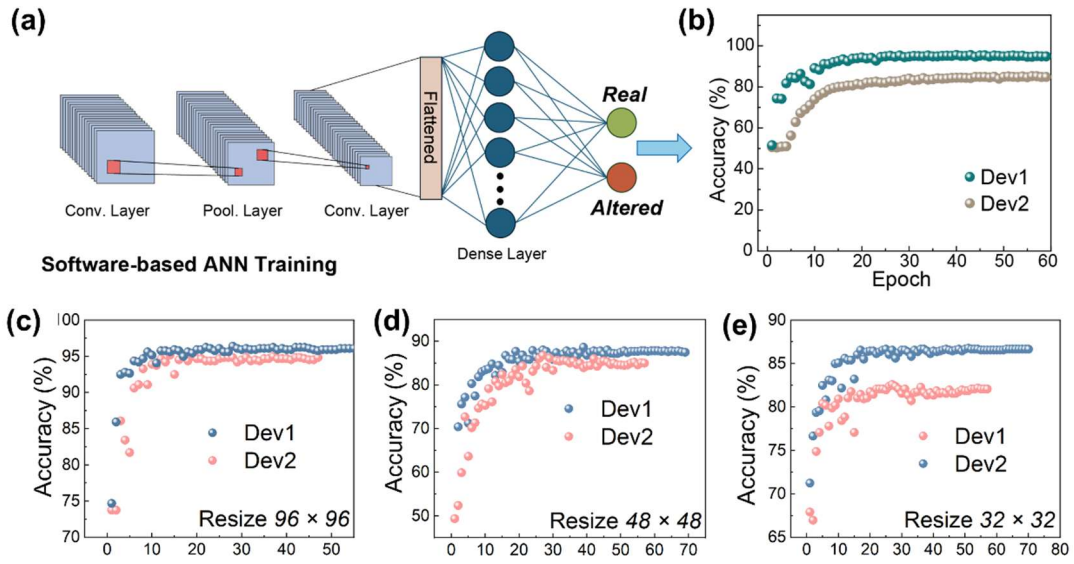

Figure 4.15 (a) Offline software-based ANN training methods. Training record of SOCOFing fingerprint recognition using MHPe@MYE as PL-based physical reservoir using (b) 64 × 64, and other resized scheme including (c) 96 × 96, (d) 48× 48, and (e) 32× 32 fingerprint images.

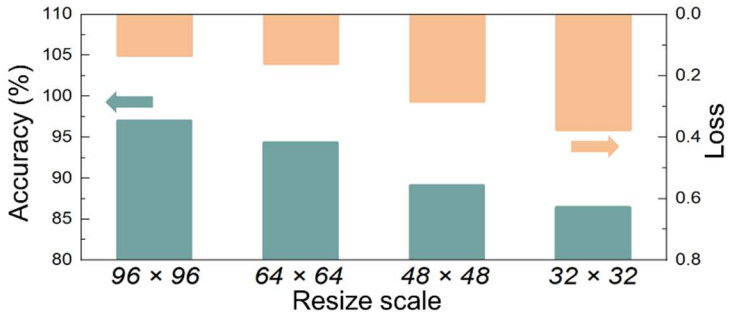

Figure 4.16 Summary of accuracy and loss metrics among difference resize of SOCOFing.

4.5 Extended PL-based physical reservoir

The concept of PL-based physical reservoir computing can be applied to other phosphors with adaptive PL variation characteristics at time domains, such as PersL

phosphors, although the lack of explicit "Read" operations may hinder the performance in complicated cases. For instance, similar dynamic PL features were constructed based on three classic PersL phosphors $Sr_2MgSi_2O_7:Eu^{2+},Dy^{3+}$, $SrAl_2O_4:Eu^{2+},Dy^{3+}$ (SAO), and $CaS:Eu^{2+}$ (commercially available from Foshan Juliang) with blue, green, and red emission, respectively. The "Write" process features PL excitation by programmed light pulses from a 365 nm LED driven by AWG, similar to the case of MHPe@MYE. No probing "Read" pulse could be applied, and the continuous decay of PersL serve as the output signal for the PersL-based reservoir.

The PL emission spectra of the three PersL phosphors under 365 nm excitation are shown in **Figure 4.17a**, with full coverage of the visible spectrum for a potentially higher information bandwidth. Their PersL decay kinetics directly define appropriate "Write" parameters in each case (**Figure 4.17b-d**): the faster-decaying PersL phosphor ($Sr_2MgSi_2O_7:Eu^{2+},Dy^{3+}$) requires higher-frequency input pulses (3 Hz) to resolve multistate sequence encoding, while the slower systems (SAO, $CaS:Eu^{2+}$) demand adjusted duty cycles and frequencies to align with their PL dynamics timescales. This adaptability highlights that PL-based reservoir performance hinges not only on intrinsic material superiority but also on tailored operational parameter designs to optimize the dynamic PL features at appropriate time domains.

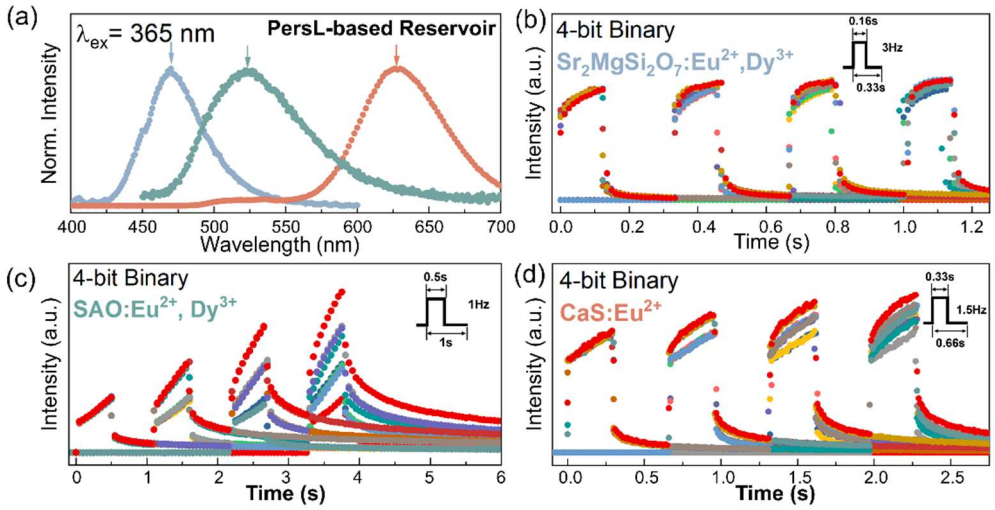

Figure 4.17 Conceptual investigation of PersL-based all-PL reservoir properties. (a) PL emission spectra of PersL phosphor $Sr_2MgSi_2O_7:Eu^{2+},Dy^{3+}$ (blue), SAO (green), and $CaS:Eu^{2+}$ (red) under 365 nm excitation. The "Write-only" feature spaces of potential all-PL 4-bit reservoir using (b) blue PersL of $Sr_2MgSi_2O_7:Eu^{2+},Dy^{3+}$ with 3 Hz light pulse input, (c) green PersL of SAO with 1 Hz light pulse input, and (d) red PersL of $CaS:Eu^{2+}$ with 1.5 Hz light pulse input. Inset diagrams show the corresponding excitation waveforms of light stimuli.

Although their neuromorphic properties are all based on PL processes, they show utterly different aspects. As compared in **Figure 4.18a** and **b**, the PersL-based systems exhibit neuromorphic behaviors in the form of decaying post-stimuli luminescence signals, whereas the MHPe@MYE "*smart phosphor*" with dark-state PL properties variations demonstrate distinct "Write" and "Read" functions.

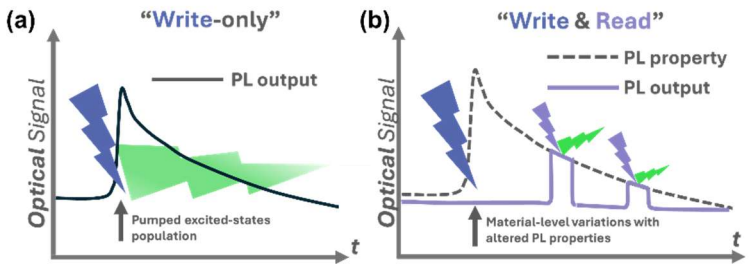

Figure 4.18 Schematical illustration of the different neuromorphic PL behaviors between existing (a) "Write-only" systems and (b) The constructed variation-type "Write & Read" MHPe@MYE "*smart phosphor*".

Therefore, this work has accordingly classified current PL-based neuromorphic systems into two categories:

"Write-only" Decay-type systems: exemplified by PersL and PA UC that rely on continuous PL decay following initial stimulation. Information can only be passively retrieved through the ongoing PL decay, resulting in "Write-only" operations.

"Write & Read" Variation-type systems: as proposed in this work, these systems exhibit history-dependent PL property variations in dark states. This is originated from light-induced materials-level variations that simultaneously alter its PL properties, thus supporting distinct "Write" and "Read" operations.

Table 4.1 lists and compares the current reports on PL-based neuromorphic behaviors. It clearly distinguishes the MHPe@MYE mechanism as material reconfiguration from existing reports, whose overall mechanisms are all based on photophysical processes with "Write-only" synaptic functions.

Table 4.1 Comparison of existing PL-based neuromorphic systems.

	Mechanisms	**Write**	**Read**	**Ref**
MHPe @MYE	material reconfigurations of light-induced and recoverable interface-driven halogen migration	Inducing material variation with altered PL properties	Non-destructive probe by low-energy spike	This work
PA UC	Photophysical process of excited-state population kinetics with energy looping between Tm^{3+} ions near the PA threshold	Pumping electrons from ground states to emissive excited states (*i.e.*, trap, intermediate, or triplet states)	Passive readouts during continuous luminescence decay	122
PersL	Photophysical process of trap-mediated electron trapping/detrapping at defect states, and resultant luminescence decay			123
Triplet ET	Photophysical process of O_2-mediated TTA anti-Stokes UC at triplet states via ISC and ET			124

The separation of "Write" and "Read" operation is widely recognized for its advantages in information processing, such as enhanced data integrity and reduced disturbance during readout.[125,126] Drawing inspiration from existing paradigms, the successful implementation of distinct "Write & Read" functionality in PL-based systems may also lead to functional advancement over previous "Write-only" decay-type systems. Some prospective merits are conceptually illustrated in **Figure 4.19** featuring the following key benefits:

1. Information security through on-demand accessibility

Continuous PL decay in decay-type systems continuously broadcast information globally, creating security risks by information leakage. In contrast, variation-type

systems like MHPe@MYE with “Read” operation requires specific optical triggers to activate current PL states. This prevents data leakage in security-sensitive tasks.

2. Anti-interference through dark PL properties variations

Decay-type systems with continuous post-stimuli signaling may suffer from internal signal interference due to light scattering, reflection, and refraction of decay within the system. In stark contrast, the variation-type avoids this by operating in dark states post-“Write”, ensuring reliable information processing by isolating signals until intentional “Read” excitation.

3. Parallel co-computing enabled by spatiotemporal decoupling

The global signal broadcasting of decay-type phosphors complicates unit integration due to signal overlaps within adjacent phosphors. In contrast, variation-type systems separate the “Write” and “Read” phases. The dark PL properties variations and on-demand “Read” mechanism enable selective readout extraction without external interference.

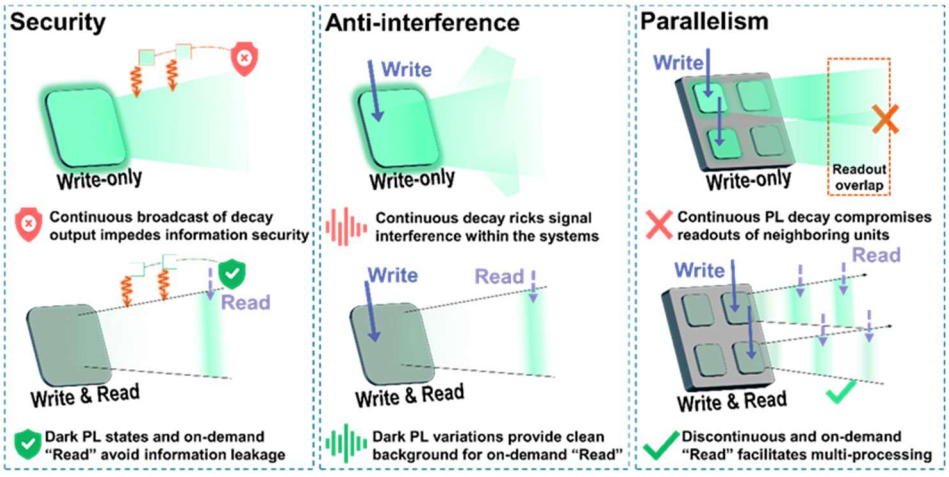

Figure 4.19 Schematic illustrations of the importance of distinct “Read” operations showing potential prospects in information security, anti-interference, and parallel operation.

The above latent advantages have potential placed the variation-type "Write & Read" systems as a more practicable neuromorphic computing paradigms based on PL functions. To further elucidate the advantages of implemented "Read" mechanisms in the developments of PL-based neuromorphic systems, comparison studies were performed to examine the impact of signal interference of "Write-only" counterparts. These experiments aim to demonstrate the critical importance of the "Read" operation in mitigating interference effects, thereby enhancing system reliability and efficiency. A similar PL-based physical reservoir was virtually constructed for SOCOFing fingerprint recognition using a decay-type "Write-only" configuration (tagged as w/o Read) with analogous PL features to MHPe@MYE. This virtual system was compared against the original "Write" and "Read" system (tagged as w/ Read). The impact of interference was investigated under four different scenarios:

1. **Internal interference (Internal)**: A single decay-type unit operating in isolation, where interference was primarily due to internal factors such as light scattering, reflection, and refraction of the continuous decay within the system.
2. **External interference at far-distance (Far)**: Another identical decay-type unit placed at a significant distance from the primary unit, causing minimal signal overlaps between the two continuous decaying signals.
3. **External interference at medium-distance (Med.)**: Another identical decay-type unit placed at a moderate distance, introducing moderate signal overlaps.
4. **External interference placed adjacently (Adj.)**: Another identical decay-type unit placed adjacently, maximizing signal overlaps.

The results revealed that even with minimal internal interference, the accuracy of the decay-type system decreased to 91.7%, compared to the original 94.4% for the system

with a "Read" operation (**Figure 4.20a**). The introduction of external signal overlaps further reduced accuracy, down to 76.4% in the adjacent case. This significant drop in accuracy underscores the vulnerability of decay-type systems to signal interference. In the meantime, the time costs associated with feature-space deviations were examined by counting the number of re-examination events due to feature loss. When the interference drifts PL readouts out of the experimentally acquired PL feature map (*i.e.*, **Figure 4.5** and **Figure 4.6**), it will count as one feature-loss event. As shown in **Figure 4.20b**, the "Write-only" operation led to a notable number of feature-loss events, particularly under external interference conditions at close distances. This results in increased training costs and reduced data quality.

Similar performance degradation was observed when altering the resize value during image preprocessing. At a constant medium distance, even minimal resizing (*e.g.*, 96 × 96) resulted in reduced maximum accuracy (**Figure 4.20c**) and greatly increased resource costs due to feature-loss events (**Figure 4.20d**). These observations highlight the impracticality of deploying multiple decay-type units in adjacent regions and underscore the critical necessity of integrating a distinct "Read" mechanism to enable robust, scalable parallel processing in developing PL-based neuromorphic computing architectures. The above simulation results evidence the advantage of distinct "Read" operations.

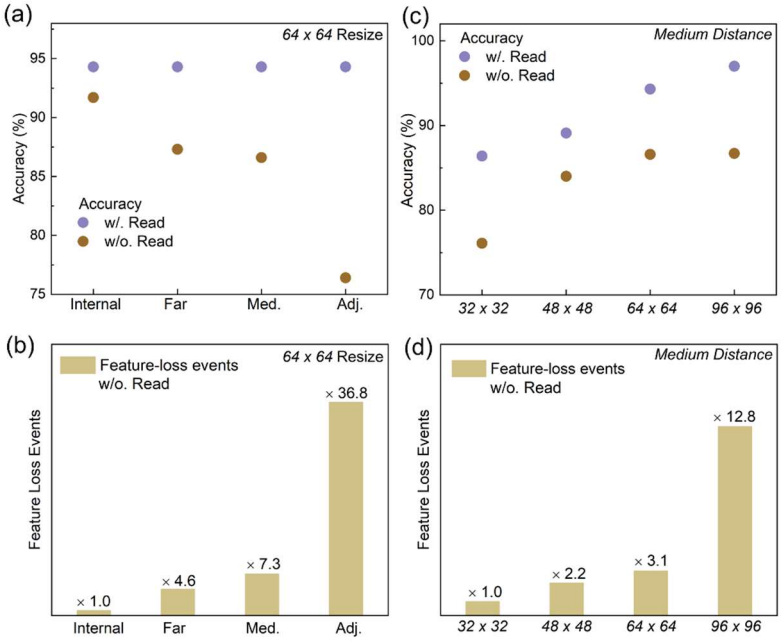

Figure 4.20 Comparison studies of PL-based physical reservoir for fingerprint recognition without distinct "Read" mechanism. (a) Recognition accuracy and (b) amounts of feature-loss events for 4 different scenarios. (c) Recognition accuracy and (d) number of feature-loss events for different image resizing.

4.6 Summary

This showcase of MHPe@MYE's capabilities in data preprocessing presents an innovative alternative to conventional processing methods like normalization and regularization. By effectively managing the intricacies of the SOCOFing fingerprint dataset, the MHPe@MYE physical reservoir secures a comparable performance with conventional electrically functioned devices with high recognition accuracy of 94.4%, further and enabling the development of specialized and efficient network architectures exclusively based on PL functions.

Chapter 5 PL and FE Er-doped HfO_2 Ultrathin Films with High Endurance

5.1 Introduction

The information explosion, from both aspects of quantities and dimensionalities, has spurred a growing demand for electronic materials with extended information freedoms, enhanced processing capabilities, and smaller sizes.[127,128] HfO_2 has long been recognized for its high-k dielectric properties.[51] Notably, a paradigm shift occurred in 2011 with the discovery of FE in Si-doped HfO_2 films.[52] The unique combination of exceptional FE characteristics at ultrathin level and the high compatibility with CMOS technology significantly addresses the bottlenecks of traditional FE materials (such as oxide perovskite and polymer ferroelectrics) in device fabrications, leading to great potential in various electronic devices applications (**Figure 5.1a**).[129-131] The FE phases of HfO_2, such as the *o*-phase, are inherently metastable at room temperature, the stabilization of which can only be achieved by imposing multiple driving factors, including dopants, defects, strains, and rapid annealing.[51] The crucial role of dopants in such phase stabilization has been widely acknowledged.[132-134] Despite the significant progress, several challenges persist and hinder their widespread adoption, particularly the electrical wake-up effect and limited endurance. The wake-up effect of HfO_2 refers to a phenomenon where the polarization strength gradually increases over the initial switching cycles (typically from 10^2 to 10^6 cycles).[135] Such FE films may not perform consistently, which complicates their usage in applications. On the other hand, the

endurance of HfO_2 thin films also remains notably inferior to that of traditional ABO_3-type perovskite ferroelectrics. This limitation arises from the intrinsic fragility of the metastable FE phase in HfO_2, which is highly sensitive to external perturbations and prone to phase instability during repeated polarization switching. Over cycling, the material is susceptible to the accumulation of structural and electronic defects, with oxygen vacancy generation and redistribution playing a central role in the fatigue process. These vacancies can migrate and aggregate under electrical stress, forming conductive filaments and local breakdown pathways. Furthermore, charge trapping at interfaces and within the film can lead to domain pinning, impeding the reversible switching of FE domains and causing a progressive reduction in the remnant polarizations (P_r). The combined effects of defect dynamics and charge trapping ultimately degrade FE performance and limit the endurance of HfO_2 thin films, accounting for their poor fatigue resistance compared to conventional ferroelectrics.

In contrast to the other ferroelectrics, dopants play a crucial role in stabilizing the metastable *Pca2*$_1$ FE *o*-phase HfO_2.[51,136] Recognizing the pivotal role of dopants in addressing these challenges, researchers have intensified many efforts in dopant engineering as the key strategy to improve the FE performance of HfO_2. Continuous efforts have been put in exploring capable dopants beyond the conventional Si:HfO_2 to Zr:HfO_2 (HZO) and Y:HfO_2 (HYO) recipes.[137-143] For instance, the incorporation of excess Hf and Zr in metallic form results in $Hf(Zr)_{1+x}O_2$ thin films stabilized in an alternative FE rhombohedral phase, showing greatly reduced coercive fields and enhanced remanent polarizations that are highly desirable for the low-power applications (**Figure 5.1b**).[139,144] A donor-and-acceptor co-doping strategy is reported to help accomplish an ultrafast FE switching dynamics of the La,Ta:HfO_2 thin films

(**Figure 5.1c**).[145] Notably, Y and La dopants have shown the capability to transcend the thickness limits of *o*-HfO_2.[146,147] HYO, in particular, is reported to possess intrinsic ferroelectricity, as evidenced in both highly crystalline thin films and bulk single crystals.[143,148]

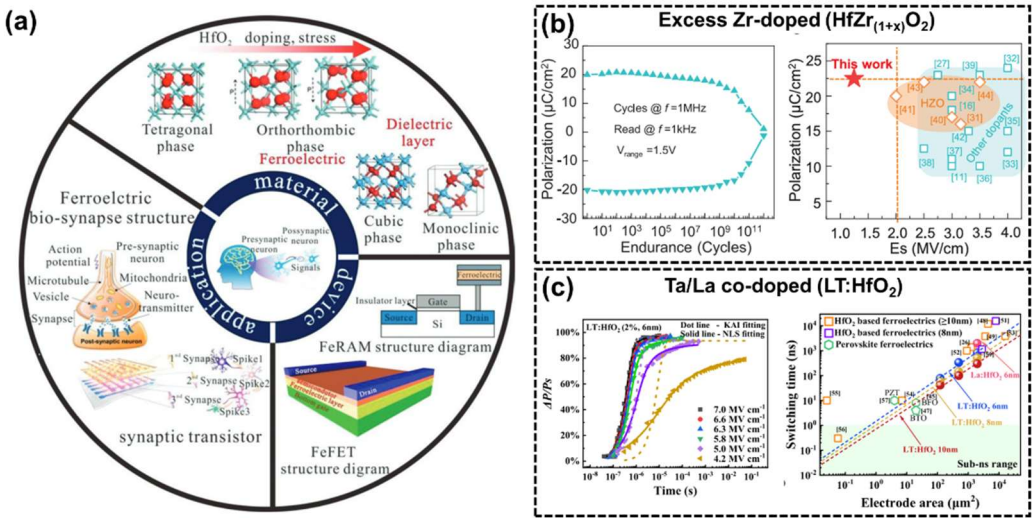

Figure 5.1 (a) Review of FE HfO_2, their utilization in various FE devices, and the related cutting-edge applications. Crucial impact of dopants from various aspects, such as (b) $HfZr_{(1+x)}O_2$ stabilized in alternative FE phase structure,[139] and (c) enhanced polarization switching dynamics in LT:HfO_2.[145]

There, the exploitation of novel dopant candidates has become an imperative and pivotal objective in this research field.[149] Besides these merits, the multifaceted impacts of metal-ion dopants beyond conventional influences on electrical properties await further exploitations.[150] Some Ln are recognized for their abundant energy levels and unique intra-configurational *f-f* transitions, which allows for light absorption and photoemission across a broad spectral range covering UV to NIR regimes. As a representative, Er^{3+} ion can show both visible and NIR photoemissions through the UC and DC pathways, respectively. Such versatile Er^{3+} luminescence has found

applications across diverse fields, rendering their widespread utilizations in telecommunications, optoelectronics, and biomedical applications.[151,152] In our previous work, the interesting coupling effect between PL and ferroelectricity in Er/Yb co-doped BTO films have been previously dem,onstrated.[57] The introductions of optically active Er^{3+} into 2D transition metal dichalcogenide (TMD) semiconductors like MoS_2, WS_2, and ZnSe also hold promises for extending optical functionalities.[153,154] However, the introduction of Er into FE HfO_2 remains an uncharted area of interest. In stark contrast to the above material systems, where Er luminescence is intentionally introduced as an extrinsic guest property into host matrices with pre-existing features (such as ferroelectricity in undoped BTO, or semiconducting characteristics in undoped 2D TMDs), the FE stabilization of HfO_2 critically hinges on appropriate dopants. This situation prompts an intriguing question about how Er will impact the FE property in doped HfO_2.

Leveraging insights from the chemical and physical conformality between Er^{3+} and Y^{3+}, as well as the extensively studied HYO systems with superior ferroelectricity, it is proposed that Er can achieve both objectives within a single type of dopant. In other words, the incorporation of Er itself undertakes a dual role in HfO_2, namely, the stabilization of ferroelectricity and the incorporation of PL property. Here in this work, it is first elucidated that, from a theoretical standpoint, Er can arouse superior dopant effect that suppress the well-studied Y and Zr dopants, resulting in effective stabilization of robust and endurable ferroelectricity by anchoring V_O from non-FE migration; on the other hand, the emergence of localized Er 4*f* states within the HErO host bandgap introduces a distinct optical difference. Experimental verifications were subsequently conducted using epitaxial HErO thin films grown by PLD. The as-

deposited HErO thin films display robust ferroelectricity at various thicknesses (3 to 30 nm). More importantly, it was confirmed that Er-doping has greatly improved the endurance with less than 20% degradation in P_r obtained after over 10^{11} switching cycles measured at 1 MHz. The successful integration of PL properties into HErO film was validated by spectral investigations, offering both NIR and visible photoemissions under 980 nm excitation through the DC and UC processes, respectively.

This study paves the way toward intrinsically expanded optical freedom of FE HfO_2 thin films spanning wide spectral windows, and significantly enhanced opening up new possibilities for achieving HfO_2-based multi-mode and multifunctional devices with high endurance as illustratively summarized in **Figure 5.2**.

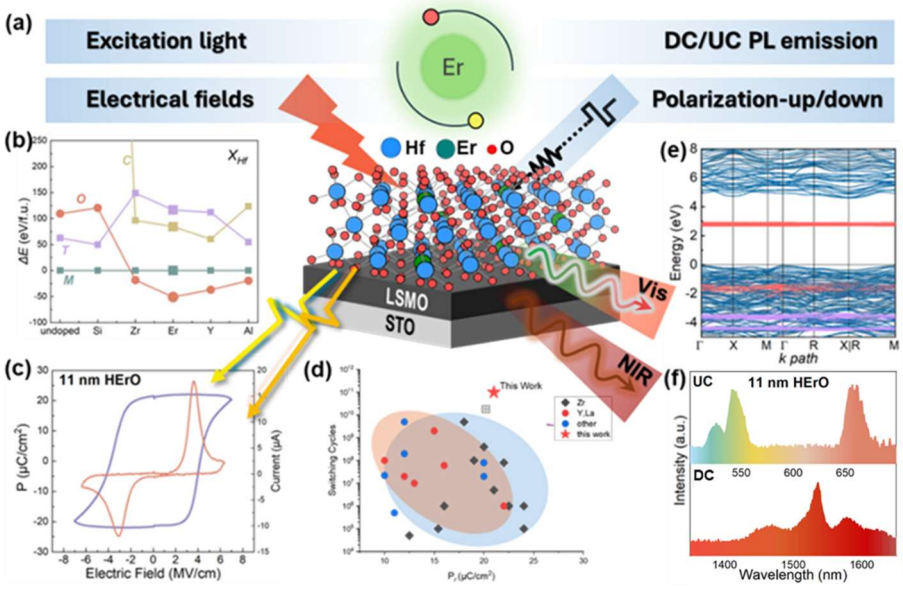

Figure 5.2 Schematic of the research design and key results in this chapter. (a) Illustration of the FE and PL dual-mode HErO thin film. (b) DFT Simulated phase energy of HfO_2 in diffenrent phase. (c) The PUND test of HErO. (d) Benchmarking FE properties of HErO against other dopants. (e) DFT simulation on introctin of the optical-active localized Er 4*f* states. (f) Experimental measured UC and DC PL from HErO at ultrathin films (~11 nm).

5.2 Theoretical insights into Er-doping effects

This study first examines the Er-doping effect in HfO_2 *via* theoretical simulations. The crystal structure of FE *Pca2₁ o*-HfO_2 is shown in **Figure 5.3a,** which is one of the metastable phases among the numerous HfO_2 polymorphs. In view of the HfO_2 phase diagram, the effects of dopants are commonly determined by three aspects: valency, ionic radius, and electronegativity.[155] These three features collectively affect the coordination number (CN) of hafnia and their bonding characteristics to oxygen, which are crucial for stabilizing *o*-HfO_2.[156] It is widely argued theoretically that trivalent dopants with large ionic radius and low electronegativity are superior choices, which favors the Ln series as ideal dopant candidates. Because of lanthanide contraction, all the Ln elements, together with the nearby Y, Hf, and Zr elements, possess similar chemical and physical properties, including ionic radii (**Figure 5.3b**) and electronegativity. While Zr has emerged as the most common dopants in both academic and industrial perspective, Y^{3+} also garnered experimental and theoretical favors in the stabilization of ferroelectricity of HfO_2.[155] In the meantime, Er and Y are acknowledged for their capability to form solid solutions in many material systems.[157-159] Consequently, Er may serve as an analogous substitute for Y doping in the case of FE HfO_2.

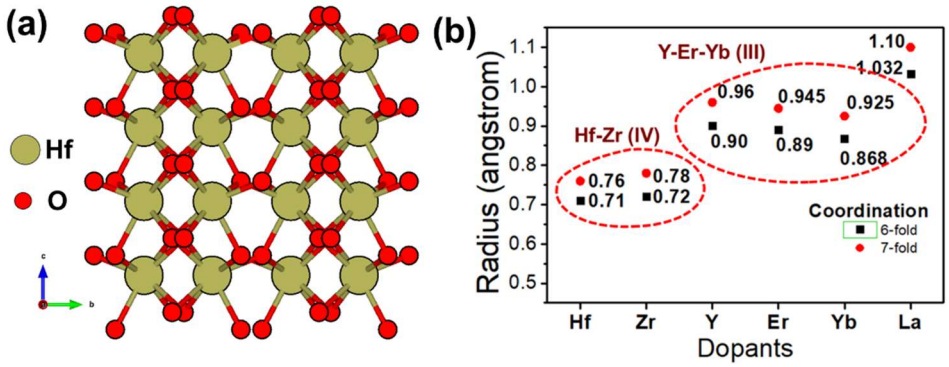

Figure 5.3 (a) The crystal structure of FE o-HfO_2, the displacive oxygen layer and the fixed oxygen layer during FE polarization are painted in green and blue, respectively. (b) The ionic radius of candidate dopants at 6-fold (for *m*-phase) and 7-fold (for *o*-phase) CN including Yb, Er, Y, and Zr against the pristine Hf.

To offer theoretical insights into this point, DFT simulations were first carried out for a systematic comparison between the dopant effects of Er on FE *o*-HfO_2 with reference to the well-studied Zr and Y. The phase energies of HfO_2 doped with different metal ions were first compared. **Figure 5.4** compares the phase energies of different non-FE phases and FE *o*-phase of HfO_2 doped with various dopants, including Si (12.5 a.t.%), Zr (50 a.t.%), Er (12.5 a.t.%), Y (12.5 a.t.%), and Al (12.5 a.t.%). The total energy was normalized based on the non-FE *m*-phase, which is thermodynamically the most stable phase of undoped HfO_2 at room temperature. It clearly shows that Er-doping leads to lower gap between FE *o*-phase and non-FE monoclinic (*m*), cubic (*c*), and tetragonal(*t*)-phase, which secure the fundamental of a more robust phase stability during electrical cycling.

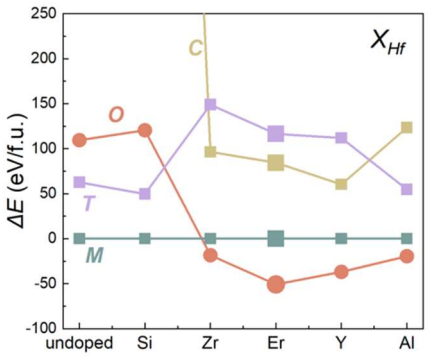

Figure 5.4 Phase energies of FE HfO_2 doped with various dopants normalized to the total energies of non-FE *m*-phase, correspondingly.

The FE properties of HErO were then studied in terms of P_r from the theoretical aspects by Berry phase method using HYO as a reference, which is current holder of record-high P_r by PLD.[148] In specific, 10 intermediate states were established by the nudged elastic band (NEB) method between the pristine *Pca2₁* polarization-down configuration and the centrosymmetric *Pbcm* states. The plots of the calculated polarization along the *z* axis (P_z) can be clearly categorized into three parallel branches (**Figure 5.5a** and **5.5b**), indicating a spontaneous polarization of 62.4 μC/cm^2 and 60.9 μC/cm^2 for HErO and HYO, respectively. No obvious spontaneous polarization can be found along the *x* and *y* axis of both the two models. The fitted spontaneous polarization of the undoped HfO_2 is relatively smaller (**Figure 5.5c**, 50.1 μC/cm^2). The results indicate that Er has a comparably positive contribution to the polarization of HfO_2 like Y-doping does. As shown in the inset atomic scheme in **Figure 5.5d**, by extending the oxygen motion across the intermediate states toward the polarization-up *Pca2₁* states, the corresponding energy barrier of the polarization switching process can be calculated.[160] The simulation results in **Figure 5.5d** show that HErO needs to overcome a potential barrier of ~66.1 meV/atom while crossing the centrosymmetric *Pbcm* state.

The value is comparable to that of the HYO counterpart (~66.8 meV/atom), and significantly lower than the undoped FE HfO_2 scenario (~87.4 meV/atom). These results indicate that the Er and Y dopants can facilitate the FE switching of HfO_2 by lowering the energy barrier to a similar extent from the theoretical perspective. The total energies of the polarization-down states to their corresponding up states with the same displacement slightly deviates, which might cause further phase degradation to the anti-polar phase as discussed elsewhere.[160]

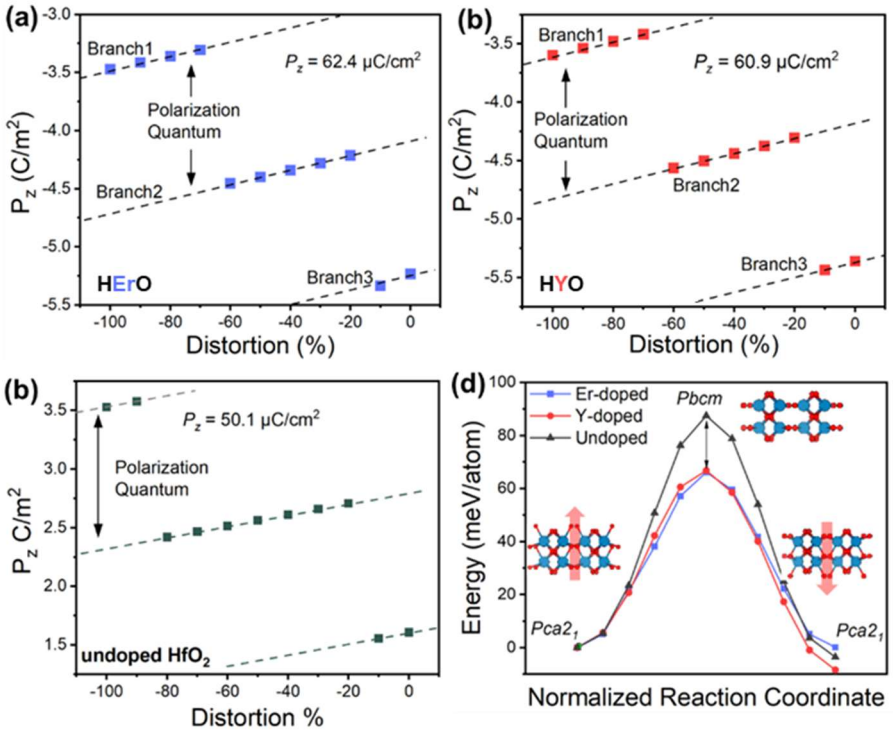

Figure 5.5. Calculated P_z of (b) HErO, (c) HYO, and (d) undoped FE HfO_2. (d) The energy landscapes of the entire polarization-switching process of HErO, HYO, and undoped HfO_2, the inset shows the crystal structures of the initial polarization-down $Pca2_1$, the centrosymmetric *Pbcm*, and the final polarization-up $Pca2_1$ states.

The electrical switching endurance of FE HfO_2 is critically influenced by the migration behavior of V_O. V_O is generally present in the HfO_2 thin films, which is also evidenced to be beneficial for the stabilization of FE *o*-phase. However, it is argued that the breakdown and fatigue of HfO_2 during electrical cycling is majorly related to the motion of neutral V_O and positively charged V_O ($V_O^{\bullet\bullet}$) oxygen defects, respectively.[161] In specific, neural V_O can be generated upon electrical cycling, which would easily migrate to form percolation paths or filaments to form conductive filaments, eventually resulting in the hard dielectric breakdown. On the other hand, $V_O^{\bullet\bullet}$ tend to be trapped at domain boundaries, which induce domain pinning that leads to gradual polarization fatigue without significant increase in leakage.

To quantitatively assess how dopant interactions affect endurance, the study establishes migration models that explicitly consider the spatial relationship between V_O and metal-ion dopant ions. Although the microscopic origin of ferroelectricity in *o*-HfO_2 is still under debate, the basic polarization switching process is arbitrarily driven by the displacements of oxygen ions along the $\pm z$ direction in the lattice.[162,163] This approach allows for a direct evaluation of how the presence and proximity of dopants modulate the migration barrier of V_O, which is a key factor in determining vacancy mobility that could lead to FE fatigue or dielectric breakdown. In specific, three representative diffusion paths for $V_O^{\bullet\bullet}$ were analyzed as illustrated in **Figure 5.6a**, which are O1 to O1, O2 to O2, and O1 to O2 located at either far from or close to the substitution site, respectively. The migration barriers were calculated using NEB method for undoped HfO_2, HErO, and the most conventional HZO. The resultant energy landscapes in **Figure 5.6b**, constructed on the total energies of different images during the migration, clearly demonstrate that Er doping can significantly increase the

migration barrier of $V_O^{\bullet\bullet}$ happened adjacently (with barrier of >3.0 eV) compared to the case where $V_O^{\bullet\bullet}$ migration is away from the coordination shell of Er (~2.2 eV). Notably, the energy barrier of the far Er- $V_O^{\bullet\bullet}$ case is the same as the undoped scenario. In sharp contrast, Zr-doping shows no restriction on $V_O^{\bullet\bullet}$, as the migration barrier of adjacent $V_O^{\bullet\bullet}$ migration process even diminishes slightly (~2.1 eV).

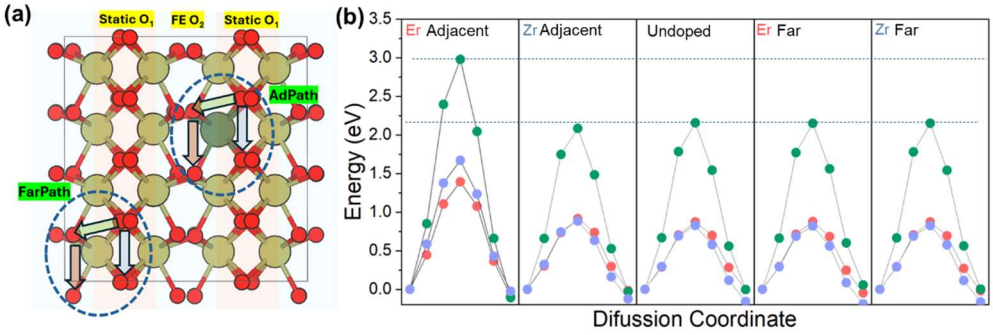

Figure 5.6 (a) Diffusion paths of $V_O^{\bullet\bullet}$ in metal-ion-doped FE HfO_2. The red, blue and green arrow indicates the migration of $V_O^{\bullet\bullet}$ from O1 to O1, from O1 to O2, and from O1 to O2, respectively. The cycled area indicates the $V_O^{\bullet\bullet}$ migration process close to the metal-ion dopants (tagged as Adjacent) or far from the metal-ion dopants (tagged as Far). (b) The NEB energy landscape of the $V_O^{\bullet\bullet}$ migration process.

Building upon the ability of Er to anchor adjacent $V_O^{\bullet\bullet}$ migration, the distribution of $V_O^{\bullet\bullet}$ is further studied. Generally, opposite charged defects tend to aggregate in the lattice to achieve the lowest total energies due to electrostatic and elastic interactions.[164] Therefore, the defect binding energies of Er_{Hf}^{-} and $V_O^{\bullet\bullet}$ ($E_b(Er_{Hf}^{-1} + V_O^{2+})$) at different configurations were investigated:

$$E_b(Er_{Hf}^{-1} + V_O^{2+}) = E_{tot}(Er_{Hf}^{-1} + V_O^{2+}) + E_{tot}(perfect) - E_{tot}(Er_{Hf}^{-1}) - E_{tot}(V_O^{2+})$$

where $E_{\mathrm{tot}}(\mathrm{Er_{Hf}}^{-1} + V_{\mathrm{O}}^{2+})$, $E_{\mathrm{tot}}(perfect)$, $E_{\mathrm{tot}}(\mathrm{Er_{Hf}}^{-1})$, and $E_{\mathrm{tot}}(V_{\mathrm{O}}^{2+})$ is the total energies of the lattice with both defects, the perfect FE HfO_2, the Er-doped HfO_2, and the $V_O^{\bullet\bullet}$-contained HfO_2 lattice, respectively. The Er_{Hf}^{-}-$V_O^{\bullet\bullet}$-distance-dependent E_b is plotted in **Figure 5.7**. It clearly shows that $V_O^{\bullet\bullet}$ favors incorporation in the first coordination shell of Er dopants, leading to a stable binding energy of ~0.25 eV. As the $V_O^{\bullet\bullet}$ was set away from Er, the binding energy also increases, indicating the configuration become less stable. The thermodynamically stable configuration of adjacent Er_{Hf}^{-} and $V_O^{\bullet\bullet}$ prompt the merits of Er to further stabilize the $V_O^{\bullet\bullet}$ migration, which is absent in the main-stream HZO counterpart. The above results collectively evidence the attractive interaction between Er dopants and $V_O^{\bullet\bullet}$ that can restrict vacancy movement and thereby contributes to improved endurance in HErO.

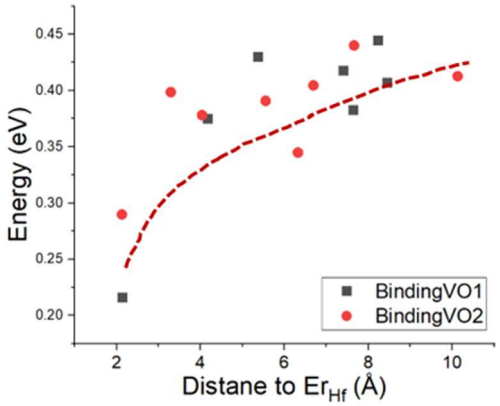

Figure 5.7 Binding energy (E_b) as a function of distance between Er and V_O.

Besides the superb Er-doping effects that can potentially stabilize a high-endurance ferroelectricity, another distinguishable difference among Er and other dopants lies in the extra Er 4*f* electronic states and the relevant electronic transitions. Screened by the outer-shell *s*, *p*, and *d* electrons, the 4*f* electrons of Er barely participate in any mixing or bonding interactions with the coordinating atoms. Consequently, Er^{3+}

(electron configuration [Xe]$4f^{11}$) shows high conformality to Y^{3+} ([Kr]). Therefore, a comparison study was then carried out using HYO as the reference. As compared in **Figure 5.8a-d,** The electronic band structures and density of states (DOS) of HErO and HYO are almost identical, despite that sharp difference can be seen from the emerging non-bonding Er *f* states with localized and non-dispersive features located within the large bandgap of HErO. It offers sufficient space for intra-configurational *f-f* electronic transitions among Er^{3+} terms during both the UC and DC PL process. These results demonstrate an intriguing juxtaposition of certain shared FE characteristics and distinct optical disparities between HErO and HYO. In other words, Er luminescence has become an intrinsic property of FE HErO. Such optical upgrades of HErO compared to HYO hold great promises in extending the functionality of FE HfO_2 thin films and their devices.

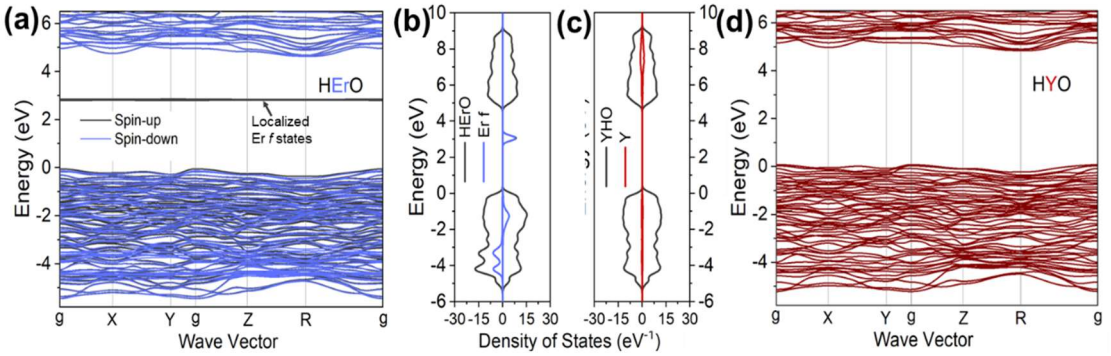

Figure 5.8 A comparison between the calculated electronic band structures and projected DOS between (a)(b) HErO and (c)(d) HYO.

5.3 Structural characterizations of HErO thin films

After evaluating the theoretical availability of two-way Er-doping effects in HfO_2, experimental verifications were carried out using PLD-grown epitaxial HErO thin films on LSMO-buffered STO(001) substrates to demonstrate the dual optical and FE properties within a single system of HErO. Comprehensive XRD analyses were carried out for investigation of the crystal structures of the HErO thin films. **Figure 5.9a** shows the standard 2θ-ω scans of the as-deposited HErO/LSMO/STO films in the range of 3 - 30 nm. The 2θ peak at around 30° can be assigned to the (111) plane of *o*-HfO_2. The slight deviation from the standard 2θ value of 30.5° is originated from the doping effect of Er with larger ionic radius (0.95 Å with 7-fold coordination, for Hf sites in $Pca2_1$ *o*-HfO_2) compared to Hf (0.76 Å with 7-fold coordination). The compressive in-plane strain also holds responsible for the elongated plane spacing of (111), especially when the film thickness approaches down to 3 nm.[144] The effects of Y doping (0.96 Å with 7-fold coordination) are similar according to present literature.[142] Crystal truncation rods of Laue oscillations can be viewed alongside the HErO and LSMO 2θ peaks over the thickness series, demonstrating the generally good crystalline and interface quality. A slight monoclinic impurity accompanies the growth of *o*-HErO when film thickness further increases to ~30 nm. The 11-nm thick HErO was selected as a representative for further detailed crystal structure characterizations. The ω rocking curve of LSMO(001) (2θ = 23.0°, **Figure 5.9b**) shows a predominate sharp peak with fwhm of 0.06°, indicating the high quality of the LSMO buffer layer. Consequently, the ω rocking curve aiming at *o*-HfO_2(111) (2θ = 30°, **Figure 5.9c**) give a classic combination of a sharp peak (fwhm is 0.16°) sitting on a much broader peak, which can be assigned

to the high-crystallinity and low-crystallinity parts of the epitaxial HfO_2 film, respectively.[148]

The relatively weak intensity for the bottom broad peak indicates a relatively high quality of the as-deposited HErO thin film.[148] The thickness of the above thin films was determined by fitting of XRR curves, as shown in **Figure 5.9d.**[165] The fitted curve (black lines) match well with the measured data, while the clear oscillations in the XRR curve resulted from the various HErO and ~50 nm LSMO layers indicate the smooth interfaces and surfaces with margin roughness. Furthermore, azimuthal φ scans were performed to confirm the epitaxy relationship among the HErO and LSMO epitaxial layers and the STO substrates. The classic cube-on-cube epitaxial growing mode of LSMO(001) on STO(001) can be first confirmed by the 4-fold φ peaks of LSMO(111) (2θ = 40.2°, χ= 55°), with identical periodicity to those of the STO(001) substrates (**Figure 5.9e**). Moreover, aiming at the (-111) plane of *o*-HfO_2 (2θ= ~30.2°, χ= ~71°), a set of 12-fold peaks can be observed that corresponds well to the in-plane epitaxial variant of *o*-HfO_2(111) with 3-fold symmetry growing onto LSMO(001)/STO(001) with 4-fold symmetry.

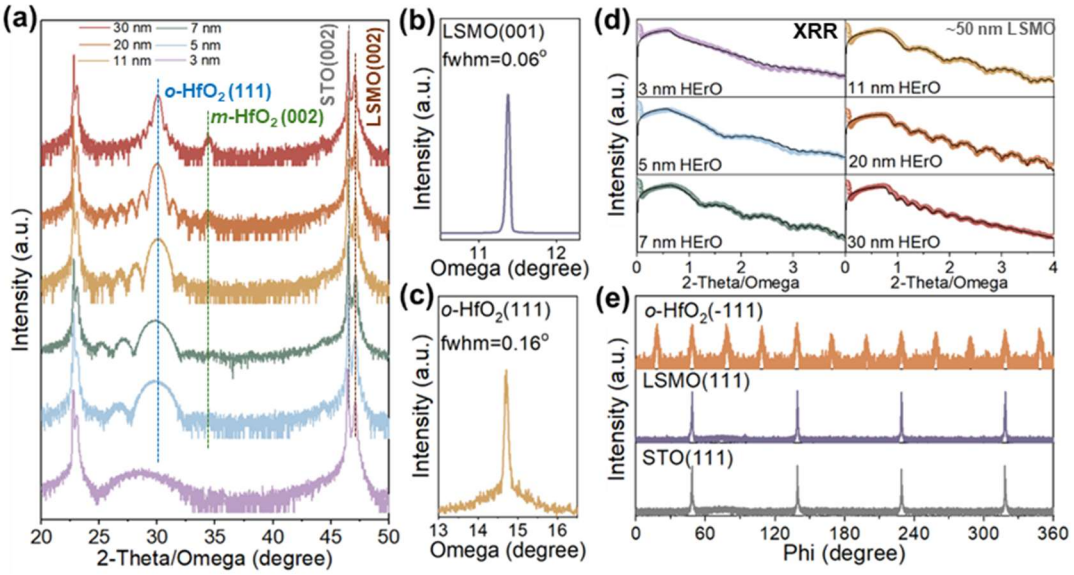

Figure 5.9. (a) the XRD 2θ-ω scan of HErO/LSMO/STO(001) thin films at various thickness, and the rocking curves of (111) plane in (b) LSMO and (c) 11-nm-thick HErO. (d) The XRR and fitting results of the HErO/LSMO/STO(001) thin films. (e) The azimuthal φ scan results of the 11-nm-thick HErO/LSMO/STO(001) thin film at χ = 71°.

However, owing to the highly similar crystal structures of the HfO_2 polymorphs, it is worth noticing that the (111) plane of cubic *Fm-3m* HfO_2 also locates at around 2θ = ~30°, and the interplanar angle χ between *c*-phase (111) and (-111) is ~71° as well. Before the emergence of ferroelectricity, doped HfO_2 films, such as HYO, have also been vastly researched in terms of their dielectric properties, alternatively facilitating the stabilization of high-*k* *c*- and *t*-HfO_2.[166] Therefore, distinguishing the XRD profiles between the high-*k* and FE HfO_2 films often raise ambiguities. In the case of HErO, using the well-known hypersensitive nature of Er PL properties, the misleading *c*-phase (111), as well as the less ambiguous *t*-phase (011), can be easily ruled out by analyzing the spectral features. Such contributions of Er PL to the phase confirmation will be

discussed later in **Chapter 5.4**, whereas the more common way of XRD analyses was first performed to determine the uncertain HfO_2 phases. **Figure 5.10a** shows the 2θ-ω scans featuring the pseudo cubic{002} ($\{002\}_{pc}$) plane of *o*-HfO_2 at different φ angles as specified by φ scan. The different has leads to obviously broadened peaks that are different from the single (002) peak of cubic HfO_2.[148] In addition, the rhombohedral distortion of the $\{111\}_{pc}$ planes is also a key feature for epitaxial *o*-HfO_2, since most of the other polymorphs of HfO_2 each possesses the same *d*-spacing for all {111} planes.[167] As shown in **Figure 5.10b**, the three tilted $\{111\}_{pc}$ diffraction peaks of the as-deposited 11-nm-thick HErO, averaged over four domains of LSMO(001)/STO(001), all uniformly located at 30.5°. A 0.63° difference between these $\{111\}_{pc}$ and the out-of-plane HErO(111) peaks was observed, evidencing the presence of a distinguished rhombohedral distortion. Finally, based on the above results, the epitaxial relationship of the as-grown HErO thin films can be verified as *o*-HfO_2[111]//LSMO[001]//STO[001] for the out-of-plane and *o*-HfO_2(-111)// LSMO(111)//STO(111) for the in-plane orientations, respectively. Notably, identical φ-scan periodic features can be observed across different thicknesses with on signals of other symmetry (**Figure 5.11**), suggesting a consistent growth mode and epitaxial orientation for HErO on LSMO/STO.

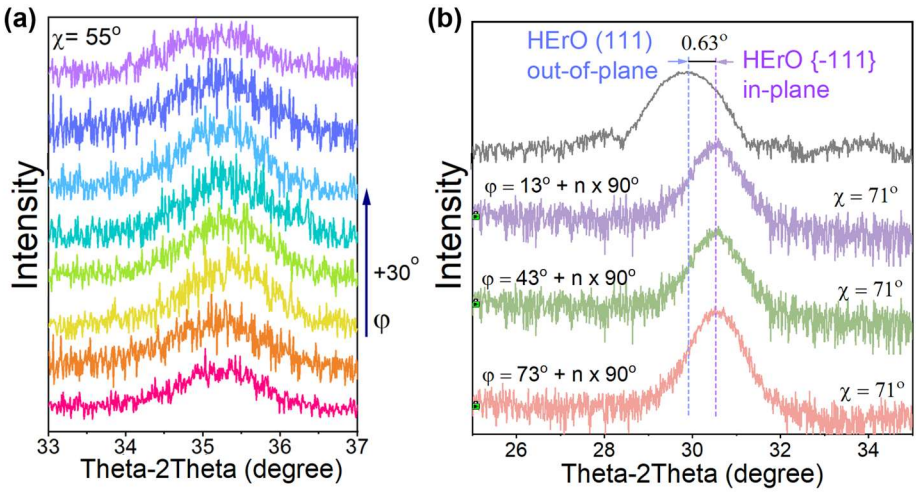

Figure 5.10. (a) XRD 2θ-ω scans around the $\{002\}_{pc}$ planes of HErO at various φ angles. (b) A comparison between the XRD of in-plane and out-of-plane $\{111\}_{pc}$ planes.

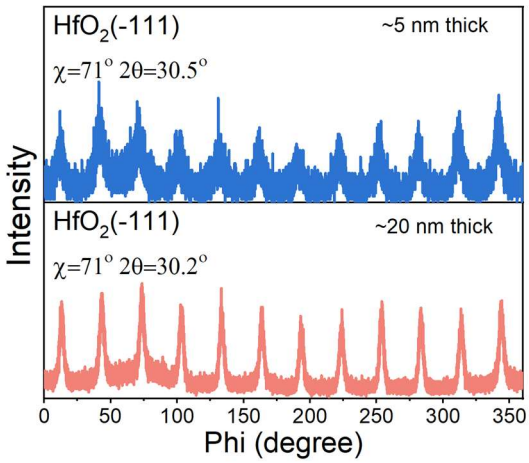

Figure 5.11. φ scans aiming at HErO (-111) with different thickness.

CS-STEM images were then recorded to provide the microscopic view of the 11-nm HErO thin film. The low-magnification HAADF-STEM image clearly shows the multilayer layout of the HErO/LSMO/STO(001) thin films with smooth interfaces (**Figure 5.12a**), where the measured film thickness corresponds well to the fitted XRR fitting results. The different chemical compositions of the multiple layers can be

represented clearly by the EDX mapping images based on **Figure 5.12a**. It was found that the elements Ef (**Figure 5.12b**), Hr (**Figure 5.12c**) in HErO, Mn (**Figure 5.12d**) in LSMO, and Sr (**Figure 5.12e**) and Ti (**Figure 5.12f)** in STO, all distributed evenly over the corresponding layer. Such uniform allocation suggests that the Er dopants have been homogenously introduced into HfO_2.

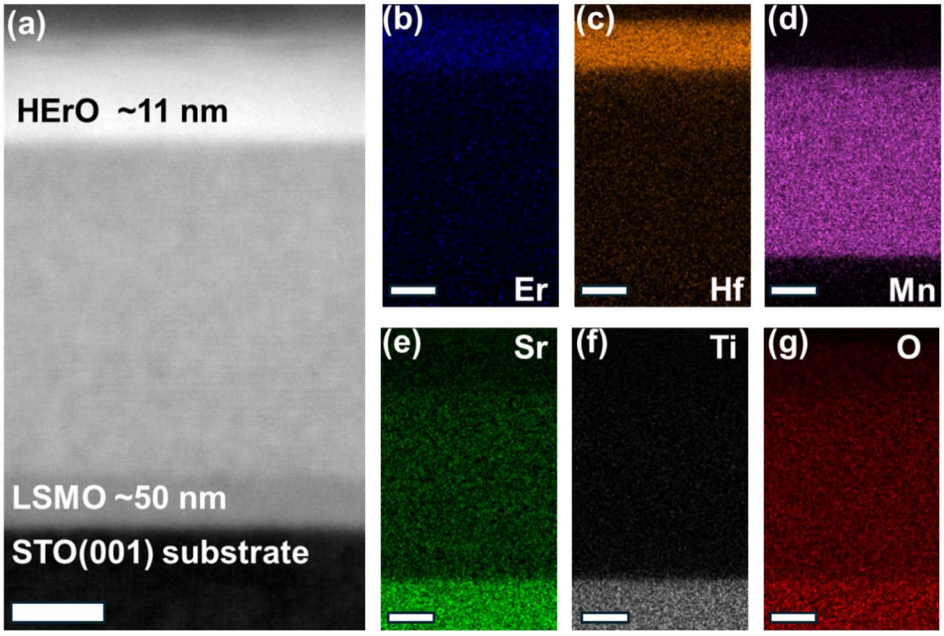

Figure 5.12. (a) Low-magnitude HAADF-STEM and the corresponding EDX mapping of (c) Er, (c) Hf, (d) Mn, (e) Sr, (f) Ti, (g) O in the 11-nm-thick HErO/LSMO/STO(001) thin film. The white bar indicates 10 nm.

The EDX spectra and the fitted elements compositions of the selection area are presented in **Figure 5.13**, respectively, confirming the actual Er-doping ratio (6.91 a.t.%) that closely matches the nominal ratio (7 a.t.%) in the ceramic target. This provides strong evidence for the near-stoichiometric growth of HErO films by PLD. Large-area high-resolution STEM images, as shown in **Figure 5.14**, further reveal the high crystalline quality and uniformity of the two epitaxial layers. Both the

HErO/LSMO and LSMO/STO interfaces can be clearly resolved, exhibiting atomically sharp and smooth boundaries over a wide field of view. The well-ordered atomic arrangements across the interfaces highlight the excellent epitaxial relationship and structural integrity of the heterostructure. In the meantime, well-ordered atomic arrangements are maintained across the large area, with no obvious domains or secondary phases observed, highlighting the high-quality epitaxial relationship in the as-grown HErO/LSMO/STO thin films.

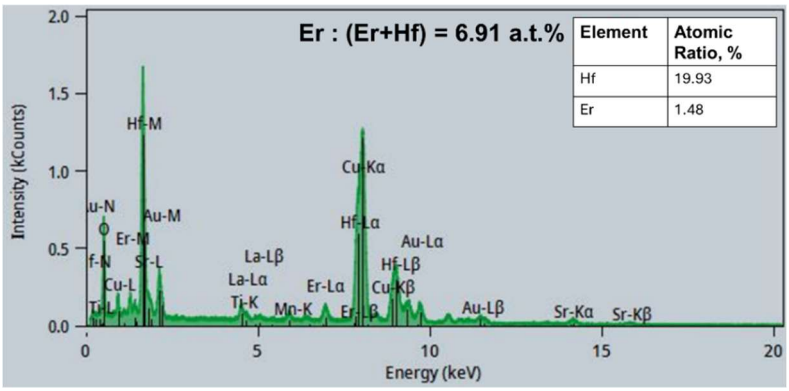

Figure 5.13. EDX spectra selected on the HErO layer, inset shows the atomic fraction of HErO in the thin film.

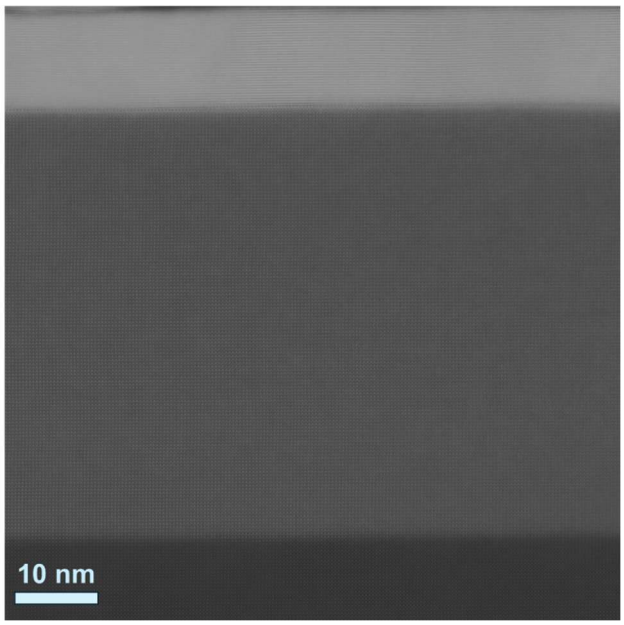

Figure 5.14 The HErO/LSMO/STO epitaxial thin films at the large field of view.

The iDPC- and HAADF-STEM image focused on the HErO/LSMO interfaces was shown in **Figure 5.15a**, featuring a continuous HErO layer growing onto the LSMO layer. As labelled in the figure, the clear crystal plane spacing of 3.0 Å and 3.9 Å match well to the standard data of *o*-HfO_2(111) and LSMO(001), respectively. Furthermore, as demonstrated in **Figure 5.15b,** the zoomed iDPC-STEM image shows a clearer atomic layout in HErO. Notably, the light element O can also be observed from the image as tagged in red. The *o*-phase HfO_2 crystal structure viewed along the [111] direction is then superposed onto the atomic layout (**Figure 5.15b**), showing the perfect matching of both Hf/Er and O in the images. However, further distinguishing Er dopants from Hf atoms remains challenging due to their similar physical and chemical properties. In particular, the close atomic numbers and comparable ionic radii of Hf and Er result in minimal contrast between the two elements in both ADF and DPC STEM imaging modes.[168] As a result, direct visualization or differentiation of Er substitution at Hf sites is not feasible using these techniques.

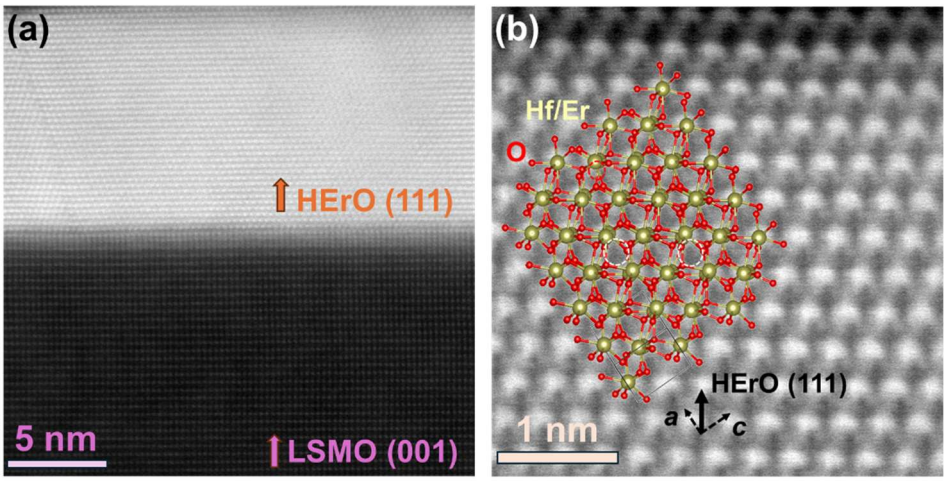

Figure 5.15 iDPC and HAADF STEM images of (a) interfaces between HErO/LSMO layer and (b) atomic layouts of Hf/Er and O as superposed by the crystal structure.

The overall uniformity of Er incorporation with similar chemical environments into Hf sites is further supported by XPS analysis. As shown in **Figure 5.16**, the XPS signal in the range of 168-170 eV can be well deconvoluted into two distinct peaks corresponding to Er $4d_{3/2}$ and $4d_{5/2}$, which is consistent with the expected spin-orbit splitting for Er in an oxide matrix.[169,170] The absence of additional peaks or significant peak broadening indicates that Er ions are predominantly occupying a single chemical site within the HfO_2 lattice.

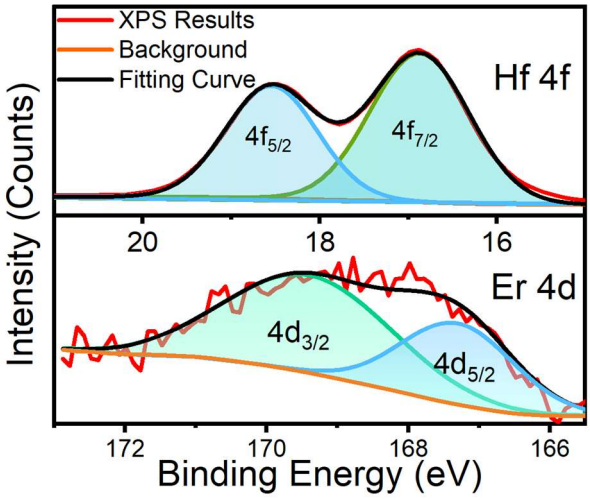

Figure 5.16 XPS spectra of Hf 4f and Er 4d in 11-nm-thick HErO.

Collectively, the above structural characterizations evidence the high-quality and epitaxial growth of HErO and LSMO on STO(001) by PLD, which secures the foundation of following optical and electrical measurements as discussed below.

5.4 UC and DC PL in HErO thin films

In sharp contrast to existing FE doped HfO_2 systems, Er^{3+} ions exhibit distinct energy levels available for light conversion through multiple pathways.[153,171] They can effectively promote an intriguing PL property alongside the robust ferroelectricity of HErO. As illustrated in the energy level profiles in **Figure 5.17a**, after absorbing one 980 nm photon, Er^{3+} can reach the $^4I_{11/2}$ excited states through the GSA process. Subsequently, it will relax to the lowest excited states ($^4I_{13/2}$) following the kasha's rule, resulting in the DC NIR emission originated from the $^4I_{13/2} \rightarrow {}^4I_{15/2}$ transitions. Alternatively, the sequential absorption of another 980 nm photons at the $^4I_{11/2}$ states can lead to further excitation to the higher $^4F_{7/2}$ level, namely the ESA process.[153] ESA leads to multiple UC emission peaks in the visible range, ascribing to transitions from $^2H_{11/2}$, $^2S_{3/2}$, and $^4F_{9/2}$ excited states to $^4I_{15/2}$ ground state, respectively.

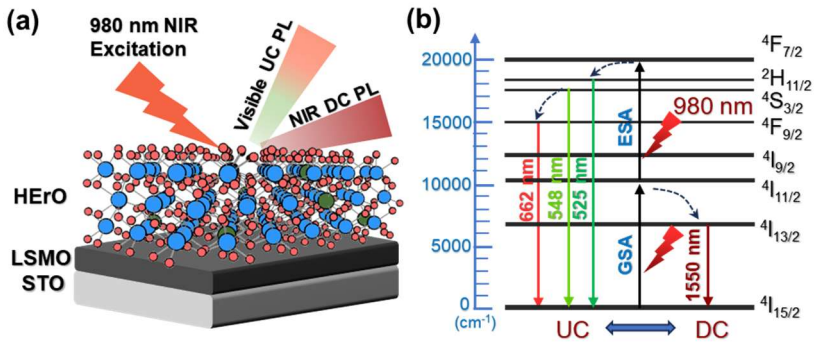

Figure 5.17. (a) Schematic of the PL properties of epitaxial HErO/LSMO/STO thin films. (b) The energy level profile of Er^{3+}, instructing the UC and DC transition pathways.

The PL spectra of the prepared ~10 nm HErO film were then recorded under the focused 980 nm laser excitation. Clear green ($^2H_{11/2} \rightarrow {}^4I_{15/2}$, $^2S_{3/2} \rightarrow {}^4I_{15/2}$) and red ($^4F_{9/2} \rightarrow {}^4I_{15/2}$) UC PL peaks can be observed in the visible range as shown in the upper spectrum of **Figure 5.18**. The PL emission spectrum recorded in the NIR region features a single broad peak ranging from 1450 nm to 1625 nm, originating from Er^{3+} $^4I_{13/2} \rightarrow {}^4I_{15/2}$ transition of the DC PL pathway (lower of **Figure 5.18**). The PL studies evidence the installation of optical interactivity into HErO in both the visible and NIR regimes.

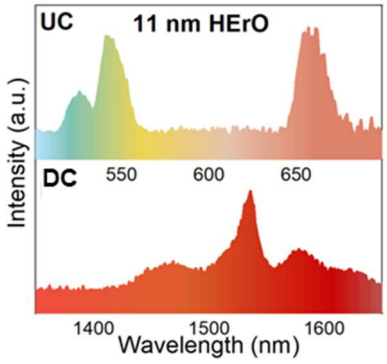

Figure 5.18 The UC (upper) and DC (lower) PL spectrum of the 11-nm HErO under 980 nm excitation.

The excitation-power-dependent PL emission spectra were then recorded by both UC (**Figure 5.19a**) and DC (**Figure 5.19b**) under 980 nm excitation, showing the stable PL features. To further confirm whether the excitation mechanism involves single-photon absorption or multi-photon UC, the logarithmic PL emission intensity was plotted against the logarithmic excitation power density, where the slope of the linear fit reveals the number of photons involved in the PL process.[153] A slope close to 1 indicates a linear single-photon process, whereas a slope near 2 suggests a two-photon UC mechanism involving sequential energy absorption. As plotted in **Figure 5.19c**, the

slopes of the $^2H_{11/2} \rightarrow {}^4I_{15/2}$ (I_{521}), $^2S_{3/2} \rightarrow {}^4I_{15/2}$ (I_{534}) and $^4F_{9/2} \rightarrow {}^4I_{15/2}$ (I_{650}) were all close to 2 with clear linear relationship throughout various excitation powers, indicating the two-photon nature of the PL process. In sharp contrast, linear fitting of the DC $^4I_{13/2} \rightarrow {}^4I_{15/2}$ (I_{1534}) series gives a smaller slope (1.28) close to 1, evidencing the distinct single-photon PL mechanisms.

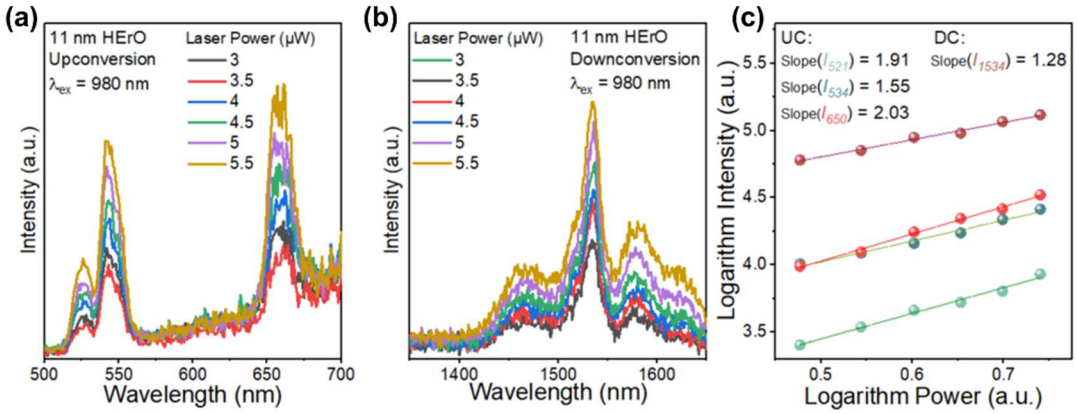

Figure 5.19 (a) Excitation-power-dependent UC PL and (b) Excitation-power-dependent DC PL in HErO. (c) The plotted excitation-power-dependent PL intensity for investigating the photon conversion amounts in the PL process.

The PL decay of the two PL processes is also investigated. **Figure 5.20** shows the measured decay curve and corresponding fitting results of each peak. Although the Er f-f transition is both parity- and spin-forbidden, both the green and red UC emission of HErO exhibits fast PL decay with short lifetimes of ~300 μs (**Figure 5.20a** and **b**). The reason can be assigned to the evaluated PL quenching brought by high doping concentrations and small energy-level gaps.[172] the UC lifetime reduction is attributed to the enhanced non-radiative decay at high doping concentrations in HErO (7 a.t.%). In addition, the energy gap among excited Er^{3+} energy states is relatively small. For instance, **Figure 5.17b** shows that the gap between $^4S_{3/2}$, $^2H_{11/2}$ is only 1000 cm^{-1}. Such

small gaps facilitate an even stronger multi-phonon relaxation, especially in oxide hosts like HfO_2 with relatively higher phonon energies than fluoride counterparts. Additionally, UC processes exhibit higher susceptibility to concentration quenching via cross-relaxation among neighboring Er^{3+} ions, which further shortens the measured PL decay lifetime. Conversely, the DC pathway at 1534 nm from $^4I_{13/2} \rightarrow {}^4I_{15/2}$ (**Figure 5.20c**) involve lower-energy states with larger energy gaps (~6000 cm^{-1}, as shown in **Figure 5.17b**), minimizing multi-phonon relaxation and allowing radiative transitions to dominate, resulting in longer lifetimes.

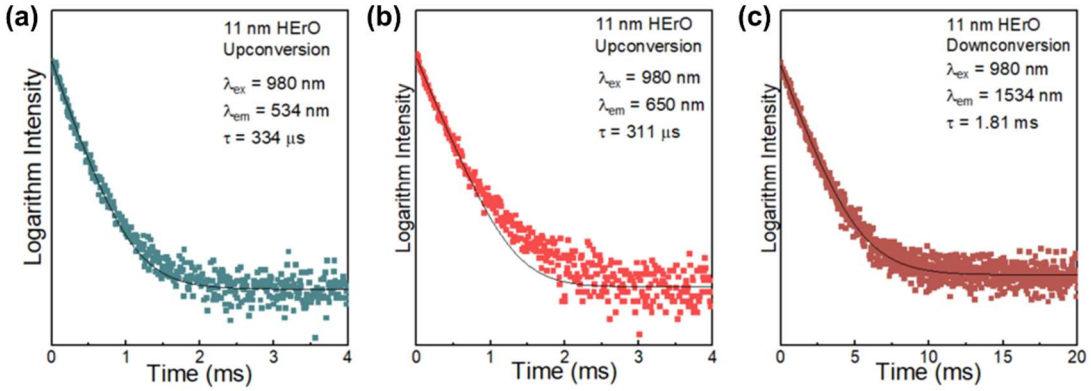

Figure 5.20 PL decay and the corresponding fitting curve of (a) $^2S_{3/2} \rightarrow {}^4I_{15/2}$ (I_{534}) and (b) $^4F_{9/2} \rightarrow {}^4I_{15/2}$ (I_{650}) UC PL, as well as (c) $^4I_{13/2} \rightarrow {}^4I_{15/2}$ (I_{1534}) DC PL under 980 nm excitation.

In addition, the coordination-environment-sensitive Er luminescence can provide another instant verification to rule out the high-symmetry cubic and tetragonal HfO_2 phase from an optical perspective. The Er^{3+} $^2H_{11/2} \rightarrow {}^4I_{15/2}$ transition (the 525 nm green emission) is a hypersensitive transition in term of the surrounding chemical environments, while the intensity of $^4F_{9/2} \rightarrow {}^4I_{15/2}$ transition (the 660 nm red emission) is relatively stable against local symmetry variations. In that case, the symmetry order

of different chemical environments can be compared by the green-to-red intensity ratios (I_{green}/I_{red}) of the incorporated Er. For instance, Wang and co-workers reported the distinct Er luminescence variation between cubic ZrO_2 with dominated I_{red} and monoclinic ZrO_2 with greatly increased I_{green}/I_{red},[173] thereby commensurate difference should be expected from HfO_2 with analogous phase structures. Similarly, the Hf sites in *Fm-3m* cubic HfO_2 are coordinated by 8 oxygen atoms, forming a perfectly symmetric [HfO_8] cube; whereas the [HfO_7] polyhedron in *o*-HfO_2 and monoclinic HfO_2 is rather highly distorted. The UC PL emission spectrum of the HErO target was then recorded (**Figure 5.21a**), which contains a majority of cubic phase and monoclinic phase (**Figure 5.21b**) from solid-state reaction, is taken as a reference. In **Figure 5.21a**, the I_{green} of HErO film is clearly more intense than I_{red}, while the spectrum of HErO target shows a larger I_{red} than I_{green}. The results suggest that Er has incorporated into crystalline sites with more asymmetric surroundings in the HErO thin film compared to the targets. Considering the comparable distortion indices (L_D) and effective coordination number (E_{CN}) of Hf in the *o*-phase (L_D=0.024 Å, E_{CN} = 6.70) and monoclinic (L_D=0.028 Å, E_{CN} = 6.62) lattices, the drastic difference in I_{green}/I_{red}, rule out the possibility of the HErO film to be cubic phase (L_D=0.00 Å, E_{CN} = 8.00). Likewise, the less ambiguous tetragonal HfO_2(011) plane at 2θ=~30° can also be ruled out because of its highly symmetric [HfO_6] octahedral (L_D=0.00053 Å, E_{CN} = 6.00). Therefore, for the HErO system, the ambiguous HfO_2 phase among the non-FE *c*-, *m*-, *t*-phase and the FE *o*-HfO_2 can be well distinguished by combining the XRD and PL results as schematically illustrated in **Figure 5.21c**.

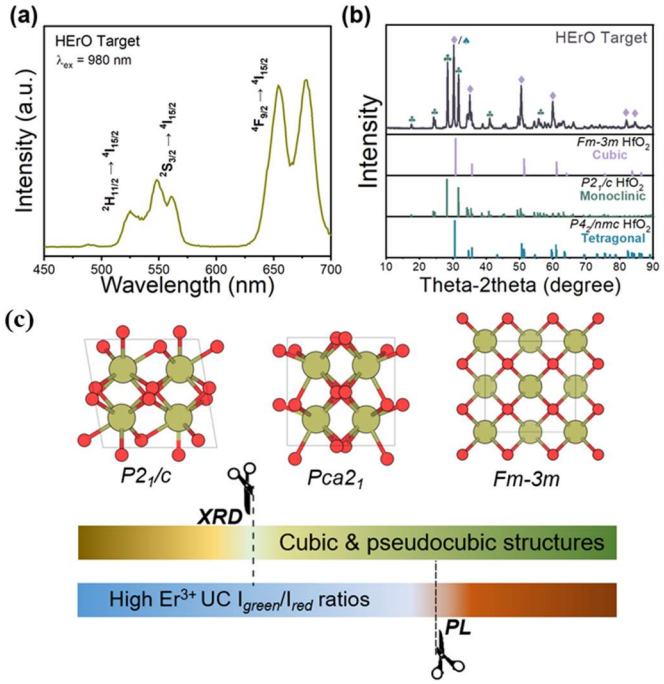

Figure 5.21 (a) XRD of the HErO targets. (b) UC PL spectrum of the HErO targets. (c) Schematic illustration of combining XRD and PL results for determining the phase composition of HErO.

5.5 High-endurance ferroelectricity in HErO thin films

The FE properties of HErO film were then validated by PFM. Using the 11-nm-thick sample as a reference, standard PFM off-field hysteresis loops can be obtained as shown in **Figure 5.22a**, where the phase and amplitude loops coincide with a coercive voltage of ~5 V. The topographic AFM scan in **Figure 5.22b** shows a flat and smooth surface morphology of the as-deposited HErO thin film with a standard root-mean-square roughness of ~220 pm. To further demonstrate the switchable nature of the polarization, PFM domain patterning experiments were performed by applying ±9 V bias to locally write out-of-plane polarization domains on the HErO film, as shown in

Figure 5.22c. The resulting PFM phase image displays a distinct 180° phase contrast between the oppositely poled regions (separated by red dot lines), which is confirmed by the line scan of the cyan line in the inset figure. This sharp phase reversal provides direct evidence for the reversible and stable FE domain switching in the HErO film at microscopic scale.

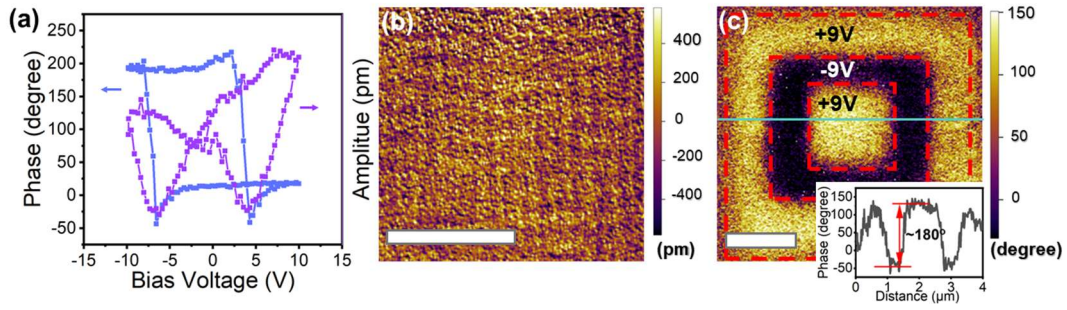

Figure 5.22 (a) The microscopic hysteresis loop of the ~11-nm PLD-deposited HErO thin film. (b) The AFM image and (c) the phase image after PFM domain patterning of HErO, where the inset shows a line scan of phase contrast of the tagged cyan line.

P-E experiments were carried out to evaluate the macroscopic FE properties of the HErO films. For these measurements, circular gold top electrodes with a radius of 37 μm were deposited by E-beam deposition onto the film surface to define a metal-ferroelectrics-metal (MFM) capacitor structure. The resulting *P-E* and *I-E* were shown in **Figure 5.23a** using the PUND measurements, where classic hysteresis loops can be viewed. As the applied electric field increases beyond the E_c (~4 MV/cm) the polarization eventually reaches the saturation level indicating that most switchable dipoles have all aligned to the biased direction. While polarization continues increasing upon further increasing electric filed strength, only dielectric displacement or leakage currents are contributed. Here, the PUND measurements can effectively wipe out the

components of leakage currents in polarization, giving a more reliable estimation of the FE properties. The 11-nm-thick HErO gives P_r value of ~21 μC/cm^2, which is a modest value among other doped systems. The corresponding *I-E* curves display two distinct peaks around $\pm E_c$ that arise from the switching currents associated with domain reversal. **Figure 5.23b** presents the characteristic double-peak capacitance-electric field (*C-E*) curves, which shows a dielectric constant of 37.5. The value is higher than those of the conventional HZO thin films. The slight asymmetry observed in both the *P-E* and *C-E* curves may be attributed to the Schottky barriers formed at the asymmetric LSMO bottom or Au/Ti top interfaces. Finally, **Figure 5.23c** gives the retention test of polarization states. It reveals that the polarization states can remain stable for an extrapolated duration exceeding ten years, demonstrating notably stable retention behaviors of non-volatile polarizations.

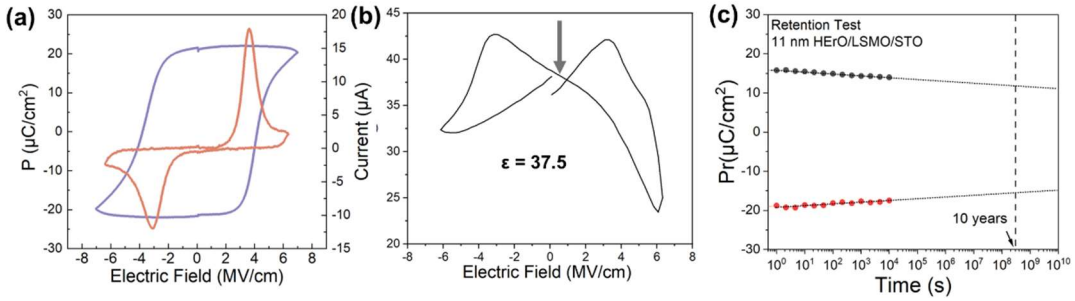

Figure 5.23 FE properties of 11-nm-thick HErO (a) PUND *P-E* and *I-E* measurements. (b) *C-E* measurements. (c) Retention test with logarithmic fitting with extrapolated 10-year expectation.

The electrical wake-up effect and limited endurance remain significant challenges for FE HfO_2. Here, FE endurance measurements were carried out to assess the switching stability of HErO. The results are shown in **Figure 5.24a**. No electrical wake-

up phenomenon was observed because the high-quality, single-phase epitaxial HErO films do not require field-induced poling to induce the FE phase transition or to redistribute oxygen defects, which are crucial in polycrystalline HfO_2 thin films.[135 174] More importantly, it shows minor degradation of FE properties (in terms of P_r) throughout the process of 10^{11} bipolar switching cycles at 1 MHz, which is among the best endurance properties of FE HfO_2 reported to date. The corresponding *P-V* and *I-V* curves recorded at various cycles are plotted in **Figure 5.24b** and **c**, showing well-defined hysteresis loops persist even at the end of the endurance test. However, as shown in **Figure 5.24b**, starting at around 10^8 cycles the saturation polarization and P_r both begin to decline, and this decay accelerates with further cycling. In the meantime, in the *I-E* features (**Figure 5.24c**), the switching current peak location also graduate shifts with decreasing peak intensity and broadened fwhm. The reason can be assigned to the progressively acuminated and deteriorated charge pinning of $V_O^{\bullet\bullet}$ at the domain walls during repeated switching, which impedes the further domain reversal. The endurance test was performed under varied electric field strengths (7 and 8 MV/cm) and cycling frequencies (100 kHz and 10 MHz) based on the 11-nm-thick HErO thin films (**Figure 5.25**). All the measurements can confirm the high endurance performance of HErO thin films.

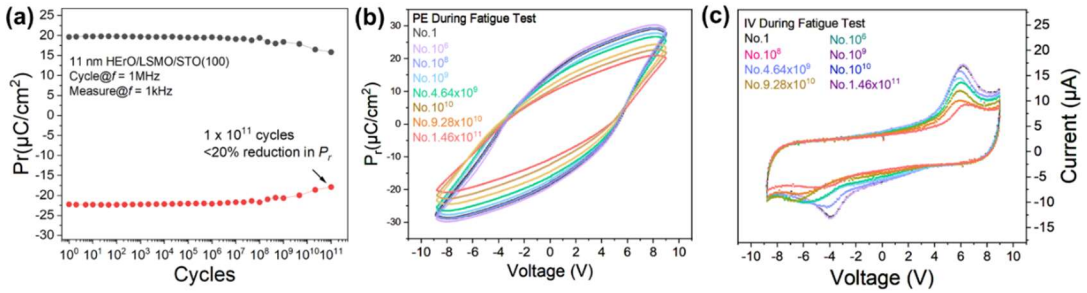

Figure 5.24 Endurance test of 11-nm-thick HErO. (a) Fatigue tests of 10^{11} cycle at 1MHz. (b) The *P-V* and (c) *I-V* tests during fatigue tests.

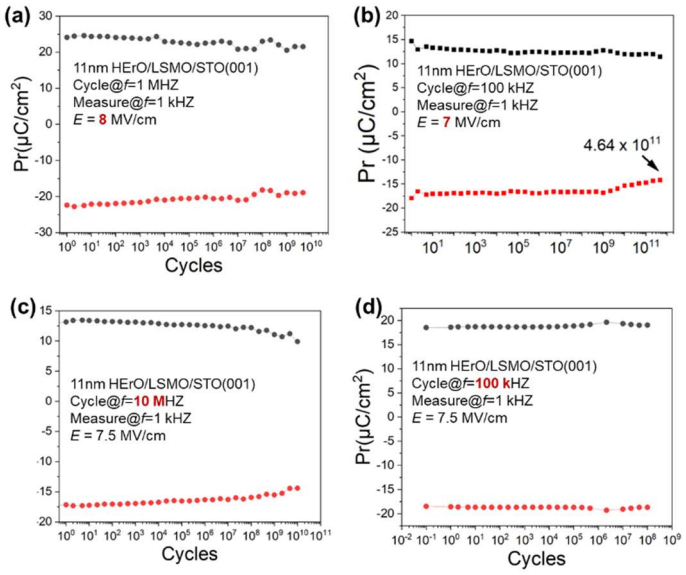

Figure 5.25 Endurance test at other parameters. (a) Fatigue tests at 7.5 MV/cm. (b) Fatigue tests at 7.5 MV/cm. (c) Fatigue tests at 10 MHz. (d) Fatigue tests at 100 kHz.

As discussed previously, FE fatigue during endurance tests is majorly attributed to the V_O generation and migrations upon electrical cycling. Therefore, careful XAS study was performed on 11-nm HErO to qualitatively compare the local structure variations during cycling caused by V_O, which results in a change in the electronic structure. The CB of HfO_2 sample consists of metal d states Hf 5d at the lower energy range and metal *sp* continuum states at the higher energy range. The O *K*-edge XAS reflects the DOS of these CB states convoluted with the hybridization strength. The XAS results show the metal d states were well separated in energy from the metal *sp* states for all HErO samples. Moreover, the XAS of sample cycling up to $1E^8$ shows good consistency with original state, demonstrating the robustness of the electronic structure during cycling.

The XAS splitting feature associated with the Hf e_g state (*i.e.*, peaks at 532.0 and 532.9 eV) as well as the sub-bandgap absorption feature in the $1E^{10}$ sample are noteworthy. Recent studies have attributed both phenomena to the Jahn-Teller deformation of the octahedral oxygen cage surrounding the Hf ion in HfO_2 nanocrystals or grain boundaries. This phenomenon indicates an irreversible twisting and destruction of the crystal structure have happened upon 10^{10} switching cycles, which may be the reason behind the P_r reduction and imprint as measured in the endurance tests.

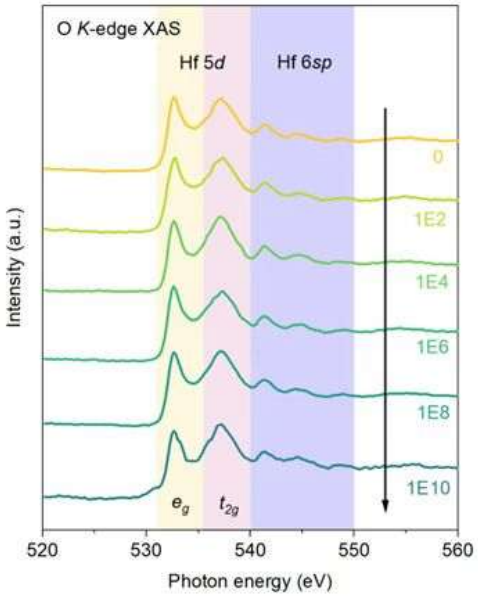

Figure 5.26 O *K*-edge XAS of pristine HErO and after 10^2 to 10^{10} switching cycles.

Finally, the performance of FE HErO was benchmarked with other dopants according to the P_r value and endurance cycle (**Figure 5.27**). The criteria were set as 75% retention of P_r, which is believed to be the critical threshold for maintaining device reliability.[175] HErO demonstrates a highly competitive position among all reported FE doped HfO_2 systems. Combined with its integrated optical reactivity, the coexistence

of robust FE and PL properties in the HErO system highlights its potential as a versatile multi-mode ultrathin platform for advanced applications.

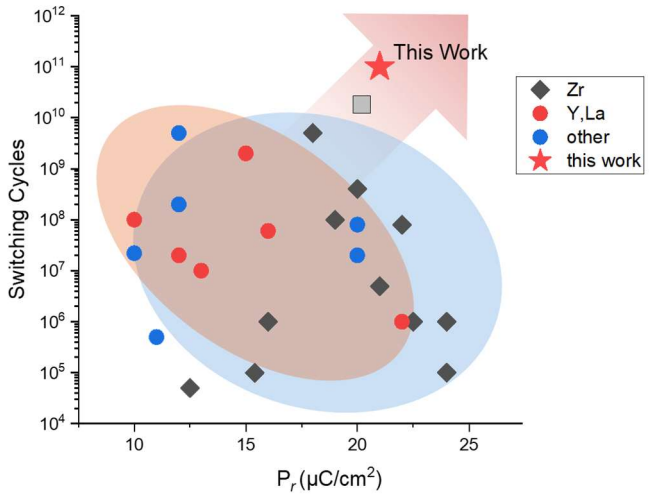

Figure 5.27 Benchmarking of HErO against other FE HfO_2.

5.6 Summary

In conclusion, this research delve into the unexploited Er dopants with an intriguing two-way doping effect in HfO_2. First-principles DFT simulations reveal the dual role undertaken by Er incorporation: the stabilization of robust ferroelectricity akin to the extensively studied FE HYO, and the emergence of localized Er 4*f* states within the wide bandgap of HErO. These 4*f* states facilitate abundant intra-configurational electronic transitions, setting HErO apart from other doped HfO_2 systems. Therefore, the work establishes the theoretical two-way doping of Er in HfO_2 with intrinsically incorporated Er PL properties and highly endurable FE. Subsequently, experimental validations were conducted based on PLD-grown epitaxial HErO/LSMO/STO thin films with high quality. Spectral analyses verify the successful incorporation of both

DC and UC PL properties within the FE HErO film, exhibiting both NIR and visible photoemissions under 980 nm excitation. Then the robust ferroelectricity was confirmed in the HErO systems within wide thickness ranging from 3 nm to 30 nm. In addition, notable endurance was found in the HErO to survive up to 10^{11} switching cycles without breakdown or FE failure. This work showcases the superposition of high-endurance FE and intrinsic PL properties in the epitaxial HErO thin films, offering a promising platform for developing future multi-mode devices at ultrathin levels.

Chapter 6 Conclusions and Future Prospects

6.1 Conclusions

The explosive growth of data across diverse media in the information age necessitates innovative approaches to information processing technologies and the development of multi-mode devices that extend beyond conventional electrical paradigms. Luminescence has long been utilized as a fundamental medium for information storage and display, whereas the potential in all-optical computing has yet been fully unleashed. Therefore, exploiting the dynamic properties of light offers significant potential for creating smart luminescent systems capable of sophisticated information processing. This thesis explored the uncharted region by engineering PL properties of smart nanocomposites to examine the potential of PL-based neuromorphic behaviors and the related information processing capability. The further scaling-down integration of PL into main-stream electronics like FE HfO_2 is also studied. The main research of the thesis is summarized below.

First, this work constructed the MHPe@MYE smart nanocomposites with light-induced PL variation and dark recovery behaviors. Comparison studies and DFT simulation evidence the importance of interfacial interaction in the systems, unravelling the light-induced adaptive halogen migration as the core mechanism behind reversible and history-dependent PL property variations. This PL variation process mimics key synaptic functions, including PPF, LTM, and STP/LTP, as experimentally validated through programmed excitation pulses and spectral analyses over a wide excitation (365 – 450 nm) and emission (470 – 520 nm) ranges, establishing the fundaments of PL-

based neuromorphic behaviors. Leveraging these intrinsic neuromorphic PL dynamics, this work constructed a full PL-based physical reservoir computing platform where optical "Write" stimuli progressively modify the material state, while non-destructive "Read" operations probe the PL features. This system successfully processed temporal information, distinguishing 4-bit binary sequences through unique PL kinetic signatures, and achieved markedly high accuracy (94.4%) in UV recognition when integrated with software-based ANN, validating the feasibility of PL-based neuromorphic computing.

Furthermore, this work explores the integration of PL functionality into FE HfO_2 systems by introducing Er as a dual-functional dopant. Theoretical simulations revealed that Er not only stabilizes the metastable FE *o*-phase with anchored V_O migration near Er dopants, but also creates localized Er 4*f* states within the band gap that enabling UC and DC PL. Experimentally, HErO thin films (3-30 nm) grown by PLD results in high-quality epitaxial HErO/LSMO/STO(001) thin films. PL measurements under 980 nm excitation reveal clear UC PL in the visible bands ($^2H_{11/2} \rightarrow {}^4I_{15/2}$, $^2S_{3/2} \rightarrow {}^4I_{15/2}$, $^4F_{9/2} \rightarrow {}^4I_{15/2}$) alongside DC PL ($^4I_{13/2} \rightarrow {}^4I_{15/2}$) at around 1530 nm, confirming the successful integration of PL into HErO at ultrathin level (~11 nm). In the meantime, the HErO thin films also exhibit robust ferroelectricity with P_r of ~21 μC/cm^2 and notably high dielectric constant of 37.5. More importantly, the 11-mn HErO can sustain over 10^{11} polarization switching cycles at 1 MHz without breakdown or failure of FE, significantly exceeding the typical endurance limits of other doped FE HfO_2. The retention of polarization states can also be extracted to more than 10 years. Collectively, HErO represents a dual-mode ultrathin platform with both UC/DC PL and high-endurance FE, potentially paving the way for advanced multifunctional devices information processing at the nanoscale.

6.2 Future prospects

It is important to note that the current PL-based neuromorphic behaviors as demonstrated in MHPe@MYE and PersL primarily emulate excitatory processes, which are fundamental to memory formation, reinforcement, and retention.[176] In contrast, biological synapses also perform inhibitory functions, which are not yet fully replicated in these systems, including the non-volatile memory and inhibitory behaviors. Bidirectional optical modulation is rather technically challenging to achieve in the form PL responses. This can be largely due to the inherently unidirectional propagation of light, which makes PL-based inhibitory excitation necessitates further mechanical innovation. Drawing inspiration from advances in optoelectronic devices, recent studies have shown that heterostructure architectures can facilitate both excitatory and inhibitory modulations of the resistance states via optical stimuli.[81,177,178] Additionally, other research has demonstrated the feasibility of implementing inhibitory behaviors through electrical or hybrid optical-electrical controls.[115,179] Investigation and exploitation on the driving force of dark-recoverable halogen migration mechanisms in the present MHPe@MYE may also provide an alternative way of achieving controlled inhibitory pathway. These strategies offer valuable perspectives for expanding the neuromorphic capabilities and functionalities of the current reported "*smart phosphor*" systems, especially for the potential heterostructural materials engineering and the deliberate integration of secondary physical interfaces.

The further translation of these promising demonstrations into practical PL-based computing platforms requires overcoming several key obstacles such as the immaturity of device architectures in PL-based neuromorphic systems, the underexplored phosphor

materials exhibiting neuromorphic functionalities, and the algorithmic innovations tailored for spectral PL processing. While major challenges persist in device architectures and algorithm developments, the compatibility of "*smart phosphors*" with existing phosphor-converted device architectures (*e.g.*, fibers, glasses, displays, and lighting),[180-182] suggests a viable pathway toward contact-less and visually interpretable neuromorphic computing.

Alternatively, the incorporation of smart PL into existing platforms may be a more direct pathway to establish PL-integrated multi-mode and multifunctional devices. Based on the successful integration of UC and DC PL in FE HfO_2 in this work, a deeper understanding of the interplay between FE polarization and PL tuning in HErO thin films will further facilitate the development of multifunctional devices at compatible and ultrathin-film level. This may represent a significant advancement over current approaches that primarily achieve multifunctionality at the device levels, where FE HfO_2 serves predominantly as an electrical signal processor within complex architectures. Unraveling the connection between FE polarization and PL tuning can enable HErO to respond to a wider range of stimulus beyond electrical signals. This capability is crucial for designing highly integrated and miniaturized FE HfO_2-based multifunctional devices, which can potentially contribute to an optical upgrade kit for the existing hardware based on FE HfO_2.[56,183] Similar scaling-down integration of PL into other functional layers of hardware can follow the same pathway. The simultaneous exploitation of electrical and optical information processing on a single ultrathin platform would represent an exciting direction for next-generation multimodal computing.

References

1 G. G. Blasse, BC. Luminescent materials (Springer Verlag, 1994).

2 V. P. Gupta.Principles and Applications of Quantum Chemistry (Academic Press, 2016).

3 N. Bloembergen. Solid state infrared quantum counters. *Phys. Rev. Lett.* 2, 84 (1959). https://doi.org/10.1103/PhysRevLett.2.84

4 F. Wang, R. Deng, J. Wang, Q. Wang, Y. Han, H. Zhu, X. Chen and X. Liu. Tuning upconversion through energy migration in core-shell nanoparticles. *Nat. Mater.* 10, 968 (2011). https://doi.org/10.1038/nmat3149

5 B. Zhou, B. Shi, D. Jin and X. Liu. Controlling upconversion nanocrystals for emerging applications. *Nat. Nanotechnol.* 10, 924 (2015). https://doi.org/10.1038/nnano.2015.251

6 X. Zhu, Y. Zhao, S. Zhang, J. Wu, D. Shao, E. Song, Q. Zhang, C. Yin and S. Ye. Isolated-Mn^{2+}-like Luminescent Behavior in $CsMnF_3$ Caused by Competing Magnetic Interactions at Cryogenic Temperature. *J. Phys. Chem. C* 125, 27800 (2021). https://doi.org/10.1021/acs.jpcc.1c08536

7 G. Blasse. The physics of new luminescent materials. Mater. chem. phys. 16, 201 (1987). https://doi.org/10.1016/0254-0584(87)90100-3

8 L.-Y. Huang and W. R. L. Lambrecht. Electronic band structure trends of perovskite halides: Beyond Pb and Sn to Ge and Si. *Phys. Rev. B* 93, 195211 (2016). https://doi.org/10.1103/PhysRevB.93.195211

9 G. Bai, M.-K. Tsang and J. Hao. Tuning the Luminescence of Phosphors: Beyond Conventional Chemical Method. *Adv. Opt. Mater.* 3, 431 (2015). https://doi.org/10.1002/adom.201400375

10 G. Li, Y. Tian, Y. Zhao and J. Lin. Recent progress in luminescence tuning of Ce^{3+} and Eu^{2+}-activated phosphors for pc-WLEDs. *Chem. Soc. Rev.* 44, 8688 (2015). https://doi.org/10.1039/C4CS00446A

11 M.-C. Wong, Y. Zhang and J. Hao.Phosphor Handbook (CRC Press, 2022).

12 G. Bai, M.-K. Tsang and J. Hao. Tuning the Luminescence of Phosphors: Beyond Conventional Chemical Method. *Adv. Opt. Mater.* 3, 431 (2015). https://doi.org/10.1002/adom.201400375

13 M.-H. Fang, Z. Bao, W.-T. Huang and R.-S. Liu. Evolutionary Generation of Phosphor Materials and Their Progress in Future Applications for Light-Emitting Diodes. *Chem. Rev.* 122, 11474 (2022). https://doi.org/10.1021/acs.chemrev.1c00952

14 S. Hariyani, M. Sójka, A. Setlur and J. Brgoch. A guide to comprehensive phosphor discovery for solid-state lighting. *Nat. Rev. Mater.* 8, 759 (2023). https://doi.org/10.1038/s41578-023-00605-6

15 Z. Xia and A. Meijerink. Ce^{3+}-Doped garnet phosphors: composition modification, luminescence properties and applications. *Chem. Soc. Rev.* 46, 275 (2017). https://doi.org/10.1039/C6CS00551A

16 Z. Xia and Q. Liu. Progress in discovery and structural design of color conversion phosphors for LEDs. *Prog. Mater. Sci.* 84, 59 (2016). https://doi.org/10.1016/j.pmatsci.2016.09.007

17 Y. Ge, M. Zhao, Y. Zhao and X. Zhang. Tailoring of Blue-Cyan Luminescence in $Rb_3Y[(P_{1-x}Si_x)O_4]_2:Eu^{2+}$ Phosphor via Si^{4+}-P^{5+} Heterovalent Substitution for Full-Spectrum Healthy Lighting. *Laser Photonics Rev.* 19, 2500026 (2025). https://doi.org/10.1002/lpor.202500026

18 L. Chen, P. Cheng, Z. Zhang, L. He, Y. Jiang, G. Li, X. Jing, Y. g. Qin, M. Yin, T.-S. Chan, B. Hong, S. Tao, W. Chu, Z. Zhao, H. Ni, H. Kohlmann and O. Oeckler. Reduced Local Symmetry in Lithium Compound Li_2SrSiO_4 Distinguished by an Eu^{3+} Spectroscopy Probe. *Adv. Sci.* 6, 1802126 (2019). https://doi.org/10.1002/advs.201802126

19 M. Zhao, H. Liao, L. Ning, Q. Zhang, Q. Liu and Z. Xia. Next-Generation Narrow-Band Green-Emitting $RbLi(Li_3SiO_4)_2:Eu^{2+}$ Phosphor for Backlight Display Application. *Adv. Mater.* 30, 1802489 (2018). https://doi.org/10.1002/adma.201802489

20 J. Xiang, J. Chang, C. Chen, S. Jin, R. Chen, R. Gao, M. Jin and C. Guo. Recent progress of inorganic phosphors in artificial plant cultivation LEDs. *J. Mater. Chem. C* 13, 1538 (2025). https://doi.org/10.1039/D4TC04641B

21 S. Li, Y. Guo and R.-J. Xie. Laser Phosphors for Next-Generation Lighting Applications. *Acc. Mater. Res.* 3, 1299 (2022). https://doi.org/10.1021/accountsmr.2c00193

22 Z. Yang, T. de Boer, P. M. Braun, B. Su, Q. Zhang, A. Moewes and Z. Xia. Thermally Stable Red-Emitting Oxide Ceramics for Laser Lighting. *Adv. Mater.* 35, 2301837 (2023). https://doi.org/10.1002/adma.202301837

23 Z. Yang, Y. Zhao, J. Ueda, M. S. Molokeev, M. Shang and Z. Xia. Engineering charge-transfer interactions for red-emitting $SrLa(Sc,Ga)O_4:Ce^{3+}$ phosphor with improved thermal stability. *Sci. China Mater.* 66, 1989 (2023). https://doi.org/10.1007/s40843-022-2315-9

24 H. Ming, Y. Zhao, Y. Zhou, M. S. Molokeev, Y. Wang, E. Song and Q. Zhang. Chemical Group Substitution Enables Highly Efficient Mn^{4+} Luminescence in

Heterovalent Systems. *Adv. Opt. Mater.* 11, 2300076 (2023). https://doi.org/10.1002/adom.202300076

25 Y. Zhang, G. Gao, H. L. W. Chan, J. Dai, Y. Wang and J. Hao. Piezo-phototronic effect-induced dual-mode light and ultrasound emissions from ZnS:Mn/PMN-PT thin-film structures. *Adv. Mater.* 24, 1729 (2012). https://doi.org/10.1002/adma.201104584

26 Q. Zhang, H. Sun, X. Wang, X. Hao and S. An. Reversible Luminescence Modulation upon Photochromic Reactions in Rare-Earth Doped Ferroelectric Oxides by in Situ Photoluminescence Spectroscopy. *ACS Appl. Mater. Interfaces* 7, 25289 (2015). https://doi.org/10.1021/acsami.5b07345

27 C. Zhang, Q. Yin, S. Ge, J. Qi, Q. Han, W. Gao, Y. Wang, M. Zhang and J. Dong. Optical anti-counterfeiting and information storage based on rare-earth-doped luminescent materials. *Mater. Res. Bull.* 176, 112801 (2024). https://doi.org/10.1016/j.materresbull.2024.112801

28 J. Zhang, Z. Wang, X. Huo, X. Meng, Y. Wang, H. Suo and P. Li. Anti-Counterfeiting Application of Persistent Luminescence Materials and Its Research Progress. *Laser Photonics Rev.* 18, 2300751 (2024). https://doi.org/10.1002/lpor.202300751

29 Z. Huang, B. Chen, B. Ren, D. Tu, Z. Wang, C. Wang, Y. Zheng, X. Li, D. Wang, Z. Ren, S. Qu, Z. Chen, C. Xu, Y. Fu and D. Peng. Smart Mechanoluminescent Phosphors: A Review of Strontium-Aluminate-Based Materials, Properties, and Their Advanced Application Technologies. *Adv. Sci.* 10, 2204925 (2023). https://doi.org/10.1002/advs.202204925

30 C. Zhang, M. Ji, X. Zhou, X. Mi, H. Chen, B. Zhang, Z. Fu, Z. Zhang and H. Zheng. Plasmon-Assisted Self-Encrypted All-Optical Memory. *Adv. Funct. Mater.* 33, 2208561 (2023). https://doi.org/10.1002/adfm.202208561

31 Y. Wang, Q. Zhang, C. Yang and Z. Xia. Ratiometric Fluorescence Optical Fiber Enabling Operando Temperature Monitoring in Pouch-Type Battery. *Adv. Mater.* 36, 2401057 (2024). https://doi.org/10.1002/adma.202401057

32 W. W. Ye, M.-K. Tsang, X. Liu, M. Yang and J. Hao. Upconversion Luminescence Resonance Energy Transfer (LRET)-Based Biosensor for Rapid and Ultrasensitive Detection of Avian Influenza Virus H7 Subtype. *Small* 10, 2390 (2014). https://doi.org/10.1002/smll.201303766

33 Y. Liu, X. Lao, M.-C. Wong, M. Song, Y. Zhao, Y. Ma, Q. Bai and J. Hao. Intelligent Point-of-Care Biosensing Platform Based on Luminescent Nanoparticles and Microfluidic Biochip with Machine Vision Algorithm Analysis. *Nano-Micro Lett.* 17, 215 (2025). https://doi.org/10.1007/s40820-

025-01745-w

34 Y. Zuo, J. Liu, P. Li, K. Li, J. W. Y. Lam, D. Wu and B. Z. Tang. Full-color-tunable AIE luminogens for 4D code, security patterns, and multicolor LEDs. *Cell Rep. Phys. Sci.* 4 (2023). https://doi.org/10.1016/j.xcrp.2022.101202

35 R. E. Cohen. Origin of ferroelectricity in perovskite oxides. *Nature* 358, 136 (1992). https://doi.org/10.1038/358136a0

36 M. Stewart, M. G. Cain and D. Hall. Ferroelectric hysteresis measurement and analysis. (1999).

37 J. Valasek. Piezo-electric and allied phenomena in Rochelle salt. *Phys. Rev.* 17, 475 (1921).

38 J. Valasek. The early history of ferroelectricity. *Ferroelectrics* 2, 239 (1971).

39 M. Humayun, Z. Li, M. Israr, A. Khan, W. Luo, C. Wang and Z. Shao. Perovskite Type ABO_3 Oxides in Photocatalysis, Electrocatalysis, and Solid Oxide Fuel Cells: State of the Art and Future Prospects. *Chem. Rev.* 125, 3165 (2025). https://doi.org/10.1021/acs.chemrev.4c00553

40 W. Gao, Y. Zhu, Y. Wang, G. Yuan and J.-M. Liu. A review of flexible perovskite oxide ferroelectric films and their application. *J. Materiomics* 6, 1 (2020). https://doi.org/10.1016/j.jmat.2019.11.001

41 H. D. Megaw. Origin of ferroelectricity in barium titanate and other perovskite-type crystals. *Acta Crystallogr.* 5, 739 (1952).

42 J.-M. Hu, L.-Q. Chen and C.-W. Nan. Multiferroic Heterostructures Integrating Ferroelectric and Magnetic Materials. *Adv. Mater.* 28, 15 (2016). https://doi.org/10.1002/adma.201502824

43 L. Bai, C. Ke, Z. Luo, T. Zhu, L. You and S. Liu. Intrinsic Ferroelectric Switching in Two-Dimensional α-In_2Se_3. *ACS Nano* 18, 26103 (2024). https://doi.org/10.1021/acsnano.4c06619

44 Z. Zhou, S. Wang, Z. Zhou, Y. Hu, Q. Li, J. Xue, Z. Feng, Q. Yan, Z. Luo, Y. Weng, R. Tang, X. Su, F. Zheng, K. Okamoto, H. Funakubo, L. Kang, L. Fang and L. You. Unconventional polarization fatigue in van der Waals layered ferroelectric ionic conductor $CuInP_2S_6$. *Nat. Commun.* 14, 8254 (2023). https://doi.org/10.1038/s41467-023-44132-y

45 X. Jiang, X. Zhang, Z. Deng, J. Deng, X. Wang, X. Wang and W. Yang. Dual-role ion dynamics in ferroionic $CuInP_2S_6$: revealing the transition from ferroelectric to ionic switching mechanisms. *Nat. Commun.* 15, 10822 (2024). https://doi.org/10.1038/s41467-024-55160-7

46 Z. Fei, W. Zhao, T. A. Palomaki, B. Sun, M. K. Miller, Z. Zhao, J. Yan, X. Xu and D. H. Cobden. Ferroelectric switching of a two-dimensional metal. *Nature*

560, 336 (2018). https://doi.org/10.1038/s41586-018-0336-3

47 Y. Bai, Z. Yu, Z. Guan, J. Tian, C. Wang, X. Yao, Y. Yang, Y. Lei, J. Xu, C. Liu, J. Zhu, Y. Tu, S. Shen, H. Xiang, X. Li, C. Xu and J. Wang. Sub-nanosecond polarization switching with anomalous kinetics in vdW ferroelectric WTe_2. *Nat. Commun.* 16, 7221 (2025). https://doi.org/10.1038/s41467-025-62608-x

48 D. Ji, S. Cai, T. R. Paudel, H. Sun, C. Zhang, L. Han, Y. Wei, Y. Zang, M. Gu, Y. Zhang, W. Gao, H. Huyan, W. Guo, D. Wu, Z. Gu, E. Y. Tsymbal, P. Wang, Y. Nie and X. Pan. Freestanding crystalline oxide perovskites down to the monolayer limit. *Nature* 570, 87 (2019). https://doi.org/10.1038/s41586-019-1255-7

49 L. Rogée, L. Wang, Y. Zhang, S. Cai, P. Wang, M. Chhowalla, W. Ji and S. P. Lau. Ferroelectricity in untwisted heterobilayers of transition metal dichalcogenides. *Science* 376, 973 (2022). https://doi.org/10.1126/science.abm5734

50 H. Ryu, K. Xu, D. Li, X. Hong and W. Zhu. Empowering 2D nanoelectronics via ferroelectricity. *Appl. Phys. Lett.* 117 (2020). https://doi.org/10.1063/5.0019555

51 U. Schroeder, M. H. Park, T. Mikolajick and C. S. Hwang. The fundamentals and applications of ferroelectric HfO_2. *Nat. Rev. Mater.* 7, 653 (2022). https://doi.org/10.1038/s41578-022-00431-2

52 T. S. Böscke, J. Müller, D. Bräuhaus, U. Schröder and U. Böttger. Ferroelectricity in hafnium oxide thin films. *Appl. Phys. Lett.* 99 (2011). https://doi.org/10.1063/1.3634052

53 J. Müller, E. Yurchuk, T. Schlösser, J. Paul, R. Hoffmann, S. Müller, D. Martin, S. Slesazeck, P. Polakowski, J. Sundqvist, M. Czernohorsky, K. Seidel, P. Kücher, R. Boschke, M. Trentzsch, K. Gebauer, U. Schröder and T. Mikolajick. in *2012 Symposium on VLSI Technology* (VLSIT).

54 K. Hosen, M. S. Islam, C. Stampfl and J. Park. Numerical Analysis of Gate-All-Around $HfO_2/TiO_2/HfO_2$ High-*K* Dielectric Based WSe_2 NCFET With Reduced Sub-Threshold Swing and High On/Off Ratio. *IEEE Access* 9, 116254 (2021). https://doi.org/10.1109/ACCESS.2021.3105341

55 A. I. Khan, J.-K. Kim, U. Sikder, K. Das, T. Rodriguez, R. Soman, S. Chowdhury and S. Salahuddin. Negative capacitance overcomes Schottky-gate limits in GaN high-electron-mobility transistors. *Science* 389, 508 (2025). https://doi.org/10.1126/science.adx6955

56 J. Y. Park, D.-H. Choe, D. H. Lee, G. T. Yu, K. Yang, S. H. Kim, G. H. Park, S.-G. Nam, H. J. Lee, S. Jo, B. J. Kuh, D. Ha, Y. Kim, J. Heo and M. H. Park.

Revival of Ferroelectric Memories Based on Emerging Fluorite-Structured Ferroelectrics. *Adv. Mater.* 35, 2204904 (2023). https://doi.org/10.1002/adma.202204904

57 J. Hao, Y. Zhang and X. Wei. Electric-Induced Enhancement and Modulation of Upconversion Photoluminescence in Epitaxial $BaTiO_3$:Yb/Er Thin Films. *Angew. Chem. Int. Ed* 50, 6876 (2011). https://doi.org/10.1002/anie.201101374

58 H. Chen, J. Shen, X. Du, S. Cai, F. Guo, W. F. Io, T. Zhou, Z. Dong, T. Bian, J. Guo, W. Liu, Y. Zhang, Z. Wu and J. Hao. Frequency converting and digital modulation of light derived from lanthanide for signal encoding and logic computing. *InfoMat* 6, e12547 (2024). https://doi.org/10.1002/inf2.12547

59 Y. Wen, Y. Cao, H. Ren, X. Du, J. Guo, Z. Wu, W. Liu, J. Du and Y. Zhang. Ferroelectric Optical Memristors Enabled by Non-Volatile Electro-Optic Effect. *Adv. Mater.* 37, 2417658 (2025). https://doi.org/10.1002/adma.202417658

60 R. Sun, Y. Jia, B. Lai, Z. Shi, M. Liu, W. Yu, K. Jiang, S. Zhang, S. Lv, Y. Chen, X. Sun and D. Li. Phase-pure ferroelectric quantum wells with tunable photoluminescence for multi-state optoelectronic applications. *Light Sci. Appl.* 14, 228 (2025). https://doi.org/10.1038/s41377-025-01874-2

61 N. D. Petkovich and A. Stein. Controlling macro- and mesostructures with hierarchical porosity through combined hard and soft templating. *Chem. Soc. Rev.* 42, 3721 (2013). https://doi.org/10.1039/C2CS35308C

62 G. F. Harrington and J. Santiso. Back-to-Basics tutorial: X-ray diffraction of thin films. *J. Electroceramics* 47, 141 (2021). https://doi.org/10.1007/s10832-021-00263-6

63 B. J. Inkson.Materials Characterization Using Nondestructive Evaluation (NDE) Methods (Woodhead Publishing, 2016).

64 J. I. Goldstein, D. E. Newbury, P. Echlin, D. C. Joy, C. E. Lyman, E. Lifshin, L. Sawyer and J. R. Michael.Scanning Electron Microscopy and X-ray Microanalysis: Third Edition (Springer US, 2003).

65 M. S. Rana, H. R. Pota and I. R. Petersen. Improvement in the Imaging Performance of Atomic Force Microscopy: A Survey. *IEEE Trans. Autom. Sci. Eng.* 14, 1265 (2017). https://doi.org/10.1109/TASE.2016.2538319

66 G. Kresse and J. Furthmüller. Efficiency of *ab-initio* total energy calculations for metals and semiconductors using a plane-wave basis set. *Compl. Mater. Sci.* 6, 15 (1996). https://doi.org/10.1016/0927-0256(96)00008-0

67 H. Jiang, P. Rinke and M. Scheffler. Electronic properties of lanthanide oxides from the *GW* perspective. *Phys. Rev. B* 86, 125115 (2012). https://doi.org/10.1103/PhysRevB.86.125115

68 K. Momma and F. Izumi. VESTA 3 for three-dimensional visualization of crystal, volumetric and morphology data. *J. Appl. Crystallogr.* 44, 1272 (2011). https://doi.org/10.1107/S0021889811038970

69 V. Wang, N. Xu, J.-C. Liu, G. Tang and W.-T. Geng. VASPKIT: A user-friendly interface facilitating high-throughput computing and analysis using VASP code. *Comp. Phys. Commun.* 267, 108033 (2021). https://doi.org/10.1016/j.cpc.2021.108033

70 D. Sheppard, R. Terrell and G. Henkelman. Optimization methods for finding minimum energy paths. *J. Chem. Phys.* 128 (2008). https://doi.org/10.1063/1.2841941

71 D. Sheppard, P. Xiao, W. Chemelewski, D. D. Johnson and G. Henkelman. A generalized solid-state nudged elastic band method. *J. Chem. Phys.* 136 (2012). https://doi.org/10.1063/1.3684549

72 Q. Ren, C. Zhu, S. Ma, Z. Wang, J. Yan, T. Wan, W. Yan and Y. Chai. Optoelectronic Devices for In-Sensor Computing. *Adv. Mater.* 2407476 (2024). https://doi.org/10.1002/adma.202407476

73 R. S. Williams, S. Goswami and S. Goswami. Potential and challenges of computing with molecular materials. *Nat. Mater.* 23, 1475 (2024). https://doi.org/10.1038/s41563-024-01820-4

74 R. Li, Z. Yue, H. Luan, Y. Dong, X. Chen and M. Gu. Multimodal Artificial Synapses for Neuromorphic Application. *Research* 7, 0427 (2024). https://doi.org/10.34133/research.0427

75 S. Wang, X. Chen, C. Zhao, Y. Kong, B. Lin, Y. Wu, Z. Bi, Z. Xuan, T. Li, Y. Li, W. Zhang, E. Ma, Z. Wang and W. Ma. An organic electrochemical transistor for multi-modal sensing, memory and processing. *Nat. Electron.* 6, 281 (2023). https://doi.org/10.1038/s41928-023-00950-y

76 A. Mehonic and A. J. Kenyon. Brain-inspired computing needs a master plan. *Nature* 604, 255 (2022). https://doi.org/10.1038/s41586-021-04362-w

77 C. Choi, H. Kim, J.-H. Kang, M.-K. Song, H. Yeon, C. S. Chang, J. M. Suh, J. Shin, K. Lu, B.-I. Park, Y. Kim, H. E. Lee, D. Lee, J. Lee, I. Jang, S. Pang, K. Ryu, S.-H. Bae, Y. Nie, H. S. Kum, M.-C. Park, S. Lee, H.-J. Kim, H. Wu, P. Lin and J. Kim. Reconfigurable heterogeneous integration using stackable chips with embedded artificial intelligence. *Nat. Electron.* 5, 386 (2022). https://doi.org/10.1038/s41928-022-00778-y

78 B. J. Shastri, A. N. Tait, T. Ferreira de Lima, W. H. P. Pernice, H. Bhaskaran, C. D. Wright and P. R. Prucnal. Photonics for artificial intelligence and neuromorphic computing. *Nat. Photon.* 15, 102 (2021).

https://doi.org/10.1038/s41566-020-00754-y

79 N. Youngblood, C. A. Rios Ocampo, W. H. P. Pernice and H. Bhaskaran. Integrated optical memristors. *Nat. Photon.* 17, 561 (2023). https://doi.org/10.1038/s41566-023-01217-w

80 J. Wang, N. Ilyas, Y. Ren, Y. Ji, S. Li, C. Li, F. Liu, D. Gu and K.-W. Ang. Technology and Integration Roadmap for Optoelectronic Memristor. *Adv. Mater.* 36, 2307393 (2024). https://doi.org/10.1002/adma.202307393

81 X. Han, J. Tao, Y. Liang, F. Guo, Z. Xu, W. Wu, J. Tong, M. Chen, C. Pan and J. Hao. Ultraweak light-modulated heterostructure with bidirectional photoresponse for static and dynamic image perception. *Nat. Commun.* 15, 10430 (2024). https://doi.org/10.1038/s41467-024-54845-3

82 Z. Dang, F. Guo, Y. Zhao, K. Jin, W. Jie and J. Hao. Ferroelectric Modulation of ReS_2-Based Multifunctional Optoelectronic Neuromorphic Devices for Wavelength-Selective Artificial Visual System. *Adv. Funct. Mater.* 34 (2024). https://doi.org/10.1002/adfm.202400105

83 Z. Dang, F. Guo, Z. Wang, W. Jie, K. Jin, Y. Chai and J. Hao. Object Motion Detection Enabled by Reconfigurable Neuromorphic Vision Sensor under Ferroelectric Modulation. *ACS Nano* 18, 27727 (2024). https://doi.org/10.1021/acsnano.4c10231

84 F. Guo, W. F. Io, Z. Dang, Y. Zhao, S.-Y. Pang, Y. Zhao, X. Lao and J. Hao. Bio-Inspired Optoelectronic Neuromorphic Device Based on 2D vdW Ferroelectric Heterostructure for Nonlinearly Preprocessing Visual Information and Convolutional Operation. *Adv. Electron. Mater.* 11, 2400528 (2024). https://doi.org/10.1002/aelm.202400528

85 M. Zheng, H. Sun, M. K. Chan and K. W. Kwok. Reversible and nonvolatile tuning of photoluminescence response by electric field for reconfigurable luminescent memory devices. *Nano Energy* 55, 22 (2019). https://doi.org/10.1016/j.nanoen.2018.10.055

86 J. Gong, P. Du, W. Li, G. Yuan, X. Mao and L. Luo. The Enhancement of Photochromism and Luminescence Modulation Properties of Ferroelectric Ceramics via Chemical and Physical Strategies. *Laser Photonics Rev.* 16, 2200170 (2022). https://doi.org/10.1002/lpor.202200170

87 J. Tan, Q. Li, S. Meng, Y. Li, J. Yang, Y. Ye, Z. Tang, S. Qu and X. Ren. Time-Dependent Phosphorescence Colors from Carbon Dots for Advanced Dynamic Information Encryption. *Adv. Mater.* 33, 2006781 (2021). https://doi.org/10.1002/adma.202006781

88 J. Du, X. Wang, S. Sun, Y. Wu, K. Jiang, S. Li and H. Lin. Pushing Trap-

Controlled Persistent Luminescence Materials toward Multi-Responsive Smart Platforms: Recent Advances, Mechanism, and Frontier Applications. *Adv. Mater.* 36, 2314083 (2024). https://doi.org/10.1002/adma.202314083

89 X. Zhou, L. Ning, J. Qiao, Y. Zhao, P. Xiong and Z. Xia. Interplay of defect levels and rare earth emission centers in multimode luminescent phosphors. *Nat. Commun.* 13, 7589 (2022). https://doi.org/10.1038/s41467-022-35366-3

90 P. Zhang, X. Zhao, Z. Jia, J. Dong, T. Liang, Y. Liu, Q. Cheng, L. Ding, L. Wu, D. Peng, Y. Kong, Y. Zhang and J. Xu. High Defect Tolerance Breaking the Design Limitation of Full-Spectrum Multimodal Luminescence Materials. *Adv. Mater.* 37, 2411532 (2024). https://doi.org/10.1002/adma.202411532

91 T. Zheng, M. Runowski, I. R. Martín, K. Soler-Carracedo, L. Peng, M. Skwierczyńska, M. Sójka, J. Barzowska, S. Mahlik, H. Hemmerich, F. Rivera-López, P. Kulpiński, V. Lavín, D. Alonso and D. Peng. Mechanoluminescence and Photoluminescence Heterojunction for Superior Multimode Sensing Platform of Friction, Force, Pressure, and Temperature in Fibers and 3D-Printed Polymers. *Adv. Mater.* 35, 2304140 (2023). https://doi.org/10.1002/adma.202304140

92 H. Yang, S. Li, J. Zheng, G. Chen, W. Wang, Y. Miao, N. Zhu, Y. Cong and J. Fu. Erasable, Rewritable, and Reprogrammable Dual Information Encryption Based on Photoluminescent Supramolecular Host-Guest Recognition and Hydrogel Shape Memory. *Adv. Mater.* 35, 2301300 (2023). https://doi.org/10.1002/adma.202301300

93 J. Huang, L. Tu, H. Huang, H. Wei, Q. Zhang and B. Zhou. Manipulating energy migration in nanoparticles toward tunable photochromic upconversion. *Nat. Commun.* 15, 10890 (2024). https://doi.org/10.1038/s41467-024-55258-y

94 H. Yang, Y. Wei, H. Ju, X. Huang, J. Li, W. Wang, D. Peng, D. Tu and G. Li. Microstrain-Stimulated Elastico-Mechanoluminescence with Dual-Mode Stress Sensing. *Adv. Mater.* 36, 2401296 (2024). https://doi.org/10.1002/adma.202401296

95 C. Lin, Y. Zhuang and R.-J. Xie.Photofunctional Nanomaterials for Biomedical Applications (Wiley, 2025).

96 R. R. Yang, M. Li, Y. F. Zhao, P. Wang and S. Ye. Regulating synthesis and photochromic behavior via interfacial Eu^{3+}/Eu^{2+}-Pb^{0}/Pb^{2+} redox of the $CsPbCl_{1.5}Br_{1.5}@Ca_{0.9}Eu_{0.1}MoO_4$ porous composites. *Mater. Today Chem.* 23, 100721 (2022). https://doi.org/10.1016/j.mtchem.2021.100721

97 M. Li, Y. Zhao, S. Zhang, R. Yang, W. Qiu, P. Wang, M. S. Molokeev and S. Ye. Understanding the Energy Barriers of the Reversible Ion Exchange Process in

$CsPbBr_{1.5}Cl_{1.5}$@Y_2O_3:Eu^{3+} Macroporous Composites and Their Application in Anti-Counterfeiting Codes. *ACS Appl. Mater. Interfaces* 13, 60362 (2021). https://doi.org/10.1021/acsami.1c18030

98 Y. Zhao, M. Li, M. C. Wong, X. Han, F. Guo, Y. Liu, X. Lao, Z. Dang, S.-Y. Pang, Z. Wu, S. Ye and J. Hao. Smart phosphor with neuromorphic behaviors enabling full-photoluminescent Write and Read for all-optical physical reservoir computing. *Nat. Commun.* 16, 7516 (2025). https://doi.org/10.1038/s41467-025-62745-3

99 W. Mao, C. R. Hall, S. Bernardi, Y.-B. Cheng, A. Widmer-Cooper, T. A. Smith and U. Bach. Light-induced reversal of ion segregation in mixed-halide perovskites. *Nat. Mater.* 20, 55 (2021). https://doi.org/10.1038/s41563-020-00826-y

100 H. Zhang, X. Fu, Y. Tang, H. Wang, C. Zhang, W. W. Yu, X. Wang, Y. Zhang and M. Xiao. Phase segregation due to ion migration in all-inorganic mixed-halide perovskite nanocrystals. *Nat. Commun.* 10, 1088 (2019). https://doi.org/10.1038/s41467-019-09047-7

101 Y. Zhao, R. Yang, W. Wan, X. Jing, T. Wen and S. Ye. Stabilizing $CsPbBr_3$ quantum dots with conjugated aromatic ligands and their regulated optical behaviors. *Chem. Eng. J.* 389, 124453 (2020). https://doi.org/10.1016/j.cej.2020.124453

102 R. I. Biega and L. Leppert. Halogen vacancy migration at surfaces of $CsPbBr_3$ perovskites: insights from density functional theory. *J Phys. Energy* 3, 034017 (2021). https://doi.org/10.1088/2515-7655/ac10fe

103 Y. Wang, R. Yang, Y. Zhao, L. Hong and S. Ye. Lanthanide-Containing Heteropolyoxomolybdate as Precursor to Porous Complex Oxides via Polymeric Micelle Assembly and Its Heterostructure with Carbon Dots for Anticounterfeiting Application. *Adv. Opt. Mater.* 12, 2302485 (2024). https://doi.org/10.1002/adom.202302485

104 Y. Zhao, F. Cheng, S. Zhang, R. Yang, M. Li, H. Ming and S. Ye. Formation mechanisms of $CsPbBr_3$/Cs_4PbBr_6 microscale composites assisted with imidazolium cations and their device applications. *Dalton Trans.* 51, 9445 (2022). https://doi.org/10.1039/D2DT00842D

105 D. Yang, X. Li, W. Zhou, S. Zhang, C. Meng, Y. Wu, Y. Wang and H. Zeng. $CsPbBr_3$ Quantum Dots 2.0: Benzenesulfonic Acid Equivalent Ligand Awakens Complete Purification. *Adv. Mater.* 31, 1900767 (2019). https://doi.org/10.1002/adma.201900767

106 G. H. Ahmed, J. K. El-Demellawi, J. Yin, J. Pan, D. B. Velusamy, M. N. Hedhili,

E. Alarousu, O. M. Bakr, H. N. Alshareef and O. F. Mohammed. Giant Photoluminescence Enhancement in $CsPbCl_3$ Perovskite Nanocrystals by Simultaneous Dual-Surface Passivation. *ACS Energy Lett.* 3, 2301 (2018). https://doi.org/10.1021/acsenergylett.8b01441

107 A. J. Barker, A. Sadhanala, F. Deschler, M. Gandini, S. P. Senanayak, P. M. Pearce, E. Mosconi, A. J. Pearson, Y. Wu, A. R. Srimath Kandada, T. Leijtens, F. De Angelis, S. E. Dutton, A. Petrozza and R. H. Friend. Defect-Assisted Photoinduced Halide Segregation in Mixed-Halide Perovskite Thin Films. *ACS Energy Lett.* 2, 1416 (2017). https://doi.org/10.1021/acsenergylett.7b00282

108 O. Lee, T. Wei, K. D. Stenning, J. C. Gartside, D. Prestwood, S. Seki, A. Aqeel, K. Karube, N. Kanazawa, Y. Taguchi, C. Back, Y. Tokura, W. R. Branford and H. Kurebayashi. Task-adaptive physical reservoir computing. *Nat. Mater.* 23, 79 (2024). https://doi.org/10.1038/s41563-023-01698-8

109 T. Ohno, T. Hasegawa, T. Tsuruoka, K. Terabe, J. K. Gimzewski and M. Aono. Short-term plasticity and long-term potentiation mimicked in single inorganic synapses. *Nat. Mater.* 10, 591 (2011). https://doi.org/10.1038/nmat3054

110 M. Cucchi, S. Abreu, G. Ciccone, D. Brunner and H. Kleemann. Hands-on reservoir computing: a tutorial for practical implementation. *Neuromorph. Comput. Eng.* 2, 032002 (2022). https://doi.org/10.1088/2634-4386/ac7db7

111 G. Tanaka, T. Yamane, J. B. Héroux, R. Nakane, N. Kanazawa, S. Takeda, H. Numata, D. Nakano and A. Hirose. Recent advances in physical reservoir computing: A review. *Neural Networks* 115, 100 (2019). https://doi.org/10.1016/j.neunet.2019.03.005

112 F. Ferrarese Lupi, M. Rosero-Realpe, A. Ocarino, F. Frascella, G. Milano and A. Angelini. Neuromorphic Light-Responsive Organic Matter for in Materia Reservoir Computing. *Adv. Mater.* 2501813 (2025). https://doi.org/10.1002/adma.202501813

113 Z. Zhang, X. Zhao, X. Zhang, X. Hou, X. Ma, S. Tang, Y. Zhang, G. Xu, Q. Liu and S. Long. In-sensor reservoir computing system for latent fingerprint recognition with deep ultraviolet photo-synapses and memristor array. *Nat. Commun.* 13, 6590 (2022). https://doi.org/10.1038/s41467-022-34230-8

114 Z. Liu, Q. Zhang, D. Xie, M. Zhang, X. Li, H. Zhong, G. Li, M. He, D. Shang, C. Wang, L. Gu, G. Yang, K. Jin and C. Ge. Interface-type tunable oxygen ion dynamics for physical reservoir computing. *Nat. Commun.* 14, 7176 (2023). https://doi.org/10.1038/s41467-023-42993-x

115 K. Liu, T. Zhang, B. Dang, L. Bao, L. Xu, C. Cheng, Z. Yang, R. Huang and Y. Yang. An optoelectronic synapse based on α-In_2Se_3 with controllable temporal

dynamics for multimode and multiscale reservoir computing. *Nat. Electron.* 5, 761 (2022). https://doi.org/10.1038/s41928-022-00847-2

116 X. Liang, J. Tang, Y. Zhong, B. Gao, H. Qian and H. Wu. Physical reservoir computing with emerging electronics. *Nat. Electron.* 7, 193 (2024). https://doi.org/10.1038/s41928-024-01133-z

117 L. Deng. The MNIST Database of Handwritten Digit Images for Machine Learning Research [Best of the Web]. *IEEE Signal Process. Mag.* 29, 141 (2012). https://doi.org/10.1109/MSP.2012.2211477

118 G. Bradski and A. Kaehler. OpenCV. Dr. Dobb's journal of software tools 3 (2000).

119 D. P. Kingma. Adam: A method for stochastic optimization. ArXiv, 1412.6980 (2014).

120 Y. I. Shehu, A. Ruiz-Garcia, V. Palade and A. James. Sokoto Coventry Fingerprint Dataset. (2018).

121 F. Guo, M. Song, M.-C. Wong, R. Ding, W. F. Io, S.-Y. Pang, W. Jie and J. Hao. Multifunctional Optoelectronic Synapse Based on Ferroelectric Van der Waals Heterostructure for Emulating the Entire Human Visual System. *Adv. Funct. Mater.* 32, 2108014 (2022). https://doi.org/10.1002/adfm.202108014

122 A. Bednarkiewicz, M. Szalkowski, M. Majak, Z. Korczak, M. Misiak and S. Maćkowski. All-Optical Data Processing with Photon-Avalanching Nanocrystalline Photonic Synapse. *Adv. Mater.* 35, 2304390 (2023). https://doi.org/10.1002/adma.202304390

123 H. Bian, X. Qin, Y. Wu, Z. Yi, S. Liu, Y. Wang, C. D. S. Brites, L. D. Carlos and X. Liu. Multimodal Tuning of Synaptic Plasticity Using Persistent Luminescent Memitters. *Adv. Mater.* 34, 2101895 (2022). https://doi.org/10.1002/adma.202101895

124 H. Chen, Y. Hou, Y. Shi, Y. Zhang, S. Wang, Q. Peng and H. Huang. Organic All-Photonic Artificial Synapses Enabled by Anti-Stokes Photoluminescence. *J. Am. Chem. Soc.* 145, 11988 (2023). https://doi.org/10.1021/jacs.2c13471

125 T. Dai, A. Ma, J. Mao, Y. Ao, X. Jia, Y. Zheng, C. Zhai, Y. Yang, Z. Li, B. Tang, J. Luo, B. Zhang, X. Hu, Q. Gong and J. Wang. A programmable topological photonic chip. *Nat. Mater.* 23, 928 (2024). https://doi.org/10.1038/s41563-024-01904-1

126 D. Wang, S. Hao, B. Dkhil, B. Tian and C. Duan. Ferroelectric materials for neuroinspired computing applications. *Fundam. Res.* 4, 1272 (2024). https://doi.org/10.1016/j.fmre.2023.04.013

127 J. Choe. Memory Technology: Trends & Challenges. 2021 International

Conference on Simulation of Semiconductor Processes and Devices (SISPAD)

128 T. Wan, B. Shao, S. Ma, Y. Zhou, Q. Li and Y. Chai. In-Sensor Computing: Materials, Devices, and Integration Technologies. *Adv. Mater.* 35, 2203830 (2023). https://doi.org/10.1002/adma.202203830

129 H.-J. Lee, M. Lee, K. Lee, J. Jo, H. Yang, Y. Kim, S. C. Chae, U. Waghmare and J. H. Lee. Scale-free ferroelectricity induced by flat phonon bands in HfO_2. *Science* 369, 1343 (2020). https://doi.org/10.1126/science.aba0067

130 S. S. Cheema, D. Kwon, N. Shanker, R. dos Reis, S.-L. Hsu, J. Xiao, H. Zhang, R. Wagner, A. Datar, M. R. McCarter, C. R. Serrao, A. K. Yadav, G. Karbasian, C.-H. Hsu, A. J. Tan, L.-C. Wang, V. Thakare, X. Zhang, A. Mehta, E. Karapetrova, R. V. Chopdekar, P. Shafer, E. Arenholz, C. Hu, R. Proksch, R. Ramesh, J. Ciston and S. Salahuddin. Enhanced ferroelectricity in ultrathin films grown directly on silicon. *Nature* 580, 478 (2020). https://doi.org/10.1038/s41586-020-2208-x

131 S. S. Cheema, N. Shanker, L.-C. Wang, C.-H. Hsu, S.-L. Hsu, Y.-H. Liao, M. San Jose, J. Gomez, W. Chakraborty, W. Li, J.-H. Bae, S. K. Volkman, D. Kwon, Y. Rho, G. Pinelli, R. Rastogi, D. Pipitone, C. Stull, M. Cook, B. Tyrrell, V. A. Stoica, Z. Zhang, J. W. Freeland, C. J. Tassone, A. Mehta, G. Saheli, D. Thompson, D. I. Suh, W.-T. Koo, K.-J. Nam, D. J. Jung, W.-B. Song, C.-H. Lin, S. Nam, J. Heo, N. Parihar, C. P. Grigoropoulos, P. Shafer, P. Fay, R. Ramesh, S. Mahapatra, J. Ciston, S. Datta, M. Mohamed, C. Hu and S. Salahuddin. Ultrathin ferroic HfO_2–ZrO_2 superlattice gate stack for advanced transistors. *Nature* 604, 65 (2022). https://doi.org/10.1038/s41586-022-04425-6

132 M. Falkowski, C. Künneth, R. Materlik and A. Kersch. Unexpectedly large energy variations from dopant interactions in ferroelectric HfO_2 from high-throughput ab initio calculations. *npj Comput. Mater.* 4, 73 (2018). https://doi.org/10.1038/s41524-018-0133-4

133 J. Guo, L. Tao, X. Xu, L. Hou, C.-W. Nan, S. Du, C. Chen and J. Ma. Rhombohedral R_3 phase of Mn-doped $Hf_{0.5}Zr_{0.5}O_2$ epitaxial films with robust ferroelectricity. *Adv. Mater.* 2406038 (2024). https://doi.org/10.1002/adma.202406038

134 H. A. Hsain, Y. Lee, M. Materano, T. Mittmann, A. Payne, T. Mikolajick, U. Schroeder, G. N. Parsons and J. L. Jones. Many routes to ferroelectric HfO_2: A review of current deposition methods. *J. Vac. Sci. Technol.* A 40 (2021). https://doi.org/10.1116/6.0001317

135 P. Jiang, Q. Luo, X. Xu, T. Gong, P. Yuan, Y. Wang, Z. Gao, W. Wei, L. Tai and H. Lv. Wake-Up Effect in HfO_2-Based Ferroelectric Films. *Adv. Electron. Mater.*

7, 2000728 (2021). https://doi.org/10.1002/aelm.202000728

136 M. H. Park, Y. H. Lee, H. J. Kim, Y. J. Kim, T. Moon, K. D. Kim, J. Müller, A. Kersch, U. Schroeder, T. Mikolajick and C. S. Hwang. Ferroelectricity and Antiferroelectricity of Doped Thin HfO_2-Based Films. *Adv. Mater.* 27, 1811 (2015). https://doi.org/10.1002/adma.201404531

137 S. Mueller, J. Müller, U. Schroeder and T. Mikolajick. Reliability characteristics of ferroelectric Si:HfO_2 thin films for memory applications. *IEEE Trans. Dev. Mater.* Reliability 13, 93 (2013). https://doi.org/10.1109/TDMR.2012.2216269

138 D. Martin, J. Müller, T. Schenk, T. M. Arruda, A. Kumar, E. Strelcov, E. Yurchuk, S. Müller, D. Pohl, U. Schröder, S. V. Kalinin and T. Mikolajick. Ferroelectricity in Si-Doped HfO_2 Revealed: A Binary Lead-Free Ferroelectric. *Adv. Mater.* 26, 8198 (2014). https://doi.org/10.1002/adma.201403115

139 Y. Wang, L. Tao, R. Guzman, Q. Luo, W. Zhou, Y. Yang, Y. Wei, Y. Liu, P. Jiang, Y. Chen, S. Lv, Y. Ding, W. Wei, T. Gong, Y. Wang, Q. Liu, S. Du and M. Liu. A stable rhombohedral phase in ferroelectric $Hf(Zr)_{1+x}O_2$ capacitor with ultralow coercive field. *Science* 381, 558 (2023). https://doi.org/10.1126/science.adf6137

140 H. Wang, Z. Guan, J. Li, Z. Luo, X. Du, Z. Wang, H. Zhao, S. Shen, Y. Yin and X. Li. Silicon-Compatible Ferroelectric Tunnel Junctions with a $SiO_2/Hf_{0.5}Zr_{0.5}O_2$ Composite Barrier as Low-Voltage and Ultra-High-Speed Memristors. *Adv. Mater.* 2211305 (2024). https://doi.org/10.1002/adma.202211305

141 K. Lee, T. Y. Lee, S. M. Yang, D. H. Lee, J. Park and S. C. Chae. Ferroelectricity in epitaxial Y-doped HfO_2 thin film integrated on Si substrate. *Appl. Phys. Lett.* 112 (2018). https://doi.org/10.1063/1.5020688

142 T. Mimura, T. Shimizu, H. Uchida, O. Sakata and H. Funakubo. Thickness-dependent crystal structure and electric properties of epitaxial ferroelectric Y_2O_3-HfO_2 films. *Appl. Phys. Lett.* 113 (2018). https://doi.org/10.1063/1.5040018

143 X. Xu, F.-T. Huang, Y. Qi, S. Singh, K. M. Rabe, D. Obeysekera, J. Yang, M.-W. Chu and S.-W. Cheong. Kinetically stabilized ferroelectricity in bulk single-crystalline HfO_2:Y. *Nat. Mater.* 20, 826 (2021). https://doi.org/10.1038/s41563-020-00897-x

144 Y. Wei, P. Nukala, M. Salverda, S. Matzen, H. J. Zhao, J. Momand, A. S. Everhardt, G. Agnus, G. R. Blake, P. Lecoeur, B. J. Kooi, J. Íñiguez, B. Dkhil and B. Noheda. A rhombohedral ferroelectric phase in epitaxially strained $Hf_{0.5}Zr_{0.5}O_2$ thin films. *Nat. Mater.* 17, 1095 (2018).

https://doi.org/10.1038/s41563-018-0196-0

145 C. Zhou, L. Ma, Y. Feng, C.-Y. Kuo, Y.-C. Ku, C.-E. Liu, X. Cheng, J. Li, Y. Si, H. Huang, Y. Huang, H. Zhao, C.-F. Chang, S. Das, S. Liu and Z. Chen. Enhanced polarization switching characteristics of HfO_2 ultrathin films via acceptor-donor co-doping. *Nat. Commun.* 15, 2893 (2024). https://doi.org/10.1038/s41467-024-47194-8

146 T. Schenk, N. Godard, A. Mahjoub, S. Girod, A. Matavz, V. Bobnar, E. Defay and S. Glinsek. Toward Thick Piezoelectric HfO_2-Based Films. Phys. Status *Solidi - Rapid Res. Lett.* 14, 1900626 (2020). https://doi.org/10.1002/pssr.201900626

147 T. Mimura, T. Shimizu and H. Funakubo. Ferroelectricity in $YO_{1.5}$-HfO_2 films around 1 μm in thickness. *Appl. Phys. Lett.* 115 (2019). https://doi.org/10.1063/1.5097880

148 Y. Yun, P. Buragohain, M. Li, Z. Ahmadi, Y. Zhang, X. Li, H. Wang, J. Li, P. Lu, L. Tao, H. Wang, J. E. Shield, E. Y. Tsymbal, A. Gruverman and X. Xu. Intrinsic ferroelectricity in Y-doped HfO_2 thin films. *Nat. Mater.* 21, 903 (2022). https://doi.org/10.1038/s41563-022-01282-6

149 X. Yan, J. Niu, Z. Fang, J. Xu, C. Chen, Y. Zhang, Y. Sun, L. Tong, J. Sun, S. Yin, Y. Shao, S. Sun, J. Zhao, M. Lanza, T. Ren, J. Chen and P. Zhou. High-performance in domain matching epitaxial La:HfO_{-2} film memristor for spiking neural network system application. *Mater. Today* (2024). https://doi.org/10.1016/j.mattod.2024.09.016

150 B. Noheda, P. Nukala and M. Acuautla. Lessons from hafnium dioxide-based ferroelectrics. *Nat. Mater.* 22, 562 (2023). https://doi.org/10.1038/s41563-023-01507-2

151 W. C. Wang, B. Zhou, S. H. Xu, Z. M. Yang and Q. Y. Zhang. Recent advances in soft optical glass fiber and fiber lasers. *Prog. Mater. Sci.* 101, 90 (2019). https://doi.org/10.1016/j.pmatsci.2018.11.003

152 Y. Ma, M. Song, L. Li, X. Lao, M. C. Wong and J. Hao. Advances in upconversion luminescence nanomaterial-based biosensor for virus diagnosis. *Exploration* 2 (2022). https://doi.org/10.1002/EXP.20210216

153 G. Bai, S. Yuan, Y. Zhao, Z. Yang, S. Y. Choi, Y. Chai, S. F. Yu, S. P. Lau and J. Hao. 2D Layered Materials of Rare-Earth Er-Doped MoS_2 with NIR-to-NIR Down- and Up-Conversion Photoluminescence. *Adv. Mater.* 28, 7472 (2016). https://doi.org/10.1002/adma.201601833

154 Y. Liu, G. Bai, Y. Lyu, Y. Hua, R. Ye, J. Zhang, L. Chen, S. Xu and J. Hao. Ultrabroadband tuning and fine structure of emission spectra in lanthanide er-

doped znse nanosheets for display and temperature sensing. *ACS Nano* 14, 16003 (2020). https://doi.org/10.1021/acsnano.0c07547

155 R. Batra, T. D. Huan, G. A. Rossetti, Jr. and R. Ramprasad. Dopants Promoting Ferroelectricity in Hafnia: Insights from a comprehensive *Chemical Space Exploration. Chem.* Mater. 29, 9102 (2017). https://doi.org/10.1021/acs.chemmater.7b02835

156 J.-H. Yuan, G.-Q. Mao, K.-H. Xue, N. Bai, C. Wang, Y. Cheng, H. Lyu, H. Sun, X. Wang and X. Miao. Ferroelectricity in HfO_2 from a Coordination Number Perspective. *Chem. Mater.* 35, 94 (2023). https://doi.org/10.1021/acs.chemmater.2c02660

157 S. Heer, K. Kömpe, H. U. Güdel and M. Haase. Highly efficient multicolour upconversion emission in transparent colloids of lanthanide-doped $NaYF_4$ nanocrystals. *Adv. Mater.* 16, 2102 (2004). https://doi.org/10.1002/adma.200400772

158 D. S. Yasyrkina, S. Kuznetsov, A. V. Ryabova, D. V. Pominova, V. V. Voronov, R. P. Ermakov and P. P. Fedorov. Dependence of quantum yield of up-conversion luminescence on the composition of fluorite-type solid solution $NaY_{1-x-y}Yb_xEr_yF_4$. *Mater. Sci. Phys.* (2013).

159 R. Luo, T. Li, Y. Chen, Z. Ning, Y. Zhao, M. Liu, X. Lai, C. Zhong, C. Wang, J. Bi and D. Gao. $Na_{1-x}Li_x(Gd_{0.39}Y_{0.39}Yb_{0.2}Er_{0.02})F_4$ ($0 \leq x \leq 1$) Solid Solution Microcrystals: Li/Na Ratio-Induced Transition of Crystalline Phase and Morphology and Their Enhanced Upconversion Emission. *Cryst. Growth Des.* 18, 6581 (2018). https://doi.org/10.1021/acs.cgd.8b00791

160 S.-T. Fan, Y.-W. Chen and C. W. Liu. Strain effect on the stability in ferroelectric HfO_2 simulated by first-principles calculations. *J. Phys. D: Appl. Phys.* 53, 23LT01 (2020). https://doi.org/10.1088/1361-6463/ab7fd4

161 Y. K. Chang, P. J. Liao, S. H. Yeong, Y. M. Lin, J. H. Lee, C. T. Lin, Z. Yu, W. Tsai and P. C. McIntyre. in 2022 IEEE International Reliability Physics Symposium (IRPS).

162 Y. Wu, Y. Zhang, J. Jiang, L. Jiang, M. Tang, Y. Zhou, M. Liao, Q. Yang and E. Y. Tsymbal. Unconventional Polarization-Switching Mechanism in $(Hf,Zr)O_2$ Ferroelectrics and Its Implications. *Phys. Rev. Lett.* 131, 226802 (2023). https://doi.org/10.1103/PhysRevLett.131.226802

163 A. Silva, I. Fina, F. Sánchez, J. P. B. Silva, L. Marques and V. Lenzi. Unraveling the ferroelectric switching mechanisms in ferroelectric pure and La doped HfO_2 epitaxial thin films. *Mater. Today Phys.* 34, 101064 (2023). https://doi.org/10.1016/j.mtphys.2023.101064

164 E. G. Seebauer and M. C. Kratzer. Charged point defects in semiconductors. *Mater. Sci. Eng.: R: Rep.* 55, 57 (2006). https://doi.org/10.1016/j.mser.2006.01.002

165 A. Glavic and M. Bjorck. GenX 3: the latest generation of an established tool. *J. Appl. Crystallogr.* 55, 1063 (2022). https://doi.org/10.1107/S1600576722006653

166 C.-K. Lee, E. Cho, H.-S. Lee, C. Hwang and S. Han. First-principles study on doping and phase stability of HfO_2. *Phys. Rev. B* 78 (2008). https://doi.org/10.1103/PhysRevB.78.012102

167 P. Nukala, Y. Wei, V. de Haas, Q. Guo, J. Antoja-Lleonart and B. Noheda. Guidelines for the stabilization of a polar rhombohedral phase in epitaxial $Hf_{0.5}Zr_{0.5}O_2$ thin films. *Ferroelectrics* 569, 148 (2020). https://doi.org/10.1080/00150193.2020.1791658

168 H. Wang, L. Liu, J. Wang, C. Li, J. Hou and K. Zheng. The Development of iDPC-STEM and Its Application in Electron Beam Sensitive Materials. *Molecules* 27, 3829 (2022). https://doi.org/10.3390/molecules27123829

169 A. Abdukayum, J. T. Chen, Q. Zhao and X. P. Yan. Functional near infrared-emitting Cr^{3+}/Pr^{3+} Co-doped zinc gallogermanate persistent luminescent nanoparticles with superlong afterglow for in vivo targeted bioimaging. *J. Am. Chem. Soc.* 135, 14125 (2013). https://doi.org/10.1021/ja404243v

170 Z. Rao, X. Xie, X. Wang, A. Mahmood, S. Tong, M. Ge and J. Sun. Defect Chemistry of Er^{3+}-Doped TiO_2 and Its Photocatalytic Activity for the Degradation of Flowing Gas-Phase VOCs. *J. Phys. Chem. C* 123, 12321 (2019). https://doi.org/10.1021/acs.jpcc.9b02093

171 J. Xiong, Y. Zhao, J. Zhu, X. Yang, X. Kuang, C.-H. Wang, Q. Zhang and S. Ye. Optical Interpretation of a Second-Order Phase Transition Induced by Thermal-Driven Li^+ Migration via Configurational Entropy in $CaTiO_3$:Li^+,Yb^{3+},Er^{3+}. *J. Phys. Chem. C* 125, 6916 (2021). https://doi.org/10.1021/acs.jpcc.1c00466

172 Z. Wang and A. Meijerink. Concentration Quenching in Upconversion Nanocrystals. *J. Phys. Chem. C* 122, 26298 (2018). https://doi.org/10.1021/acs.jpcc.8b09371

173 K. Wang, H. Wu, G.-H. Pan, H. Wu, L. Zhang and J. Zhang. Enhanced upconversion luminescence and optical thermometry in Er^{3+}/Yb^{3+} heavily doped ZrO_2 by stabilizing in the monoclinic phase. *Mater. Chem. Front.* 5, 5142 (2021). https://doi.org/10.1039/D1QM00440A

174 A. Kashir, S. Oh and H. Hwang. Defect Engineering to Achieve Wake-up Free HfO_2-Based Ferroelectrics. *Adv. Eng. Mater.* 23, 2000791 (2021).

https://doi.org/10.1002/adem.202000791

175 G. Kim, S. Lee, T. Eom, T. Kim, M. Jung, H. Shin, Y. Jeong, M. Kang and S. Jeon. High performance ferroelectric field-effect transistors for large memory-window, high-reliability, high-speed 3D vertical NAND flash memory. *J. Mater. Chem. C* 10, 9802 (2022). https://doi.org/10.1039/D2TC01608G

176 D. C. Rubin and A. E. Wenzel. One hundred years of forgetting: A quantitative description of retention. *Psychol. Rev.* 103, 734 (1996). https://doi.org/10.1037/0033-295X.103.4.734

177 R. Yang, D. Hu, Q. Chen, Z. Wang, B. Lu, Z. Ye, X. Li and J. Lu. SnS-Facilitated ZnAlSnO-Based Fully Optically Modulated Artificial Synaptic Device for Image Processing. *Adv. Funct. Mater.* 35, 2414210 (2025). https://doi.org/10.1002/adfm.202414210

178 R. Yang, Y. Wang, S. Li, D. Hu, Q. Chen, F. Zhuge, Z. Ye, X. Pi and J. Lu. All-Optically Controlled Artificial Synapse Based on Full Oxides for Low-Power Visible Neural Network Computing. *Adv. Funct. Mater.* 34, 2312444 (2024). https://doi.org/10.1002/adfm.202312444

179 H. Jiang, H. Ji, Z. Ma, D. Yang, J. Ma, M. Zhang, X. Li, M. Wang, Y. Li, X. Chen, D. Wu, X. Li, C. Shan and Z. Shi. Simultaneous achieving negative photoconductivity response and volatile resistive switching in Cs_2CoCl_4 single crystals towards artificial optoelectronic synapse. *Light Sci. Appl.* 13, 316 (2024). https://doi.org/10.1038/s41377-024-01642-8

180 D. Zhang, W. Xiao, C. Liu, X. Liu, J. Ren, B. Xu and J. Qiu. Highly efficient phosphor-glass composites by pressureless sintering. *Nat. Commun.* 11, 2805 (2020). https://doi.org/10.1038/s41467-020-16649-z

181 P. Wang, H. Lin, G. Chen, W. Weng, Y. Xu, Y. Lin, J. Xu, Y. Cheng and Y. Wang. Rapid sintering of high-efficiency phosphor-in-glass films for laser-driven light source. *Nat. Commun.* 16, 2807 (2025). https://doi.org/10.1038/s41467-025-58099-5

182 E. Song, M. Chen, Z. Chen, Y. Zhou, W. Zhou, H.-T. Sun, X. Yang, J. Gan, S. Ye and Q. Zhang. Mn^{2+}-activated dual-wavelength emitting materials toward wearable optical fibre temperature sensor. *Nat. Commun.* 13, 2166 (2022). https://doi.org/10.1038/s41467-022-29881-6

183 Q. Wu, Y. Cao, Q. Luo, H. Jiang, Z. Han, Y. Han, C. Dou, H. Lv, Q. Liu, J. Yang and M. Liu. A 9-Mb HZO-Based Embedded FeRAM With 10-Cycle Endurance and 5/7-ns Read/Write Using ECC-Assisted Data Refresh and Offset-Canceled Sense Amplifier. *IEEE J. Solid-State Circuits* 59, 208 (2024). https://doi.org/10.1109/JSSC.2023.3320659